

# Stimulus Artifact Reduction in Somatosensory Evoked Potential Measurements Using Velocity Filters

By

**Nabil Yazdani**

A thesis submitted to the  
Faculty of Graduate Studies and Research Office  
in partial fulfillment of the requirements for the degree of

Master of Applied Science in Engineering, Electrical  
Faculty of Engineering  
Carleton University  
Ottawa, Ontario, Canada

©2006, Nabil Yazdani



Library and  
Archives Canada

Bibliothèque et  
Archives Canada

Published Heritage  
Branch

Direction du  
Patrimoine de l'édition

395 Wellington Street  
Ottawa ON K1A 0N4  
Canada

395, rue Wellington  
Ottawa ON K1A 0N4  
Canada

*Your file* *Votre référence*  
*ISBN: 978-0-494-18336-6*  
*Our file* *Notre référence*  
*ISBN: 978-0-494-18336-6*

**NOTICE:**

The author has granted a non-exclusive license allowing Library and Archives Canada to reproduce, publish, archive, preserve, conserve, communicate to the public by telecommunication or on the Internet, loan, distribute and sell theses worldwide, for commercial or non-commercial purposes, in microform, paper, electronic and/or any other formats.

The author retains copyright ownership and moral rights in this thesis. Neither the thesis nor substantial extracts from it may be printed or otherwise reproduced without the author's permission.

**AVIS:**

L'auteur a accordé une licence non exclusive permettant à la Bibliothèque et Archives Canada de reproduire, publier, archiver, sauvegarder, conserver, transmettre au public par télécommunication ou par l'Internet, prêter, distribuer et vendre des thèses partout dans le monde, à des fins commerciales ou autres, sur support microforme, papier, électronique et/ou autres formats.

L'auteur conserve la propriété du droit d'auteur et des droits moraux qui protègent cette thèse. Ni la thèse ni des extraits substantiels de celle-ci ne doivent être imprimés ou autrement reproduits sans son autorisation.

---

In compliance with the Canadian Privacy Act some supporting forms may have been removed from this thesis.

Conformément à la loi canadienne sur la protection de la vie privée, quelques formulaires secondaires ont été enlevés de cette thèse.

While these forms may be included in the document page count, their removal does not represent any loss of content from the thesis.

Bien que ces formulaires aient inclus dans la pagination, il n'y aura aucun contenu manquant.

  
**Canada**

### **Author's Declaration**

I hereby declare that I am the sole author of this thesis.

I authorize Carleton University to lend this thesis to other institutions or individuals for the purpose of scholarly research.

Signature\_\_\_\_\_

I further authorize Carleton University to reproduce this thesis by photocopying or by other means, in total or in part, at the request of other institutions or individuals for the purpose of scholarly research.

Signature\_\_\_\_\_

## Abstract

Somatosensory evoked potentials (SEPs) are bio-electric signals that propagate through the nervous system in response to external stimuli. When using electrical stimulation, a current pulse is delivered at a location along the nerve, and electrodes are used to measure the evoked potential at a location down the nerve axon. A fundamental problem that arises when noninvasive measurements are required is that the stimulus pulse also spreads to the recording site via conduction through tissues creating a stimulus artifact (SA). This SA overlaps the SEP in both time and frequency, is coherent with the SEP, and is orders of magnitude larger than the SEP. It is often the case that the decaying tail component of the SA temporally exceeds the SEP latency and causes significant distortion to the SEP.

The motivation of this thesis is to remove the SA from the SEP by post-processing the distorted measurement after it has been acquired. The array processing technique of velocity filtering is employed using an array of SEP measurements along the axis of propagation. The fact that the SEP and SA differ widely in their propagation velocities is used as a basis for distinguishing them. This is accomplished using a spatio-temporal 2-D fan filter.

Using 11 channels of simulated data, the percent-residual-difference was 21.1%. In real data, spatial variation of the SEP along the array may also distort amplitude and timing information of the SEP. The performance and practicality of this method is examined and compared to that of existing methods from the literature, which are based on nonlinear adaptive noise cancellation (ANC). In actual measurements from 10 subjects, the filter outperforms nonlinear ANC according to 3 performance metrics.

## Acknowledgements

I have been very fortunate to have had the opportunity to study under Dr. Q. J. Zhang and Dr. A. D. C. Chan. They have both been very valuable to me both as professionals and leaders in terms of my learning as well as in being pleasant people to work with.

Professor Zhang provided continuous guidance, direction, and financial assistance to me during the first year of my graduate studies, spending lots of his extra time and effort to answer my many questions and explain concepts to me regarding RF and microwave circuits and nonlinear, dynamic modeling, simulation and optimization. I am grateful for this as well as for his enthusiasm for the work that we did. His graduate students Jianjun Xu, Lei Zhang, Yi Cao, Hitaesh Sharma, Humayun Kabir, and Kui Bo have all been pleasant to work with, bright and full of ideas, and good team players in our group work.

Professor Chan became my new graduate supervisor after switching research topics in the second year. He has also been a great leader and role model in many senses. I benefited a great deal from his technical and theoretical expertise in biological signal acquisition, modeling, and processing. I thank him for his patience, financial assistance, and especially his excellence in technical writing and editing. It has been a pleasure to work with his graduate students Hua Jin Guo, Vesal Badee, Geoff Green, and Mehran Talebinejad who are also good friends and talented engineers.

I thank my family and friends for their understanding and support. I also thank my father for his help as a parent and as an experienced senior engineer and for being a role-model whose level of achievements I can only dream of reaching one day.

## Table of Contents

Author's Declaration .....	iii
Abstract .....	iv
Acknowledgements .....	v
Table of Contents .....	vi
List of Figures .....	viii
List of Tables.....	x
List of Symbols and Abbreviations .....	xi
Chapter 1 Introduction.....	1
1.1 SEP Measurements.....	1
1.2 Current SA Reduction Techniques.....	3
1.3 Thesis Objective.....	7
1.4 Thesis Organization.....	9
Chapter 2 Literature Review .....	10
2.1 Motivation for Obtaining Undistorted SEP Measurements.....	10
2.2 Difficulties with Stimulus Artifact in SEP Measurements.....	11
2.3 Adaptive Filtering of Stimulus Artifact.....	15
2.3.1 Segmented Training.....	16
2.3.2 Sub-Threshold Training.....	19
2.4 Motivation for Velocity Filtering.....	21
Chapter 3 Velocity Filtering.....	24
3.1 Spatio-Temporal View of Signals .....	24
3.2 Theory of Velocity Filtering.....	31
3.3 Discrete Velocity Filtering .....	36
3.4 Practical Constraints.....	39
3.4.1 Spatial Resolution.....	40
3.4.2 Velocity Resolution .....	41
3.4.3 Trace-to-Trace Consistency of Signal Features.....	42
Chapter 4 Simulation Study Using Sinc Pulses.....	45
4.1 Simulation Study .....	45
4.2 Effect of Sampling Rate .....	50
4.3 Effect of Number of Channels.....	54

4.4 Effect of SEP Spatial Amplitude Variation.....	56
4.5 Loss of Low Frequency Information.....	58
Chapter 5 Simulation Study Using Synthetic SEP Measurements.....	60
5.1 Simulated SEP Array.....	60
5.2 Simulated Stimulus Artifact.....	63
5.3 Simulation Results.....	69
5.4 Comparison with Nonlinear ANC - Segmented Training.....	72
Chapter 6 Filtering Real SEP Array Data.....	80
6.1 Measurement Setup.....	80
6.1.1 Stimulation.....	81
6.1.2 SEP Recording.....	82
6.1.3 Physical Array Implementation.....	84
6.2 Results and Discussion.....	85
6.3 Comparison with Nonlinear ANC – Segmented Training.....	92
6.4 Conclusions.....	99
Chapter 7 Conclusions.....	102
7.1 Summary and Conclusions.....	102
7.2 Contributions.....	104
7.2.1 Minor Contributions.....	104
7.2.2 Major Contributions.....	105
7.3 Future Work.....	106
Appendix A Derivation of Fan Filter Impulse Response.....	113
Appendix B Carleton University Research Ethics Committee Consent Form.....	115

## List of Figures

Figure 1-1: Median nerve SEP measurement configuration.....	2
Figure 1-2: Adaptive noise cancellation scheme.....	4
Figure 1-3: ANC scheme used in segmented training, (a) training, (b) predicting .....	5
Figure 1-4: ANC Scheme used in sub-threshold training, (a) training, (b) predicting .....	6
Figure 2-1: Median nerve SEP measurement configuration.....	12
Figure 2-2: Adaptive noise cancellation schemes for SA reduction.....	17
Figure 2-3: Adaptive elements used in segmented training ANC schemes, (a) FIR filter, (b) truncated Volterra Series, (c) artificial neural network.....	18
Figure 2-4: Sub-threshold method of ANC for SA reduction .....	20
Figure 3-1: Sensor array data: constant velocity signal propagating along the array.....	25
Figure 3-2: Effect of apparent velocity on $k$ - $\omega$ magnitude spectrum .....	27
Figure 3-3: 2D signal with constant velocity in $(x, t)$ and $(k, \omega)$ spaces, (a) time domain traces, (b) $k$ - $\omega$ magnitude response, (c) contoured $k$ - $\omega$ magnitude response .....	29
Figure 3-4: Comparison of signals with different velocities in $(k, \omega)$ space of 25, 40, 65, and $\infty$ m/s (ordered top to bottom), (a) magnitude spectrum, (b) 2D contoured magnitude spectrum.....	31
Figure 3-5: Ideal frequency response of fan filter .....	32
Figure 3-6: Block diagram of velocity filter implementation.....	33
Figure 3-7: Illustration of 2D convolution (a) computation of output trace previous to center trace, (b) center trace, (c) trace following the center trace .....	35
Figure 3-8: Fan filter FIR approximation, (a) center traces of impulse response, (b) magnitude of frequency response, (c) phase of frequency response .....	39
Figure 3-9: Illustration of velocity resolution, (a) 2D projection onto $k$ - $\omega$ plane, (b) 1D illustration of low frequency distortion.....	42
Figure 4-1: (a) 21 simulated traces of $s_{2,n}(t)$ , (b) $k$ - $\omega$ magnitude spectrum of $s_n(t)$ .....	46
Figure 4-2: (a) FIR fan filter $k$ - $\omega$ magnitude response, (b) phase response .....	47
Figure 4-3: $k$ - $\omega$ magnitude spectrum of (a) input, (b) output .....	48
Figure 4-4: Center 5 traces of signals from Equation 4.1, (a) input, (b) output .....	49
Figure 4-5: Comparison of center trace output PSD with ideal.....	49
Figure 4-6: Effect of sampling rate on filtering performance, (a) PRD measure of distortion when filtering slow signal, (b) residual power when filtering fast signal, (c) PRD measure of overall error when filtering fast + slow signals.....	52

Figure 4-7: PRD of center trace filter output for different number of data channels .....	55
Figure 4-8: PRD of center trace filter output for different channel spacing.....	56
Figure 4-9: Power spectral density of center trace filter output .....	59
Figure 5-1:Block diagram illustrating synthetic SEP measurements .....	61
Figure 5-2:Synthesized 11-channel array of surface-recorded SEP's .....	62
Figure 5-3:Circuit schematic of SA generation mechanism model in Agilent ADS.....	64
Figure 5-4: Simulation of SA generation mechanism, (a) input current, (b) output voltage.....	68
Figure 5-5:Simulated SEP measurements with SA corruption (SEP amplitudes are scaled up).....	69
Figure 5-6:Center input and output traces for one filter pass, (a) input, (b) output.....	70
Figure 5-7: Center input and output traces after 200 filter pass, (a) input, (b) output.....	71
Figure 5-8:Input and output $k-\omega$ magnitude spectra after 200 filter pass, (a) input, (b) output .....	71
Figure 5-9:PSD of center trace output compared to ideal after 200 filter passes .....	72
Figure 5-10:Results of SEP estimate using segmented nonlinear ANC, (a) reference channel, (b) ideal SEP estimate, (c) primary channel, (d) comparison of SEP estimate and ideal .....	74
Figure 5-11:Results of SEP estimate using 11-channel velocity filter, (a) center trace SA, (b) center trace SEP, (c) center trace input, (d) comparison of center trace estimate and ideal .....	75
Figure 6-1: System diagram of SEP recording setup .....	81
Figure 6-2:11-channel SEP array measurements from subject S1, (a) raw measurement showing the SA, (b) zoomed in on SEP.....	85
Figure 6-3:Velocity filtered output, (S1)-(S10): Array data from subject (left), comparison of input and output center trace (middle), comparison of SEP at center trace input and output (right) .....	88
Figure 6-4: Array data from Subject S6 zoomed into SEP region .....	89
Figure 6-5: (S1)-(S10)Nonlinear ANC output (segmented training), array data from subject (left), comparison of input and output traces (middle), comparison of SEP at center trace input and output (right).....	95
Figure 6-6: Comparison of performance metrics for velocity filter and nonlinear ANC, (a) $\rho_1$ measure, (b) $\rho_2$ measure, (c) $\rho_3$ measure .....	97

## List of Tables

Table 5-1: Simulation parameters used to generate SEP waveforms .....	62
Table 5-2: Summary of performance indices for velocity filter and nonlinear ANC (grey box used to indicate which method was better according to the given metric) .....	78
Table 6-1: Summary of performance indices of velocity filtered SEP estimates for all subjects .....	90
Table 6-2: Summary of performance indices of Nonlinear ANC SEP estimates for all subjects .....	95

## List of Symbols and Abbreviations

A/D	Analog-to-Digital
Ag	Silver
AgCl	Silver Chloride
ANC	Adaptive Noise Cancellation
ANN	Artificial Neural Network
ASIC	Application-Specific Integrated Circuit
Cl <sup>-</sup>	Negative Chlorine Ion
DAQ	Data Acquisition
dB	Decibels
DC	Direct Current
DFT	Discrete Fourier Transform Operator
EM	Electromagnetic
FIR	Finite Impulse Response
FPGA	Field Programmable Gate Array
$f_s$	Temporal Sampling Rate
$H$	Hilbert Transform Operator
IDFT	Inverse Discrete Fourier Transform Operator
IIR	Infinite Impulse Response
$k$	Spatial Radial Frequency Variable
K <sup>+</sup>	Positive Potassium Ion
$k_s$	Spatial Sampling Rate
L <sub>2</sub>	Least Squares Norm
LMS	Least-Mean-Squares
MLP	Multi-layer Perceptron
MNA	Modified Nodal Analysis
Na <sup>+</sup>	Positive Sodium Ion
$N_c$	Number of Channels
PRD	Percent Residual Difference
PSD	Power Spectral Density
RLS	Recursive Least Squares

$s$	Symbol for Spatio-Temporal Signal
SA	Stimulus Artifact
SEP	Somatosensory Evoked Potential
SFAP	Single-Fiber Action Potential
sinc	Function with a flat spectrum $\sin(\pi x) / (\pi x)$
SNR	Signal-to-Noise Ratio
$t$	Time Variable
RC Network	Electrical Network of Resistors and Capacitors
$v$	Velocity Variable
VCVS	Voltage-Controlled-Voltage Source
$x$	Space Variable in 1D Space
$\Delta t, \Delta x$	Temporal and Spatial Sampling Intervals
$\omega$	Temporal Radial Frequency Variable
$\delta$	Dirac Delta Function
$\lambda$	Wavelength Variable
$\mu$	Nerve Depth Under Skin Surface
$\Pi$	Rectangular Pulse Shape

# Chapter 1

## Introduction

### 1.1 SEP Measurements

Somatosensory evoked potentials (SEPs) are bio-electric signals that propagate through peripheral or central sensory nerves due to external stimulation. SEPs convey information about the state and integrity of the nervous system in the form of signal features of the SEP waveform. The presence of the SEP ensures that transmission is occurring along the nerve as it should when stimulated. The shape, latency, and amplitude of the SEP are indicators of the integrity and proper functioning of the nervous system. This is especially valuable during spinal surgery and may provide adequate diagnosis for Carpel Tunnel Syndrome, Nerve Root Compression Syndrome and possibly other neuromuscular disorders [1], [2].

Typically, the stimulus is delivered via a current pulse applied to the tissues directly above the nerve. If the amplitude and duration are sufficiently large, the stimulus will evoke an action potential in the nerve of interest and initiate SEP propagation. This SEP waveform may be measured at a location down the nerve from the skin surface using electrodes at locations where the nerve is relatively close to the skin such that the SEP amplitude at the skin surface is sufficiently large. Typically the SEP measured from the skin surface on the median nerve has an amplitude on the order of a few microvolts [3], occupies a bandwidth from 10 to 3000 Hz, and propagates between 10 and 100 m/s. Due to the small amplitude, SEP measurements are difficult to distinguish from the noise floor. Ensemble averaging is a powerful technique that is used for increasing the SNR of small, noisy, repetitive signals such as the SEP. Many time-aligned repetitions of the measurement are taken and then averaged

together; this reduces uncorrelated noise such as electronic, myo-electric, cardiac, and power-line interference. The SEP of the median nerve can be measured at the wrist and the elbow pit where the nerve is superficial. At other locations the depth of the nerve bundle is too large to provide sufficient amplitude at the skin surface.

The stimulus artifact (SA) is the result of electrical stimulation provided to the nerve using surface electrodes. In addition to the nerve, the surrounding body tissues also draw current from the stimulator. The stimulus pulse thus propagates and appears at the skin surface in addition to the SEP recording. In configurations where the recording site is close to the stimulation site, it is often found that the tail component of the large SA extends well into the SEP, introducing significant distortion to the required SEP measurement. Figure 1-1 illustrates a SEP measurement from the median nerve that is corrupted by the SA.

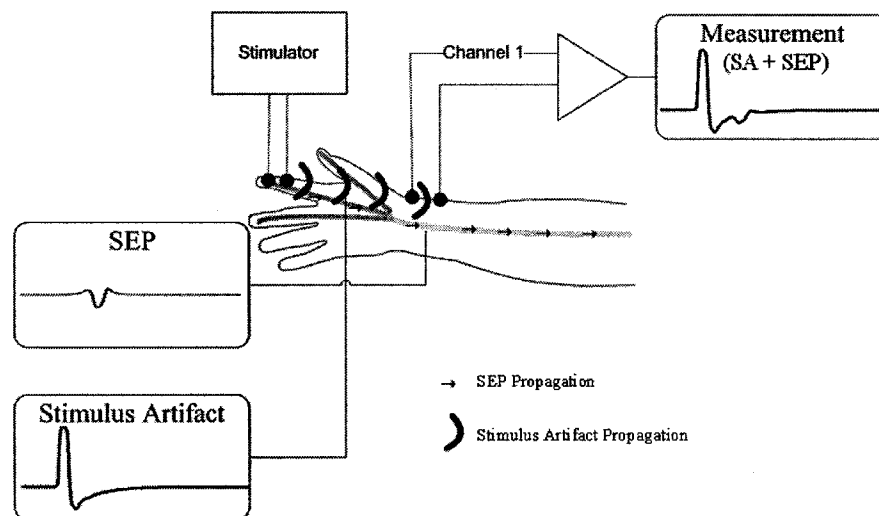


**Figure 1-1: Median nerve SEP measurement configuration**

This SA is problematic because it overlaps the SEP in time and frequency and is orders of magnitude larger than the SEP. Although ensemble averaging significantly reduces noise

from sources that are uncorrelated with the SEP, the SA cannot be removed this way because it is coherent with the SEP. It has thus become a topic of research to find effective post-processing methods for SA cancellation.

Improved SEP measurements may be obtained using needle electrodes because they are more spatially localized; however, our aim is to make the measurements noninvasive. The use of noninvasive surface recording electrodes removes discomfort for the patient and also the risk of infection. With the availability of a robust and easy to use SA cancellation method, undistorted SEP measurements may be readily obtained, allowing for improved confidence and less uncertainty in diagnostics based on clinical SEP records.

## **1.2 Current SA Reduction Techniques**

Early work in stimulus artifact reduction focused on ways to physically mitigate the SA using hardware techniques. These include custom design of recording amplifiers and stimulators, shielding the recording instrumentation from the stimulator, selection of the type of stimulation, using a large electrode size and Ag/AgCl electrodes [1], [4]. As explained in Section 2.3, these efforts have helped to reduce the SA in SEP recordings, but a large, coherent artifact remains due to the unavoidable spread of the stimulus pulse through body tissues between stimulating and recording electrodes surrounding the nerve. It is generally accepted that the SA is an unavoidable consequence of using electrical stimulation. It cannot be avoided, but can be removed from measurements by post-processing with some degree of success.

The state of the art methods for SA cancellation to date are based on nonlinear adaptive noise cancellation (ANC). These methods are treated in Chapter 2. The two available nonlinear ANC methods are called: segmented training [5] and sub-threshold training [6]. In both of these methods, a classical ANC scheme is used as shown in Figure 1-2 in which the adaptive element is an artificial neural network (ANN). The two methods differ in the nature of the data that they are trained with and used with.

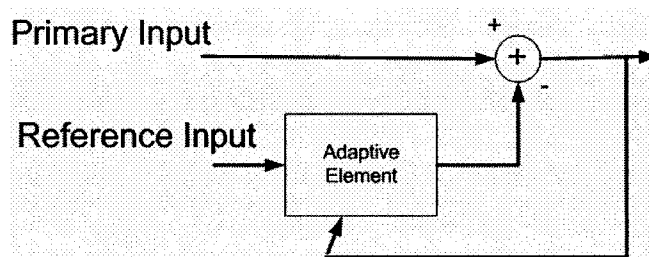


**Figure 1-2: Adaptive noise cancellation scheme**

In the classical ANC scheme, an adaptive algorithm such as least-mean-squares (LMS) or Recursive Least-Squares (RLS) is used to adapt the parameters of the adaptive element in such a way as to minimize the difference between the primary input and the reference input. Thus the filter models the relationship between the primary and reference channels, or maps the reference to the primary channel [7].

In segmented training, a reference channel is measured at the same time as the SEP measurement. The reference channel is located off of the nerve and contains no SEP but an SA that is correlated with that in the primary channel. The ANN is trained to learn the relationship between the SA in the primary and reference channels for the time samples up to the onset of the SEP. It then generalizes this relationship over the remaining time period to

estimate the remaining portion of the SA in the primary channel. This estimate of the SA in the primary channel is then subtracted from the primary channel to produce an estimate of the SEP. This is illustrated in Figure 1-3.

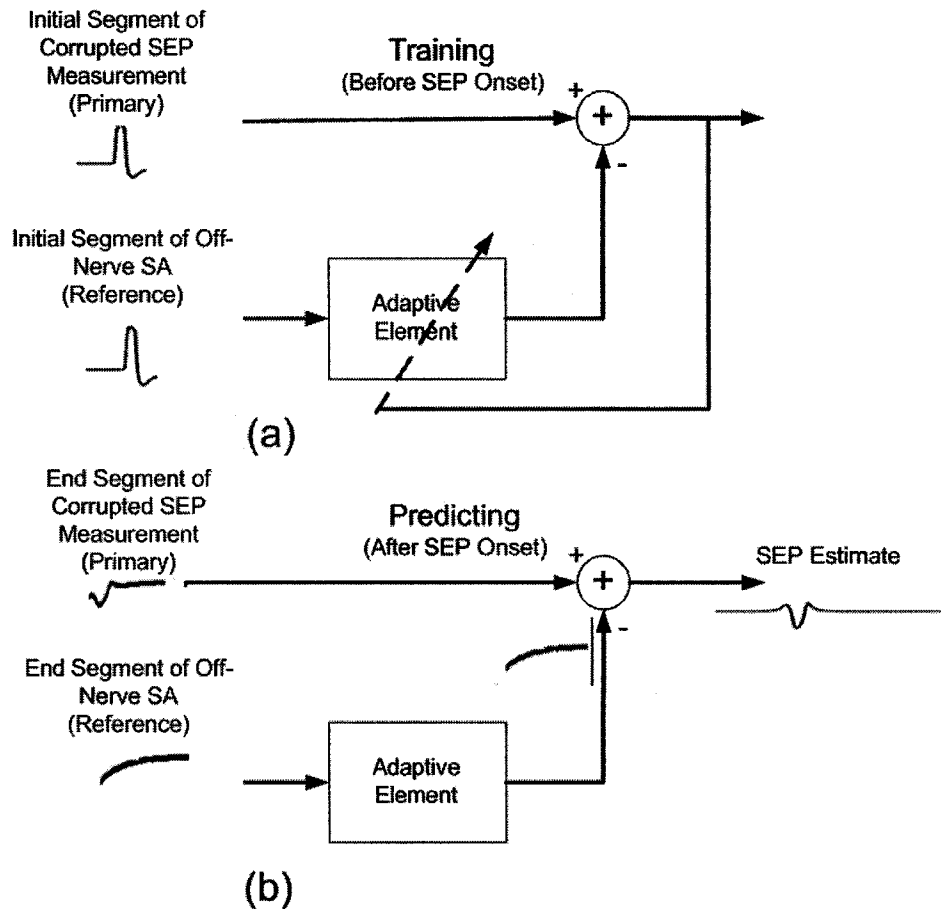


**Figure 1-3: ANC scheme used in segmented training, (a) training, (b) predicting**

In sub-threshold training, the ANN learns the relationship between stimulus level and the associated SA waveform and this relationship is learned over all time samples but for sub-threshold stimulus levels where no SEP exists. Here, the threshold refers to a minimum stimulus level required to activate the nerve. The ANN then generalizes this relationship to the supra-threshold case in order to estimate the SA at a supra-threshold level to obtain an

estimate of the SA in the primary channel at a supra-threshold stimulus level. This SA estimate is then subtracted from the SEP measurement to produce an estimate of the SEP. This is illustrated in Figure 1-4.

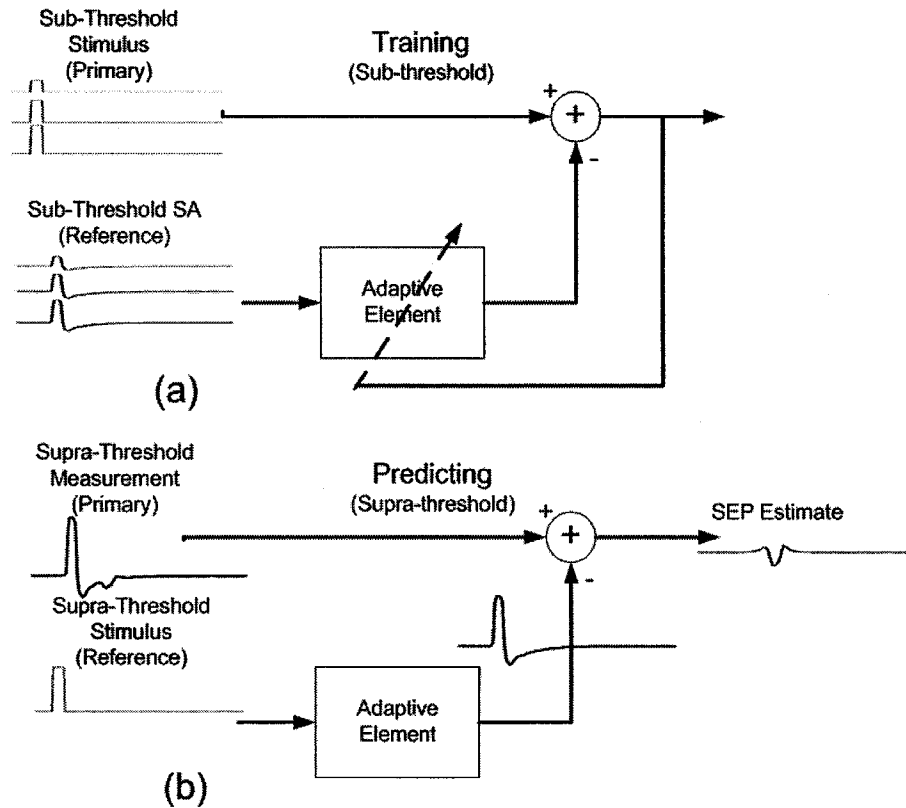


**Figure 1-4: ANC Scheme used in sub-threshold training, (a) training, (b) predicting**

The segmented training method is faster and straight forward to implement, but performance is not reliable, and is very sensitive to many factors. This will be discussed in detail in Section 2.3, but essentially it suffers from the need to generalize over time. Sub-threshold training overcomes this time generalization problem and has a more robust performance. The limitations of this method however are the fact that data collection is time-consuming as

recording must be done at multiple stimulus levels, and it still relies on the ability of the ANN to make accurate predictions which is not always reliable.

In both segmented and sub-threshold training, after good data are obtained, the ANN must then be trained and since the ANN is a nonlinear system, there is no guarantee of convergence or stability and there is the possibility of under or over-training. Time-consuming trial and error and human judgment are also required to choose a data size, network size and structure, and to supervise the training process. Furthermore, when satisfactory training is achieved, the SEP estimator is only valid when using a measurement setup that is identical to the one used for gathering training data including electrode impedances, locations, temperature, and stimulus intensity; hence, the training process must be repeated for each different subject and potentially for each measurement even with the same subject. These limitations make the nonlinear ANC-based SA cancellation methods non-ideal for a clinical setting. To have clinical significance, SA cancellation during SEP monitoring and clinical diagnosis must occur in real-time or at least within a short time after measurements are taken, and the system must work for general measurements without requiring training for each individual case.

### **1.3 Thesis Objective**

The objective of this thesis is to attempt to develop an effective SA cancellation method that overcomes the limitations of the current nonlinear ANC methods. Ideally, the system should be cheap, efficient, effective, and able to work in real time or at least yield results quickly and reliably without the need for human intervention and judgment.

In this thesis, we note that a key distinguishing factor between the SA and SEP is their propagation velocity. As the SA is mainly a result of the spread of current density from the stimulus pulse through extra-cellular media, it propagates near the speed of light. The SEP on the other hand is a potential field generated not by electromagnetic (EM) propagation, but by charged ions crossing a semi-permeable membrane of the axons comprising the nerve due to dynamic diffusion gradients across the axon membranes that are induced by the stimulus. It is well-known that ion flow is much less mobile than varying EM fields and accordingly, evoked potentials in the nervous system propagate much slower than electrical phenomena. In the median nerve under study, conduction velocity is less than 100 m/s [3] and varies across subjects. It is our aim to take advantage of the vast difference in propagation velocities of the SA and SEP a key distinguishing feature in order to separate them.

In order to operate on the velocity of a signal, information is required regarding not only how it varies with time, but also with space. The SEP is measured as array data that is sampled in time and in space at discrete spatial locations. The operator used to discriminate based on apparent velocity along the array axis is a spatio-temporal filter called a velocity filter. The two-dimensional (2D) filter is called a fan filter because of the shape of its frequency response.

The goal of this thesis is to develop the concept of velocity filtering as a means of SA cancellation and to examine whether it is a practical choice for real-time SA cancellation in clinical SEP monitoring. The motivation is that the system may be automated and run properly without requiring human judgment or intervention. It also has the advantages of being straight forward to implement as an FIR filter that is linear, time-invariant and

produces results that are deterministic, repeatable, and insensitive to features other than propagation velocity.

#### **1.4 Thesis Organization**

A literature review is given in Chapter 2 outlining the nature of the SA and SEP, the problem of the SEP being distorted by the SA, and previous methods of SA cancellation. In Chapter 3, the concept of velocity filtering is introduced, its theoretical basis is developed and some practical issues are identified and studied. Chapter 4 presents a simulation study using sinc pulse signals propagating at different velocities. Sinc pulses are chosen because of their spectrum that excites all frequencies up to the Nyquist frequency. This chapter is intended to demonstrate the agreement of the theory with application under simplified conditions, and examine the effects of system parameters such as the number of available channels. A simulation study is given in Chapter 5 using simulated SA and SEP signals that more closely resemble real measurements in the absence of random noise and spatial SEP variations. This allows the performance of the SEP estimate to be measured quantitatively and compared against a nonlinear ANC method using segmented training because the ideal SEP is known *a priori*. In Chapter 6, the velocity filter is applied to real SEP array measurements for 10 subjects and compared against segmented training using 3 quantitative performance metrics defined in [6]. Chapter 7 concludes the thesis with conclusions in the form of a summary, contributions, and future work and recommendations.

## **Chapter 2**

### **Literature Review**

#### **2.1 Motivation for Obtaining Undistorted SEP Measurements**

SEPs are electric potential fields that are induced in sensory nerves in response to a sensory stimulus [8]. They convey valuable information from sensory nerves to the central nervous system. Information about the integrity of the nervous system can be determined from the SEPs amplitude and latency [1]. An increase in SEP latency indicates slower propagation which may signify pathology [9]. A damaged or malfunctioned nerve can be detected by the decrease or disappearance in SEP amplitude [2]. The amplitude and duration also conveys valuable information about the distribution of axons and their conduction velocities in the nerve bundle. Some clinical applications of SEPs include the diagnosis of nerve root compression syndrome [10] and median nerve injuries such as Carpal Tunnel Syndrome [11]. SEPs are useful for spinal cord monitoring during surgery [4]. They can also be used to detect silent lesions in multiple sclerosis patients and focal interruptions in nerve pathways [2].

It is also of theoretical importance to obtain undistorted, accurate SEP measurements. Theoretical models of the SEP process may be validated more accurately against real measurements and possibly revised to account for limitations, providing more detailed scientific insight. With the availability of undistorted SEP measurements, common signal analysis and processing methods may also be applied to SEPs in a more practical and

systematic manner and the uncertainty in the apparent SEP waveform features that are obscured by distortion can be considerably reduced.

## **2.2 Difficulties with Stimulus Artifact in SEP Measurements**

Ensemble averaging is a powerful tool for SNR enhancement for noisy, repetitive signals such as the SEP. Because the SEP is so small (typically a few microvolts), it is normally buried in background noise. Ensemble averaging significantly increases the SNR of small, noisy, repetitive signals. This SNR gain is proportional to the square root of  $N$ , requiring 400 records for a 20 times enhancement [3] where  $N$  is the number of trials. While ensemble averaging helps reduce uncorrelated noise, such as electronic, myoelectric, cardiac, and power line interference, it cannot reduce noise that is coherent with the SEP. In our measurement setup, the SNR can typically be increased from levels roughly on the order of 0 dB to 10 dB. The remaining distortion is mainly due to the SA because it is coherent with the SEP and therefore is unaffected by ensemble averaging.

To evoke an SEP, the stimulus is usually supplied in the form of an externally applied electric current. This can be accomplished using two surface electrodes placed on the skin, with one acting as a source and one as a sink. This type of non-invasive current stimulation depolarizes the local membranes of the nerve fiber axons from their resting states, and initiates the propagation of action potentials through the axons [3]. In this work, bipolar electrodes are used for SEP recording. The potential associated with the SEP is recorded at a location down the nerve using bipolar electrodes placed on the skin surface [12]. This is shown in Figure 2-1.

The distributed impedance of the body tissues load the stimulator giving rise to the spread of stimulus current density which flows through the tissues between the stimulus and recording sites. The SA is a manifestation of the stimulus pulse that appears at the recording site after propagating through the tissue.

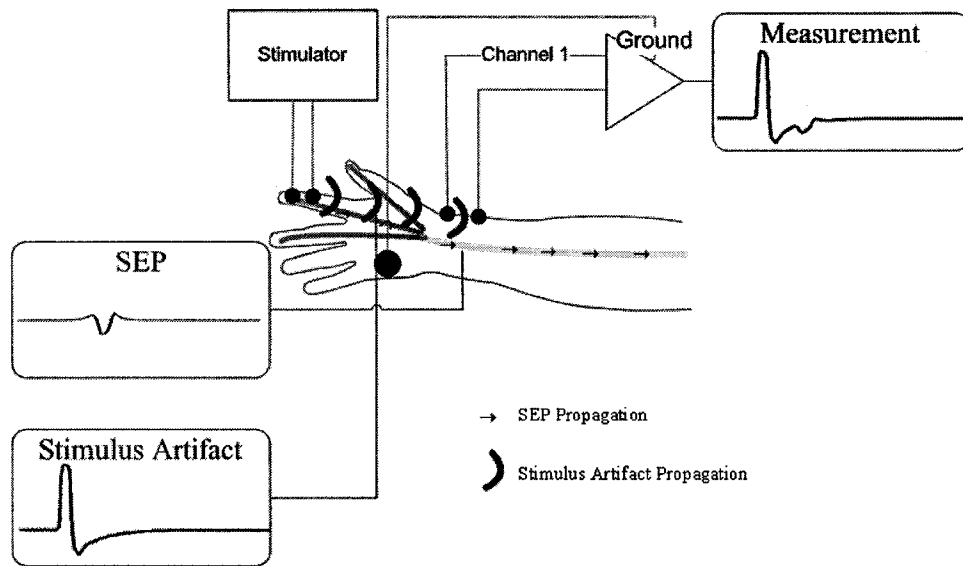


**Figure 2-1: Median nerve SEP measurement configuration**

Depending on the choice of stimulator, electrodes, amplifier, and the distance from stimulus to recording sites, the duration of the tail component of the SA in Figure 2-1 often exceeds the SEP latency and causes significant distortion to the SEP measurement [1], [2], [13].

The SA normally has a large initial spike, followed by a slowly decaying tail component [6], [13]. Although the large spike portion of the SA is fairly localized in time and short in duration, it is the slow tail component that usually temporally overlaps the SEP. Although the tail component is comparatively smaller than the fast spike portion, it is still considerably

larger than the SEP. This distorts the SEP measurement as shown in Figure 2-1, leading to a great deal of uncertainty in basic signal features of the SEP such as amplitude and latency.

It is generally accepted that the SA generation mechanism contains nonlinearities and exhibits large variability across different subjects and different locations within a subject, [2], [13]. Therefore, the SA generation mechanism is not easily modeled in accurate detail. This presents the fundamental challenge of distinguishing the SA from the SEP in real measurements and accordingly, accurate SA cancellation cannot be achieved by using a model to predict the SA waveform *a priori*. One must carry out a full-wave electromagnetic analysis or extract parameter estimates from measurement to formulate behavioral models [14].

Major sources contributing to the SA are identified in [1], [4] as:

- voltage gradient through extra-cellular tissues from stimulation to recording sites
- capacitive coupling from stimulation to recording sites
- common-mode voltage due to unequal impedances of recording electrodes
- common-mode voltage due to escape current from the ground electrode
- high-pass filter effect of the recording amplifier

Time or frequency domain filtering cannot remove the SA because it overlaps the SEP in both time and frequency. Time domain ensemble averaging cannot remove the SA because it is coherent with the SEP. Time-frequency analysis cannot remove it because the SA and SEP are stationary processes with frequency content that does not change over time [2], [13].

The high-pass filtering effect of the recording amplifier was identified in [13] as being largely responsible for the SA tail. Even as the amplifier is designed to pass very low frequencies, DC voltages are not passed by Ag/AgCl recording electrodes [8]. The Ag/AgCl electrodes are necessary for measuring small signals that are embedded in a background of noise because of their low-noise characteristics [8].

Using electrodes with a large surface area provides greater sensitivity to the small SEP measurement, but unfortunately this is also true for the SA in the measurement and so the SNR is not increased. Using constant-current versus constant voltage stimulation helps to keep the SA constant when stimulating electrode impedances change over time [15]; however, this does not reduce the SA. Physically shielding the recording instrumentation from the stimulator can reduce coupling through the air of the stimulus pulse to the recording electrodes; however, the main source of coupling occurs through the tissue. Using the shortest possible stimulus duration and fast rise and fall times, but still sufficiently long to evoke an SEP, also helps to reduce the SA [13]. In spite of these efforts, a large, coherent artifact remains due to the unavoidable spread of the stimulus pulse through the body tissues between stimulating and recording electrodes surrounding the nerve.

In summary, the SA is seen as an unavoidable consequence of using noninvasive electrical stimulation and recording. This view has brought about the recent research on post-processing of SEP measurements to remove the SA *a posteriori*. Many signal processing methods based on ANC schemes have been applied to remove the SA from SEP measurements [5], [6], [16]. These are described in the next sections.

Parametric curve-fitting techniques have been proposed and applied to fit exponential or sinusoidally decaying functions to the stimulus artifact tail, subtract this from the measurement, and obtain an SEP estimate. This method is not robust and inaccurate because the SA tail varies widely across subjects, stimulus intensity, electrode impedance and location and many other factors. These methods also suffer from and the assumption that the SA tail is exponential. Like the ANC methods, this method requires learning or parameter estimating for each separate measurement, but the ANC methods are still preferred because the model architecture allows more sophisticated models than exponential curves.

### **2.3 Adaptive Filtering of Stimulus Artifact**

ANC schemes are effective methods for SA reduction in SEP measurements. In this section, the two classes of nonlinear ANC based methods are described, segmented training, and sub-threshold training. In the classical ANC scheme of Figure 1-2, an adaptive algorithm is used to adapt the parameters of the adaptive element in such a way as to minimize the square of the difference between the primary input and the reference input using information fed back about the gradient of the error with respect to the parameters of the adaptive element. For adaptive elements that are linear systems, two common methods of weight adaptation are the LMS and RLS algorithms. The adaptive element models the relationship between the primary and reference channels, or maps the reference to the primary channel [7]. One of the many applications of ANC systems is for time-series prediction as in segmented training, or prediction of other signal features as in sub-threshold training. The adaptive element is first trained with a given set of data, and then used to generalize this relationship to data outside of this training range or data that was not seen during training.

### 2.3.1 Segmented Training

In segmented training, the reference channel is located off of the nerve and contains no SEP, but does contain an SA. The primary channel is located on the nerve and contains an SEP that is corrupted by the SA. The SA in the primary channel is correlated with the SA in the reference channel through a system  $H$ . The adaptive system has to learn  $H^{-1}$ , the relationship between the SA in the reference channel and the SA in the primary channel over the initial time period before the SEP occurs. It then generalizes this relationship across time using the remaining samples of the reference channel to estimate the remainder of the SA waveform and subtract it from the primary channel to yield an estimate of the SEP [5]. The general ANC structure used for segmented training is shown in Figure 2-2. Different computational architectures are shown in Figure 2-3; these are possible choices for the adaptive element to be used in the ANC scheme.

Using segmented training, linear FIR filter models as in Figure 2-3(a) were first explored in the classical ANC scheme for reducing the SA. In [16], it was found that a second order truncated Volterra series model as in Figure 2-3(b) outperformed the linear model when both trained with an RLS algorithm. Here, the performance was evaluated in terms of the SA power ratio in the output and primary input while ensuring sufficient filter length and training convergence in the minimum mean squared error (MSE) sense. This result supports the view that there are inherent nonlinearities present in the SA generation mechanism, mainly arising from the nonlinearity of the skin impedance at large current levels on the stimulation site [2], [5], [17].

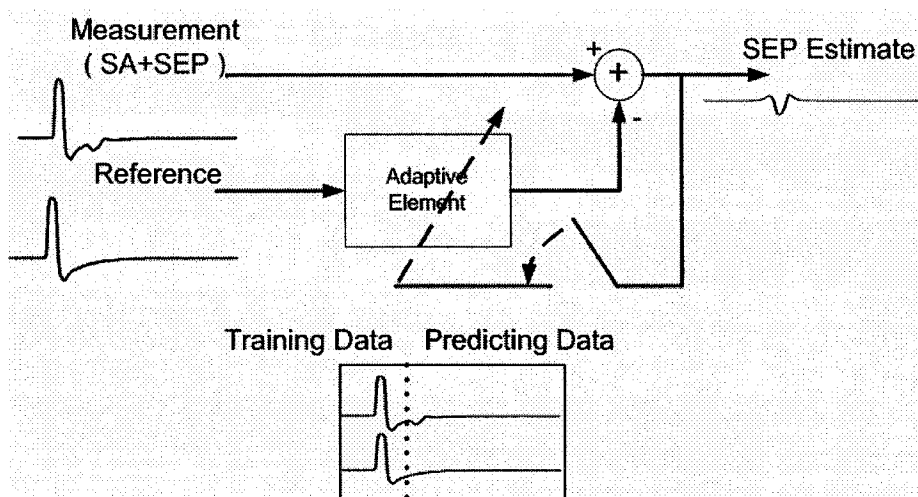


**Figure 2-2: Adaptive noise cancellation schemes for SA reduction**

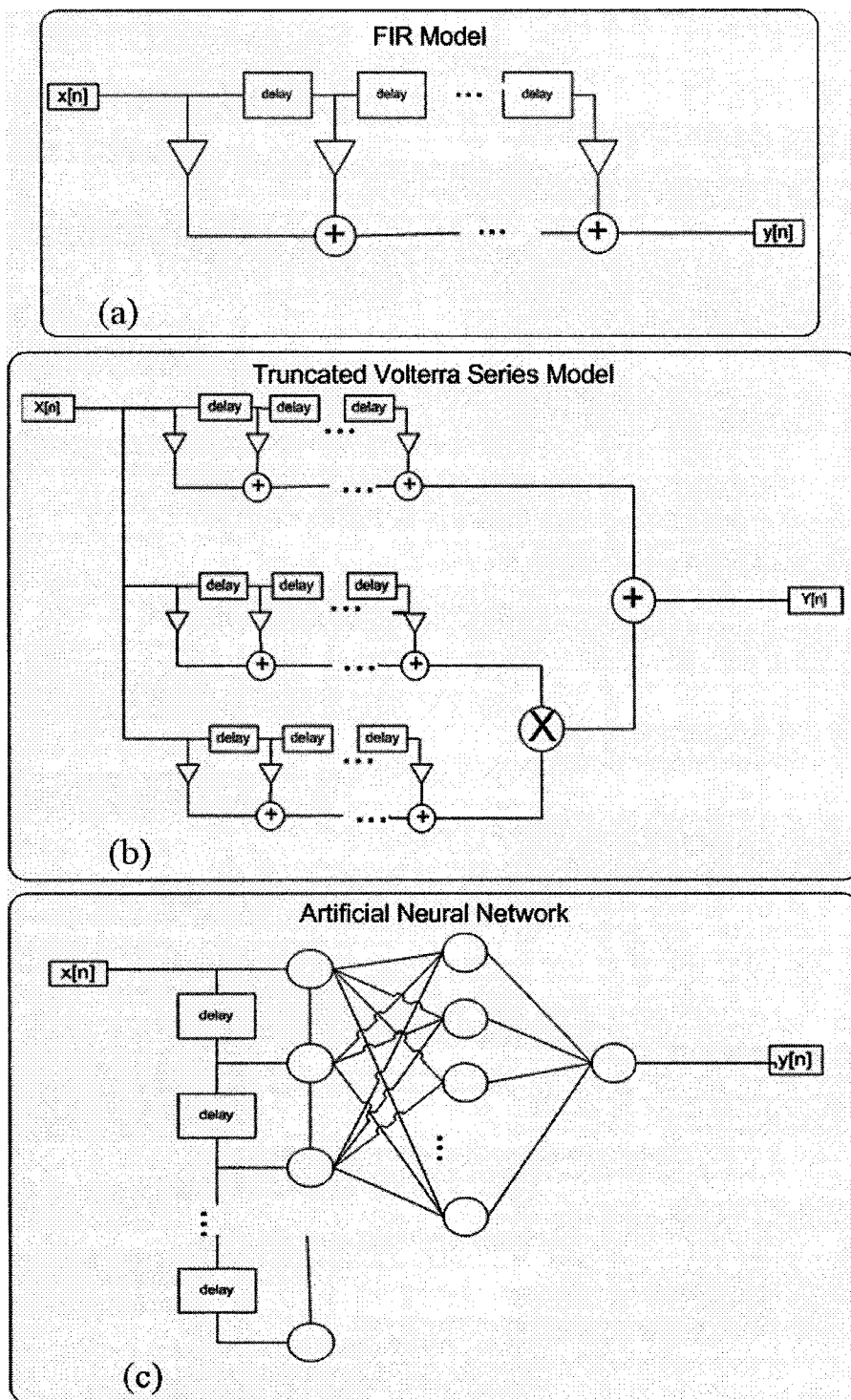


**Figure 2-3: Adaptive elements used in segmented training ANC schemes, (a) FIR filter, (b) truncated Volterra Series, (c) artificial neural network**

In [5], a nonlinear adaptive filtering method using an ANN with a multilayer perceptron (MLP) architecture and delays in the input layer as in Figure 2.3(c) was introduced as the nonlinear adaptive element in the ANC scheme for SA cancellation. When accurate training is achieved, this model has the following advantages over the Volterra series model. Training and feed-forward computation may be evaluated with greater speed and less computational demands due to the ANN's efficient architecture and the availability of modern training algorithms based on back-propagation [18]. Furthermore, the ANN may model nonlinearities of arbitrary order as opposed to a truncated Volterra-based model. Assuming that "good learning" as opposed to "over learning" is achieved, the ANN provides excellent generalization capability outside of its training range [18].

One limitation of this approach is the introduction of nonlinear harmonics into the system, leading to uncertainty in the amount of training data required to unambiguously represent the output which may contain higher frequencies than the input. Also, the ANN structure's number of input delays, hidden layers and neurons may not be known in advance and there is no guarantee of training convergence or of stability even with small or adaptive step sizes. A trial and error approach must therefore be used before arriving at a satisfactory result. The limitation of requiring the ANN to generalize across time is overcome by sub-threshold training.

### **2.3.2 Sub-Threshold Training**

In sub-threshold training, temporal generalization of the ANN is not used. Instead it learns the relationship between the stimulus level and the SA waveform, or the nonlinear mapping

from stimulus pulse to SA at different stimulus intensity levels [6]. This relationship is learned over all time samples for a family of different stimulus levels that are sub-threshold meaning that the stimulus artifact is isolated because the stimulus is not sufficiently strong to evoke action potentials in the nerve axons. Figure 2.4 illustrates this process.

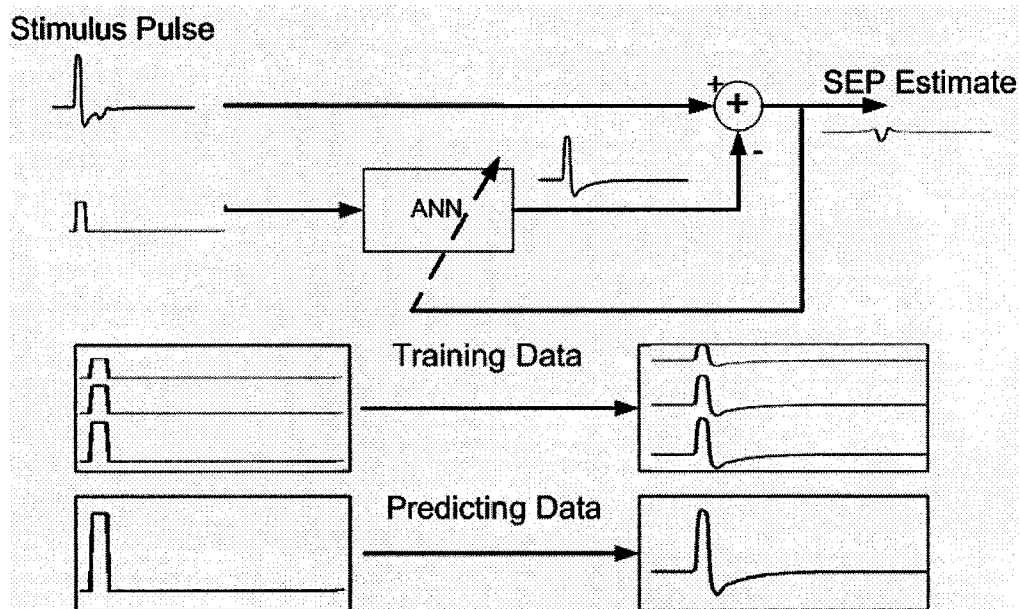


**Figure 2-4: Sub-threshold method of ANC for SA reduction**

The ANN learns the relationship between stimulus level and the SA waveform over all time samples, and generalizes this relationship outside of the training range to the supra-threshold case to estimate the supra-threshold SA waveform and subtract it from the measurement. This technique is not limited to relying on the network's generalization ability over time, but instead over stimulus intensity. The nonlinear dynamics of this relationship appear to be simpler than the temporal SA off-nerve to on-nerve relationship, and consequently the ANN is expected to have a higher chance of learning the mapping more accurately. Similar limitations exist concerning the nature of ANN's and uncertainty involved with their use

requiring human supervision. Another problem is that collection of the training data requires care and time to minimize measurement error, while keeping all other environment parameters constant except for stimulus intensity. The accuracy of the ANN's generalization will also be a strong function of the range of stimulus intensities covered by the training data set and number of stimulus levels in the set. A linear approximation was also attempted in [6] to model the relationship between stimulus intensity and SA waveform. Although this avoids the limitations associated with the use of ANN's, the linear model only partially captures the relationship which is nonlinear [6] thus limiting the accuracy that can be achieved in the SEP estimate.

## **2.4 Motivation for Velocity Filtering**

In this thesis, a velocity filtering method is introduced. The proposed method does not train an adaptive model to estimate the SA waveform. Instead, it incorporates spatial information to deduce differences in propagation velocities of the SA and SEP that are used to separate them. This approach has the advantage of making SA reduction more systematic because the system used has a static architecture and may be used online without human intervention. The goal of this work is to exploit propagation velocity as the key distinguishing feature between the SA and SEP.

The current-voltage dynamics of the SA generation process are not fully understood. In [14], parameterized behavioral models are fit to real measurements to estimate the parameters of a lumped circuit model. This model accounts for the transformation of the square stimulus current pulse to the SA waveform at the measurement site. For the purposes of justifying the

use of velocity filters, it is sufficient to say that the SA and SEP propagate with different velocities, regardless of the dynamics of the SA generation mechanism.

The SA is mainly due to the spread of stimulus current density and capacitive coupling from the stimulus to recording sites through the extra-cellular tissue and therefore its propagation is electromagnetic in nature traveling relatively close to the speed of light ( $\sim 3 \times 10^8$  m/s).

The potential associated with the SEP as seen from a pair of bipolar electrodes on the skin surface is a manifestation of the action potential phenomena in neural tissues. It is thought of as the superposition or distribution of action potentials from a large bundle of individual axons composing the large nerve. These potentials are the result of current flow carried by ions ( $K^+$ ,  $Cl^-$ , and  $Na^+$  are the main ions involved) as they carry net charges across the cell membranes [8], and induce the same net effect in their neighboring regions. This is so because the ions follow their diffusion gradients which change dynamically when a stimulus disrupts the trans-membrane potential from its equilibrium resting state. The net SEP potential progresses in a regenerative manner down the fiber by depolarizing its neighboring regions in a distributed fashion [8]. The macroscopic electrical dynamics mimic lossless transmission as in an ideal transmission line, but with much slower propagation velocity. The key physical characteristic is the propagation velocity of the SEP which is much less than that of SA. This is because ion flow has much less mobility than varying EM fields, and as such, bio-electric potentials propagate at very low speeds in neural tissues [3].

The nerve examined in this thesis is the median nerve because it presents a practical situation in nerve conduction studies in which the SA and SEP overlap in time when stimulating at the

index finger and recording at the wrist where the nerve is superficial as in Figure 2.1. This particular measurement setup may also be used as an indicator of Carpal Tunnel Syndrome [2]. The conduction velocity in the median nerve and most large myelinated peripheral nerves is typically between 10 and 100 m/sec [3].

The remainder of this thesis is concerned with exploiting the difference in propagation velocities of the SA and SEP as the key distinguishing feature between them. With spatio-temporal information of the SA and SEP, they may be clearly distinguished in the 2D frequency domain. The mechanism proposed here for separating the SA and SEP signals, is to employ a 2D velocity filter. The filter is 2D in nature operating on an array of SEP measurements. The signals are treated not as spatially localized functions of time, but as functions of time and space in order to resolve velocity information.

## Chapter 3

### Velocity Filtering

#### 3.1 Spatio-Temporal View of Signals

Electrical signals are normally thought of as spatially localized functions of time. When propagating signals are measured at different locations in 1D space, they possess a 2D wave nature and may be viewed as functions of time,  $t$  and distance,  $x$ . Discrete spatio-temporal data are treated as sampled-time signals, but using a 2D matrix rather than a 1D vector because space is also sampled. Just as the index of a 1D vector denotes the amplitude at a location in time, a discrete spatio-temporal signal uses 2 indices to denote the amplitude at a location in both time and space by the temporal and the spatial sample indices of a 2D matrix. The Nyquist criterion now applies in both dimensions simultaneously. In the time dimension the sampling rate must be at least 2 times the maximum temporal frequency contained in the signal, and in spatial dimension the spatial sampling rate must be at least 2 times the maximum spatial frequency contained in the signal. The first condition avoids temporal aliasing, meaning that there is a minimum allowed sampling frequency required to avoid ambiguity in temporal frequency when time is sampled. The second condition avoids spatial aliasing, meaning that there is maximum allowed sensor spacing, or minimum spatial sampling rate required to avoid ambiguity in spatial frequency when space is sampled. Figure 3-1 portrays an array of SEP measurements as a spatial sequence of 1D functions of time, each measured at different locations along the axis of SEP propagation.

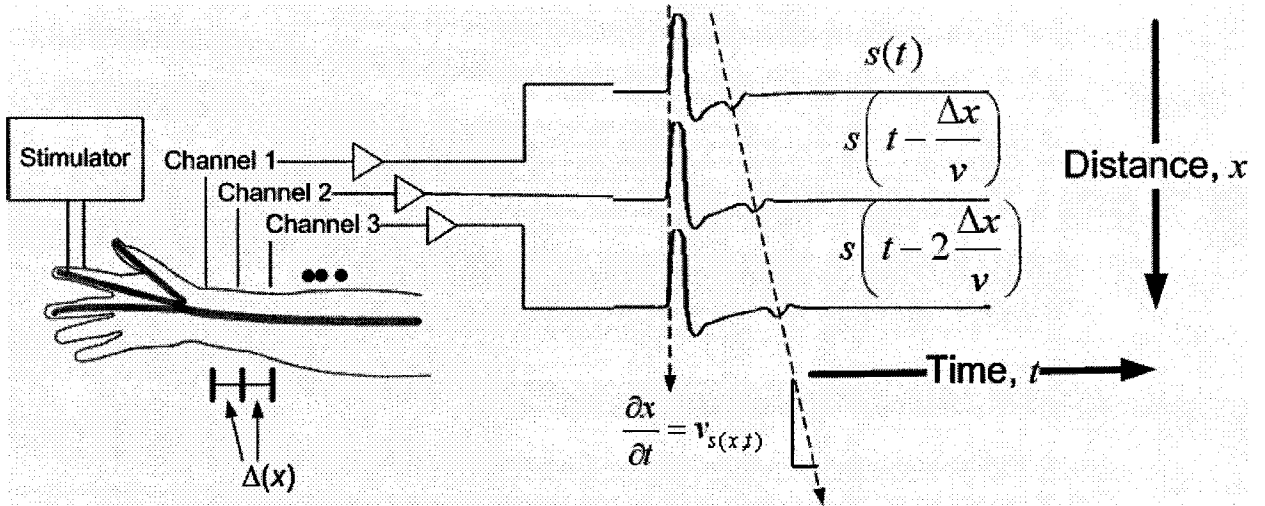


Figure 3-1: Sensor array data: constant velocity signal propagating along the array

The frequency content is interpreted in two orthogonal frequency axes: temporal frequency,  $\omega$  and spatial frequency or wavenumber,  $k$ . The  $k$ - $\omega$  spectrum of a space-time signal  $s(x, t)$  is computed by 2D Fourier Transform. The 2D Fourier Transform of a propagating signal is expressed mathematically using elementary Fourier Transform properties in Equation 3.1 assuming that no other spatial variation exists in the signal besides lossless propagation with constant velocity,  $v$ .

$$\begin{aligned}
 s(x, t) &= s\left(t - \frac{x}{v}\right) \\
 S(k, \omega) &= \int_{-\infty}^{\infty} \int_{-\infty}^{\infty} s(x, t) e^{-j\omega t} e^{-jkx} dt dx \\
 S(k, \omega) &= \int_{-\infty}^{\infty} \int_{-\infty}^{\infty} s\left(t - \frac{x}{v}\right) e^{-j\omega t} e^{-jkx} dt dx \\
 &= \int_{-\infty}^{\infty} e^{-\frac{j\omega x}{v}} \left( \int_{-\infty}^{\infty} s(t) e^{-j\omega t} dt \right) e^{-jkx} dx \\
 &= S(\omega) \int_{-\infty}^{\infty} e^{-\frac{j\omega x}{v}} e^{-jkx} dx \\
 &= S(\omega) \delta\left(k + \frac{\omega}{v}\right)
 \end{aligned} \tag{3.1}$$

For a signal propagating with very large apparent velocity,  $v$  is very large in the denominator and Equation 3.1 reduces to:

$$S(k, \omega) = S(\omega)\delta(k) \quad (3.2)$$

and the  $k$ - $\omega$  spectrum is equal to the 1D temporal frequency spectrum located above the  $\omega$  axis at  $k = 0$ , and zero everywhere else as in Figure 3.2. Thus for signals propagating along an array at the speed of light, each sensor will see the same signal and  $s(x, t) = s(t)$ , and

$S(k, \omega)$  looks like  $S(\omega)$  parallel to the  $\omega$  axis.

In the case of low apparent velocity, the  $k$ - $\omega$  spectrum is formed by tilting the 1D spectrum at a point in space into a second dimension,  $k$ , such that the projection of  $S(k, \omega)$  onto the  $k$ - $\omega$  plane lies parallel to the line  $\omega / k = v$  as in Figure 3.2 if the velocity is constant.

The practical significance of this result is that an observation of overlapping signals containing little or no distinguishing features in the time or frequency domains may now be clearly distinguished according to their apparent velocities by looking in the  $k$ - $\omega$  domain if spatial as well as temporal information is included in the description of the propagating signal.

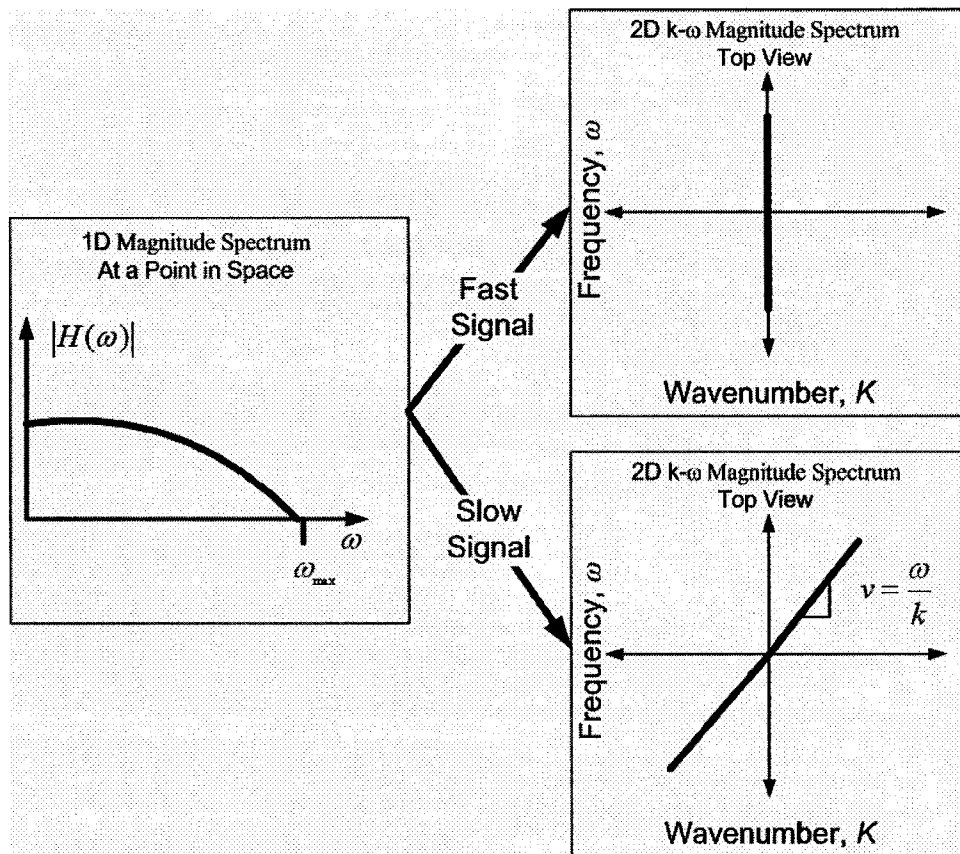


Figure 3-2: Effect of apparent velocity on  $k$ - $\omega$  magnitude spectrum

If apparent velocity is thought of in terms of frequency rather than time, then it is an expression of the rate of change of temporal to spatial frequency.

$$v_{s(x,t)} = \frac{\partial x}{\partial t} \xrightarrow[\left\{ \frac{\partial \omega}{\partial t} = \frac{1}{2\pi \partial t}, \frac{\partial k}{\partial x} = \frac{1}{2\pi \partial x} \right\}]{2D-FT} \frac{\partial \omega}{\partial k} = v_{s(k,\omega)} \quad (3.3)$$

For waveforms propagating at a constant velocity, this derivative is a constant. The projection of the  $k$ - $\omega$  magnitude spectrum onto the  $k$ - $\omega$  plane will then appear as a straight line whose slope is equal to its apparent velocity. Figure 3.3 illustrates the time-domain

traces and  $k$ - $\omega$  magnitude spectrum of the propagating sinc pulse signal in Equation 3.4 propagating with constant velocity,  $v$  in 1D space.

$$s(x,t) = \text{sinc}\left(t - \frac{x}{v}\right) \tag{3.4}$$

where  $\text{sinc}(\bullet)$  denotes a bandlimited sinc function,  $\text{sinc}(x) = \frac{\sin(\pi x)}{(\pi x)}$

Figure 3.3(a) shows the 10 center traces of a 30-trace signal with 5 mm sensor spacing. Each trace has a flat spectrum up to 5 kHz and is sampled at 45 kHz.

The trace-to-trace delay due to constant propagation velocity or the moveout is 3 samples per trace (76.9  $\mu\text{sec}$ , for 45 m/sec propagation with 5 mm spacing). The magnitude of the  $k$ - $\omega$  spectrum is plotted in dB in Figure 3.3(b), and contoured in Figure 3.3(c). With a linear phase, all frequency components lay on a straight line in  $k$ - $\omega$  space, the slope of this line is the apparent velocity.

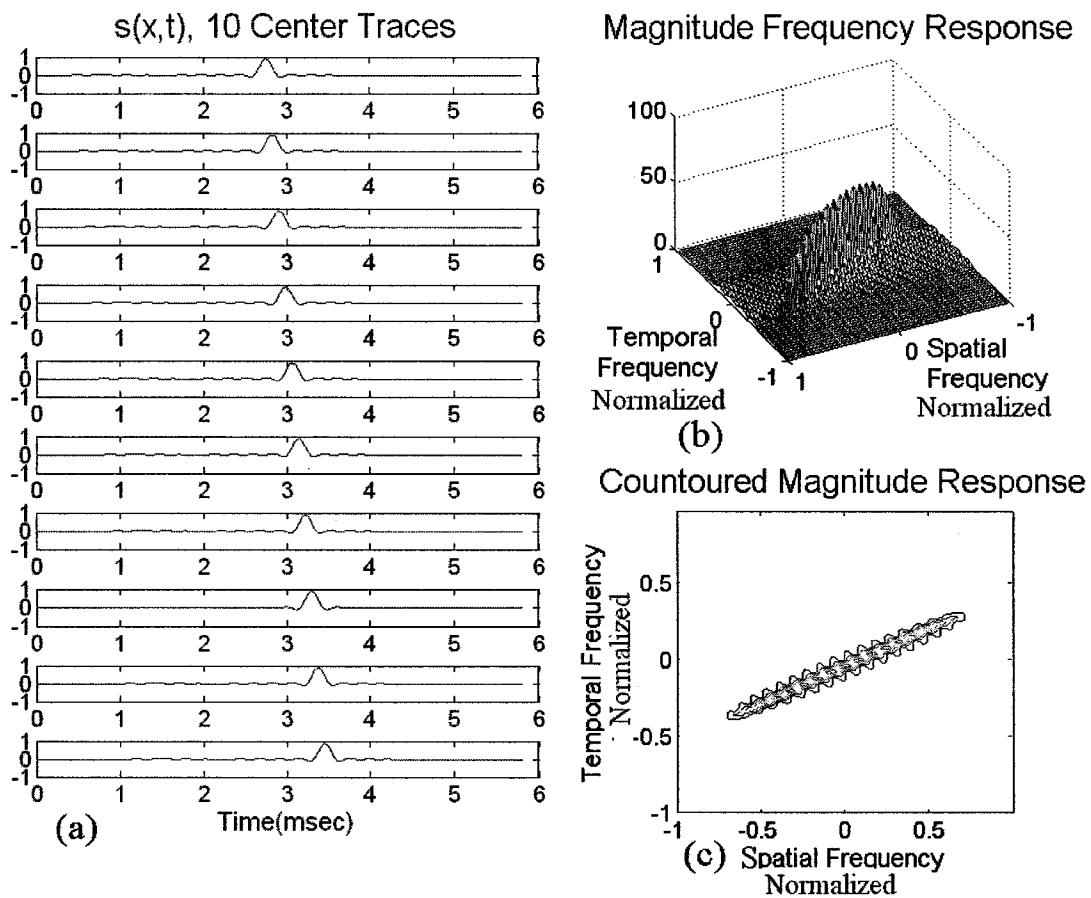


**Figure 3-3: 2D signal with constant velocity in  $(x, t)$  and  $(k, \omega)$  spaces, (a) time domain traces, (b)  $k$ - $\omega$  magnitude response, (c) contoured  $k$ - $\omega$  magnitude response**

Figure 3.4 demonstrates the effect of signals with different apparent velocities. The spacing and sampling rate are respectively  $\Delta x = 5.0$  mm and  $f_s = 26$  kHz. The propagation velocities are respectively: 25, 40, 65, and  $\infty$  m/s. This is equivalent to 5, 3, 2, and 0 sample moveouts. If the apparent velocity is large enough, the moveout is 0 samples long and the slope of the  $k$ - $\omega$  spectrum in the  $k$ - $\omega$  plane becomes parallel to the  $\omega$  axis and is interpreted as infinite velocity. In the upper two spectra for  $v_{apparent} = 25$  and 40 m/s, spatial aliasing is observed

due to low velocity with insufficiently small sensor spacing, and causes folding in the  $k$  dimension.

The channel spacing is 5 mm, the corresponding spatial sampling rate is:

$$\Delta x = 5 \text{ mm} \rightarrow k_s = \frac{1}{0.005} = 200 \text{ cycles/meter}$$

The maximum spatial frequency that can be represented is:

$$k_{\max} = \frac{k_s}{2} = 100 \text{ cycles/meter}$$

The highest spatial frequency contained in the data is:

$$k_u = \frac{f_u}{v}$$

and when  $v$  gets small,  $k$  gets large and folding occurs.

For  $v = 25 \text{ m/s}$ ,  $k_u = 5 \text{ kHz} / 25 \text{ m/s} = 200 \text{ cycles/m} > k_{\min} = 100 \text{ cycles/m}$ ,

similarly for  $v = 40 \text{ m/s}$ ,  $k_u = 125 \text{ cycles/m} > k_{\max}$ .

For the cases of  $v = 65$  and  $\infty \text{ m/s}$ ,  $k_u < k_{\min}$  and no aliasing occurs.

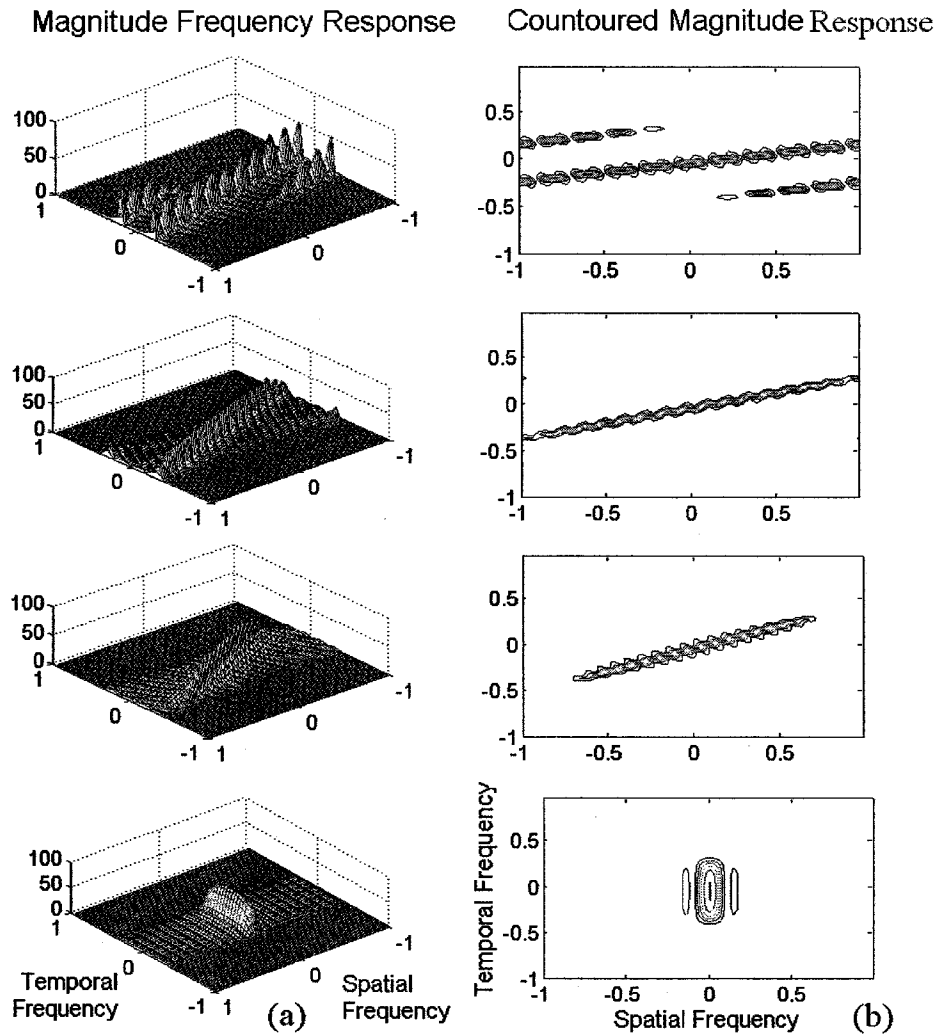


**Figure 3-4: Comparison of signals with different velocities in  $(k, \omega)$  space of 25, 40, 65, and  $\infty$  m/s (ordered top to bottom), (a) magnitude spectrum, (b) 2D contoured magnitude spectrum**

### 3.2 Theory of Velocity Filtering

Velocity filters were first reported by Fail and Grau [19] for attenuating coherent noise artifacts based on their apparent velocities or moveout in seismic array data. The 2D operator used to perform this function is called the fan filter, also known as the pie-slice filter, dip filter or wedge filter.

In the 2D  $k-\omega$  plane, the passband of the filter is defined by the pie-slice region bounded by the radial lines that correspond to the cut-off velocity. The stopband is defined as the remaining slice where velocities are less than the cut-off velocity. The fan filter passes low velocities, and attenuates high velocities as illustrated in Figure 3.5, where  $S_1$  through  $S_4$  are propagating signals in order of increasing velocity.

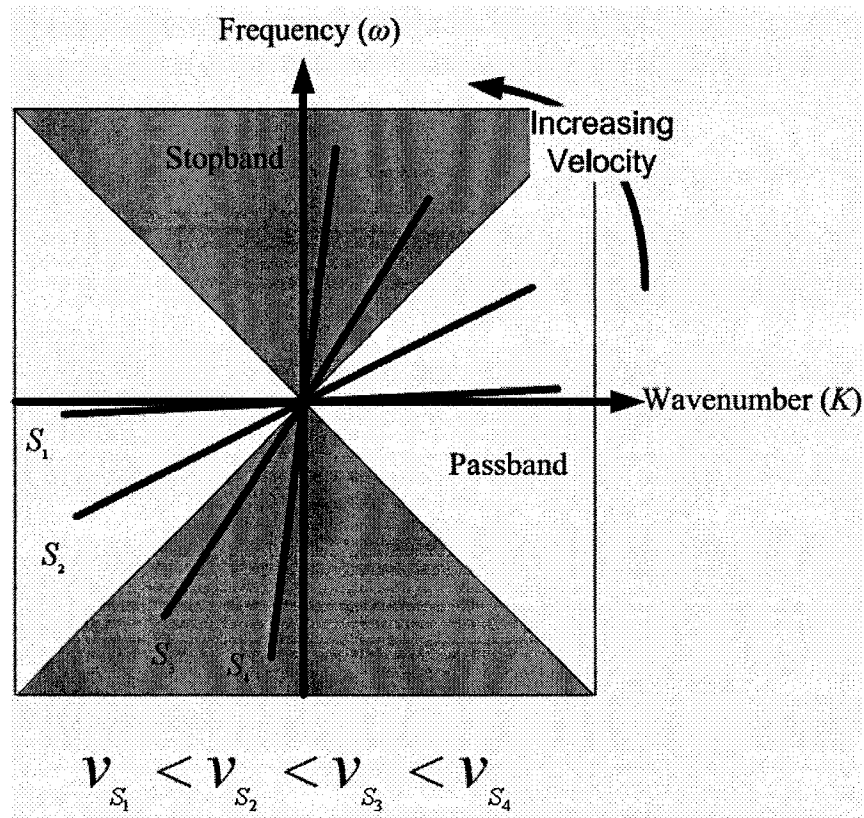


**Figure 3-5: Ideal frequency response of fan filter**

Realizations of the impulse response of such as filter have been derived in the literature [19], [20], [21]. Starting with a specification of the ideal frequency response:

$$H(k, \omega) = \begin{cases} 1, & \frac{|\omega|}{k} \leq v_C \\ 0, & \frac{|\omega|}{k} > v_C \end{cases} \quad (3.5)$$

Using a 2D inverse Fourier Transform, the ideal impulse response may be computed (Appendix A).

$$\begin{aligned} f(x, t) &= \frac{1}{2\pi} \frac{1}{2\pi} \int_{-\infty}^{\infty} \int_{\frac{|k|}{v_C}}^{\frac{|k|}{v_C}} e^{j\omega t} e^{jkx} \partial\omega \partial k \\ &= \frac{1}{4\pi^2} \frac{1}{t} \left[ \hat{\mathcal{D}} \left( x - \frac{t}{v_C} \right) - \hat{\mathcal{D}} \left( x + \frac{t}{v_C} \right) \right] \end{aligned} \quad (3.6)$$

where the hat indicates the Hilbert Transform Operator.

Using the Hilbert Transform Property:  $s_1(t) * H\{s_2(t)\} = H\{s_1(t) * s_2(t)\} = H\{s_1(t)\} * s_2(t)$  the Hilbert Transform may be directly applied to the data prior to filtering:

$$s(x, t) \rightarrow \boxed{\frac{1}{4\pi^2} H(\bullet)} \rightarrow \boxed{f(x, t) = \frac{1}{t} \left[ \mathcal{D} \left( x - \frac{t}{v_C} \right) - \mathcal{D} \left( x + \frac{t}{v_C} \right) \right]} \rightarrow y(x, t)$$

**Figure 3-6: Block diagram of velocity filter implementation**

This result is intuitively satisfying, but in reality the Dirac-Delta functions must be realized by band-limited approximations and the infinite impulse response must be truncated. This is the usual limitation in filter design; that is, filter order and complexity are traded off for roll-off rate and flatness in the passband. The implementation is most conveniently performed in discrete space and time. Various discrete approximations of this response have been reported

in the literature [19]-[22]. The filtering in two dimensions is accomplished using 2D linear, discrete convolution of the form

$$y[m,n] = h[m,n] * s[i,j] = \sum_{i=0}^{N_x-1} \sum_{j=0}^{N_T-1} h[m,n] s[i-n, j-m] \quad (3.7)$$

where  $h$  is the discrete fan filter impulse response,  $s$  are the array data, and  $m$  and  $n$  are the discrete space and time indices, respectively. The center-trace of the filter output  $y[m, n]$ , denoted by the 1D vector  $y[n]$  naturally provides the best velocity filtered output because it maximally utilizes all available trace-to-trace latency information of the propagating signals seen in the input data traces as shown in Figure 3.7(b). Figure 3.7(a) and (c) show that the off-center traces can only use symmetrical velocity information from less than the total number of input traces and are lower quality estimates of the SEP than the one located at the center trace.

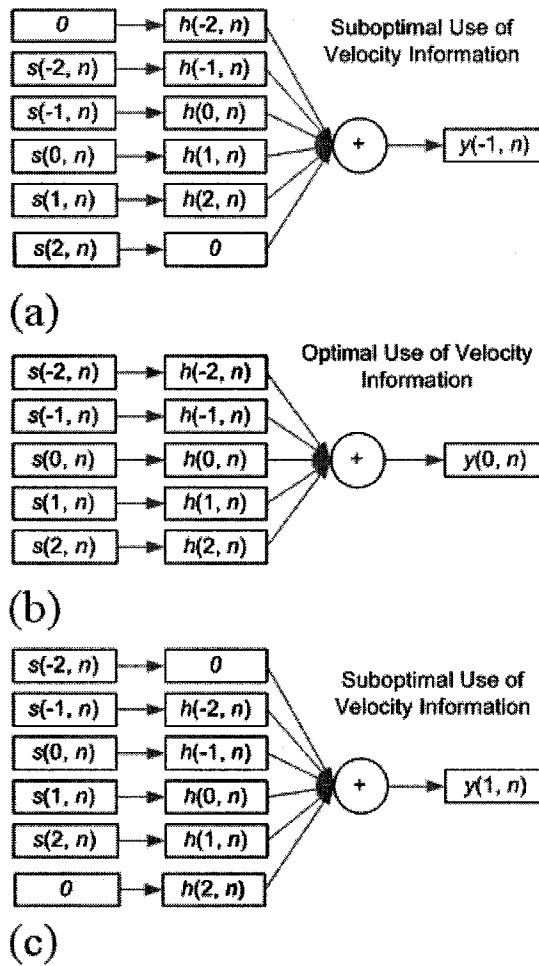


**Figure 3-7: Illustration of 2D convolution (a) computation of output trace previous to center trace, (b) center trace, (c) trace following the center trace**

When filtering 2D sampled data, an odd number of channels should be used for spatial symmetry in the array data symmetry so that no fractional-sample phase shifts are introduced [20] into the output traces. In this case, the center trace is the valid velocity filtered output which corresponds to the signal located at the center array location in space. The other output traces become useful when filtering multiple times because they will further contribute to the center trace estimate after the first convolution is performed.

### 3.3 Discrete Velocity Filtering

A finite impulse response (FIR) approximation of the ideal fan filter response was used in this work by truncating and windowing an inverse discrete Fourier Transform IDFT of discrete frequency points. The reasons for this choice are:

- to study velocity filtering without the stability problems involved with IIR filters
- the computation of filter coefficients is much simpler
- linear phase in the pass band (no group delay) is a requirement

A 2-D Bilinear transform [23], a McClellan transform [24], the Impulse Invariance method or other design synthesis procedures could also be used and may have different properties in terms of attenuation, distortion, stability and efficiency of implementation. For our purposes, the FIR fan filter approximation is generated by a grid of discrete frequency points that sample the ideal frequency response. An IDFT is used to compute a truncated FIR impulse response approximation followed by application of a 2D window. The filter size and window were chosen empirically to make the impulse response as short as possible, but without degrading the roll-off or introducing considerable ringing. The design is assuming that 11 data channels are available as in the usual case for SEP recordings on the wrist location of the median nerve, and so an 11 channel filter is sufficient to estimate the center trace. However, since we may pass the data through the filter multiple times to achieve greater SNR gains, using more than 11 channels will improve the estimate, and a filter size of  $21 \times 101$  is chosen empirically. The cutoff velocity line is chosen to be  $45^\circ$  between the  $k$  and  $\omega$  axes. This is because varying the sampling rate allows different choices of cut-off velocity

on the non-normalized frequency scale. Also, by choosing this value such that the passband and stopband occupy equal area in  $k$ - $\omega$  space, the dynamics of the system are simpler than another choice of cutoff velocity, requiring lower filter order to model. The filter design procedure is given below where frequency is normalized between -1 and 1 corresponding to +/- half of the sampling rate. Also, the choice of window functions was based on trial and error in choosing one that gave the most accurate numerical results, a topic of future work is to carefully design special windows to leverage the time localization of the SA.

1) Specify the ideal frequency response with zero phase (1001×1001 points). A large number of frequency points were chosen to approximate a continuous frequency response in order to improve the accuracy of the following Fourier Transform approximation.

$$G[k_x, k_t] = \begin{cases} 1, & \left| \frac{k_t}{k_x} \right| < 1 \\ 0, & \text{otherwise} \end{cases} \quad (3.8)$$

$-1 \leq k_x \leq 1, -1 \leq k_t \leq 1$

where  $k_x$  and  $k_t$  indicate the spatial and temporal discrete frequency indices.

2) Approximate the fan filter FIR impulse response using a 2D inverse discrete Fourier Transform (2D-IDFT).

$$g[n_x, n_t] = \frac{1}{N_x N_t} \sum_{k_x=0}^{N_x-1} \sum_{k_t=0}^{N_t-1} G[k_x, k_t] e^{j2\pi \frac{k_x n_x}{N_x}} e^{j2\pi \frac{k_t n_t}{N_t}}$$

$$n_x = -\frac{(N_x-1)}{2} \dots 0 \dots \frac{(N_x-1)}{2}, N_x = 21$$

$$n_t = -\frac{(N_t-1)}{2} \dots 0 \dots \frac{(N_t-1)}{2}, N_t = 101$$

(3.9)

3) A Hamming window is used in the time dimension to give the truncated response a smooth transition to zero. Note that this is not necessarily the best choice of windowing, but that is a topic for further investigation.

$$\tilde{h}[n_x, n_t] = g[n_x, n_t]w_H[n_x, n_t] \quad (3.10)$$

where the window function truncates the filter to  $21 \times 101$ .

$$w_H \left[ n_x + \frac{N_x + 1}{2}, n_t + \frac{N_t + 1}{2} \right] = W_1 W_2^T$$

The 1D Rectangular Window,  $W_1$  is given by:  $W_1[n_x] = \begin{cases} 1, & n_x = 0, 1, \dots, N_x \\ 0, & \text{elsewhere} \end{cases}$  (3.11)

and the 1D Hamming Window,  $W_2$  is given by:

$$W_2[n + 1] = 0.54 - 0.46 \cos \left( 2\pi \frac{n_t}{N_t - 2} \right), n_t = 0, 1, \dots, N_t$$

$W_1$  has a length of 21 and  $W_2$  has a length of 101. One might be tempted to use a window in the spatial dimension thinking that it can smooth the effect of spatial truncation due to a limited number of channels, but this is found not to be the case because the window would also destroy the spatial consistency in the amplitude propagating signal introducing distortion into the filter output.

Figure 3.8(a) shows the 10 center traces of the 2D impulse response of the resulting FIR approximation of the fan filter. Figure 3.8(b) and (c) show the magnitude and phase of its frequency response.

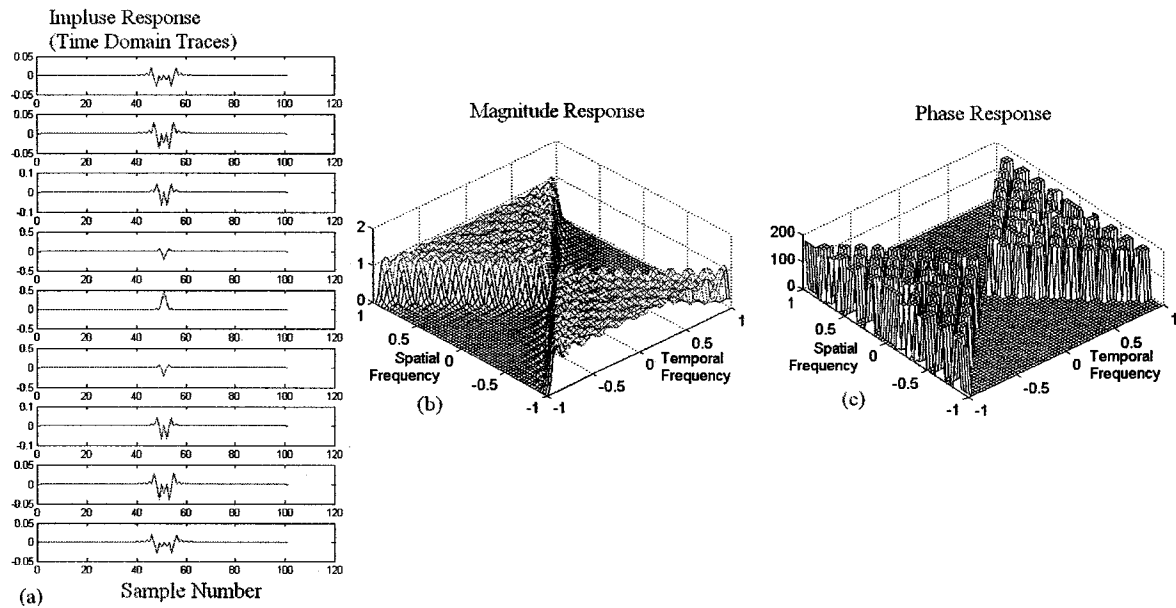


**Figure 3-8: Fan filter FIR approximation, (a) center traces of impulse response, (b) magnitude of frequency response, (c) phase of frequency response**

The FIR approximation has a phase that is close to zero in the passband, and piecewise-linear in the stopband. The magnitude response has some passband ripple and reasonably fast roll-off.

### 3.4 Practical Constraints

In order for the filter to effectively suppress the high-velocity coherent interference without distorting the low velocity signal, some trade-offs must be made to minimize low-velocity distortion and maximize stopband attenuation. Physical performance limiting factors are identified in this section and the effects of filter realization are quantitatively treated in the following sub-sections.

### 3.4.1 Spatial Resolution

In the median nerve, the propagation velocity of SEP's is on the order of 10 to 100 m/s. with a bandwidth roughly in the 1 to 3 kHz range [3]. The wavelengths are roughly in the range:

$$v = \frac{\omega}{k} \longrightarrow k = \frac{\omega}{v}$$
$$k_{max} \approx \frac{3 \text{ kHz}}{10 \text{ m/s}} = 300 \text{ cycles/m} \quad k_{min} \approx \frac{1 \text{ kHz}}{100 \text{ m/s}} = 10 \text{ cycles/m} \quad (3.12)$$
$$0.33 \text{ cm} \leq \lambda \leq 10 \text{ cm}$$

The superficial region of the median nerve at the wrist where the SEP may be effectively detected using Ag/AgCl electrodes from the skin surface is approximately 5 to 10 cm long depending on the subject. Using 11 channels, spaced by 5 mm and spanning a 5.5 cm measurements window over the median nerve at the wrist is roughly the most spatial information available about the SEP that can be measured from the skin surface. Outside this range, the SNR becomes too poor to contribute spatial information for use by the velocity filter.

In the time dimension, we may control the sampling rate and observation window length; however, in the spatial dimension the number of channels is limited to 11 by the nerve's superficial region and the physical electrode size (bipolar electrodes with 1.3 cm diameter). With an accurately manufactured array, finer electrode spacing may be available, but at the expense of smaller electrode area and lower SNR. Given this limited spatial observation window length, spectral leakage and loss of resolution will be suffered in the  $k$  dimension.

$$\begin{aligned}\hat{sep}(x,t) &= sep\left(t - \frac{x}{v}\right)\Pi\left(\frac{x}{\Delta x}\right) \\ \hat{SEP}(k,\omega) &= \left[SEP(\omega)\delta\left(k + \frac{\omega}{v}\right)\right] * \left[\Delta x \text{sinc}\left(\frac{k\Delta x}{2}\right)\right]\end{aligned}\tag{3.13}$$

where  $\Pi$  is the rectangular function and  $\hat{sep}(x,t)$  denotes a truncated approximation of  $sep(x,t)$ .

### 3.4.2 Velocity Resolution

Depending on the temporal sampling rate,  $f_s$ , and spatial rate  $k_s$ , propagation velocity is resolved by the number of samples  $M$  by which points in the waveform are shifted to the right between adjacent traces as they propagate.

$$v = \frac{\partial x}{\partial t} \xrightarrow{\text{sampled at } [f_s, k_s]} M \frac{\Delta x}{\Delta t} = M \left(\frac{f_s}{k_s}\right) = Mv_c\tag{3.14}$$

where  $\Delta x$  and  $\Delta t$  are the spacing and sampling periods and  $v_c$  is the fan filter cut-off velocity. As  $f_s$  is increased, the sampling error in moveout decreases and causes the spectrum to tilt towards the  $k$  axis and closer to passband center where there is less distortion. The spectrum will also be compressed and localized around the origin on a normalized frequency scale. It is better to spread the spectral energy out of this region because the FIR truncation of the fan filter causes more severe distortion at low frequencies [22]. This is because the discontinuities of the passband and stopband edges converge together at low frequencies as in Figure 3.9(a), implying very high filter orders required to accurately approximate the ideal response at these frequencies. Consequently, there is a tradeoff between tilting the signal further into the passband for less distortion, and the loss of low-frequency information.

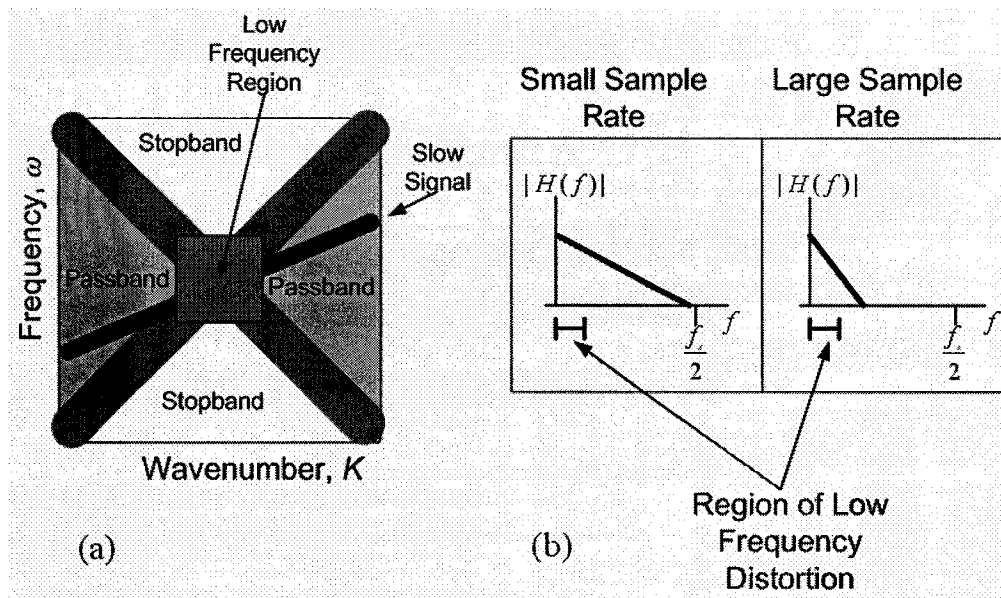


Figure 3-9: Illustration of velocity resolution, (a) 2D projection onto  $k$ - $\omega$  plane, (b) 1D illustration of low frequency distortion

### 3.4.3 Trace-to-Trace Consistency of Signal Features

The velocity filters described thus far rely on the assumption of trace-to-trace consistency or spatial invariance of the SEP made in Equation 3.1 which is restated in Equation 3.15. Signal features such as amplitude, trace-to-trace latency, and spectral content must not vary with distance along the array for ideal velocity filtering.

$$s(x,t) = s\left(t - \frac{x}{v}\right) \quad (3.15)$$

If the spatial SEP amplitude variation is modeled as linearly decreasing with distance as in Equation 3.16, it is shown in that the velocity filtered output will be distorted.

$$s(x,t) = (mx + b)s\left(t - \frac{x}{v}\right) \quad (3.16)$$

The signal of Equation 3.16 may be decomposed into:

$$\begin{aligned} s(x,t) &= mxs\left(t - \frac{x}{v}\right) + bs\left(t - \frac{x}{v}\right) \\ &= y_1(x,t) + y_2(x,t) \end{aligned}$$

The second term is a scaled version of the signal in Equation 3.1 with the 2D Fourier Transform:

$$Y_2(k, \omega) = bS(\omega)\delta\left(k + \frac{\omega}{v}\right)$$

The 2D Fourier Transform of the first term is calculated as follows:

$$\begin{aligned} Y_1(k, \omega) &= \int_{-\infty}^{\infty} \int_{-\infty}^{\infty} mxs\left(t - \frac{x}{v}\right) e^{-j\omega t} e^{-jkx} \partial t \partial x \\ &= m \int_{-\infty}^{\infty} x e^{\frac{-j\omega x}{v}} \left[ \int_{-\infty}^{\infty} s(t) e^{-j\omega t} \partial t \right] e^{-jkx} \partial x \\ &= mS(\omega) \int_{-\infty}^{\infty} \left( x e^{\frac{-jx\omega}{v}} \right) e^{-jkx} \partial x \\ &= mS(\omega) G\left(k + \frac{\omega}{v}\right) \end{aligned}$$

where  $g(x) = x$ , and

$$\begin{aligned} G(k) &= \int_{-\infty}^{\infty} x e^{-jkx} \partial x & \therefore G\left(k + \frac{\omega}{v}\right) &= j \frac{\delta\left(k + \frac{\omega}{v}\right)}{k + \frac{\omega}{v}} & \therefore Y_1(k, \omega) &= mS(\omega) j \frac{\delta\left(k + \frac{\omega}{v}\right)}{k + \frac{\omega}{v}} \\ &= -j \frac{\partial}{\partial k} \int_{-\infty}^{\infty} e^{-jkx} \partial x & & & &= jms(\omega) \frac{\delta\left(k + \frac{\omega}{v}\right)}{k + \frac{\omega}{v}} \\ &= -j \frac{\partial}{\partial k} \delta(k) & & & & \\ &= j \frac{\delta(k)}{k} & & & & \end{aligned}$$

Combining these expressions:

$$\begin{aligned}
 S(k, \omega) &= Y_1(k, \omega) + Y_2(k, \omega) \\
 &= mS(\omega) \left( j \frac{\delta\left(k + \frac{\omega}{v}\right)}{k + \frac{\omega}{v}} \right) + bS(\omega) \delta\left(k + \frac{\omega}{v}\right) \\
 S(k, \omega) &= S(\omega) \delta\left(k + \frac{\omega}{v}\right) \left( b + j \frac{m}{\left(k + \frac{\omega}{v}\right)} \right) \tag{3.17}
 \end{aligned}$$

The filter has no knowledge of the spatial variation; it can only operate on velocity so it will also process the imaginary term which will appear in the filter output. It is seen in this case that the filtered output will be scaled by the factor  $b$ , and will contain an extra term which is a filtered version of the propagating signal that is scaled by the factor  $m$ , phase-shifted by  $90^\circ$ , and tapered off by the denominator as  $k$  and  $\omega$  increase. This distortion may corrupt the latency and amplitude information in the SEP.

The assumption of trace-to-trace amplitude consistency does not hold in surface recorded SEP measurements. There is spatial variation of SEP amplitude due to increasing depth under the skin surface. The variation of SEP amplitude with distance varies across different subjects and is likely to be nonlinear. The effects of this are difficult to represent mathematically or to predict. As an example, we have analyzed the effect of linearly decreasing SEP amplitude. The simplicity of this effect made it possible to predict the distortion due to filtering, but by no means is this to be regarded as an accurate model of spatial SEP amplitude variation. It is intended however to demonstrate that distortion will be introduced to the filter estimate if the SEP varies with distance.

## Chapter 4

### Simulation Study Using Sinc Pulses

#### 4.1 Simulation Study

In this section, an initial simulation study is performed using sinc pulses as test signals. In this way, the entire temporal frequency spectrum of interest is excited, spanning the approximate frequency range of the SEP. In addition, this allows us to examine the effects of the sampling rate, number of channels, trace-to-trace spatial variation of signal features, and distortion associated with velocity filtering.

The test signals under study are two sinc pulses exciting temporal frequencies up to 10.4 kHz equally, with one propagating at 50 m/s representing the SEP, and the other propagating very fast along the array representing the SA. The fast signal is located at the same temporal location in all traces, and its apparent velocity as seen by an array of sensors is instantaneously fast. The slow signal has a constant trace-to-trace latency and its apparent velocity is the ratio of the sensor spacing and the moveout or 50 m/s. The expressions for the fast and slow test signals at each spatial location are:

$$\begin{aligned}
 s_{1,n}(t) &= \text{sinc}(f_0 t) \\
 s_{2,n}(t) &= \text{sinc}(f_0 (t - n\tau)) \\
 s_n(t) &= s_{1,n}(t) + s_{2,n}(t) \quad n = 0, 1, 2, \dots, N_C - 1 \\
 \text{where } \text{sinc}(x) &= \frac{\sin(\pi x)}{(\pi x)}
 \end{aligned} \tag{4.1}$$

where  $s_n(t)$  is bandlimited to  $f_0 \approx 10.4$  kHz, and  $N_C = 21$  is the number of channels. In SEP measurements, only 11 channels will be available, limiting spatial frequency resolution, but

21 channels are used in this chapter for the purpose of better demonstrating the agreement of the velocity filtering theory with application under more simplified conditions. These simulated signals were sampled at 25 kHz, with a channel spacing of 5 mm or a spatial sampling rate of 200 cycles/m. Figure 4.1(a) shows the superposition of the 21 time-domain traces of the slow array signal,  $s_{2,n}(t)$ , and Figure 4.1(b) shows the  $k$ - $\omega$  magnitude spectrum of the array  $s_n(t) = s_{1,n}(t) + s_{2,n}(t)$ .

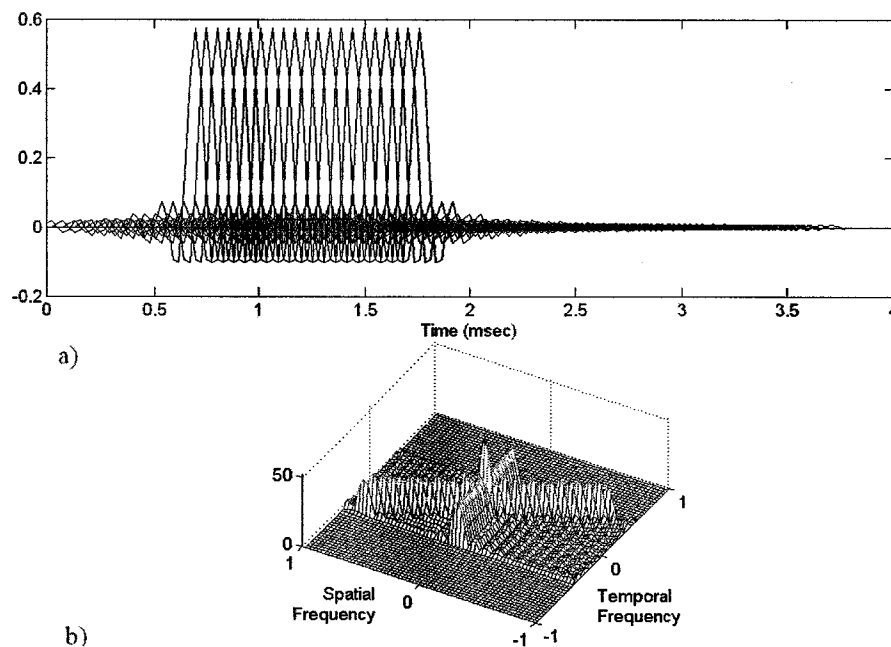


**Figure 4-1: (a) 21 simulated traces of  $s_{2,n}(t)$ , (b)  $k$ - $\omega$  magnitude spectrum of  $s_n(t)$**

The array data were velocity filtered using the fan filter FIR approximation described in section 3.3 whose magnitude and phase responses are shown in Figure 4.2(a) and (b), but the number of filter traces in this case is truncated to 41 rather than 21. This is because this simulation study uses 21 data traces for the purpose of verifying the agreement of applying the filter with what is expected from theory, whereas the real SEP measurements are limited

to 11 channels with 5 mm spacing and uses a 21-trace filter. The performance is also evaluated using different numbers of data channels including 11 channels as in the SEP array data. When using 21 data traces and filtering multiple times, using more than 41 filter traces does not offer an improvement in the SEP estimate. In general, when using  $N$  data traces, more than  $N$  filter traces will not offer an improved estimate of the slow signal estimate at the output center trace unless the same data are filtered multiple times in which case using more than  $2N-1$  filter channels will not offer improvements in the output center trace.

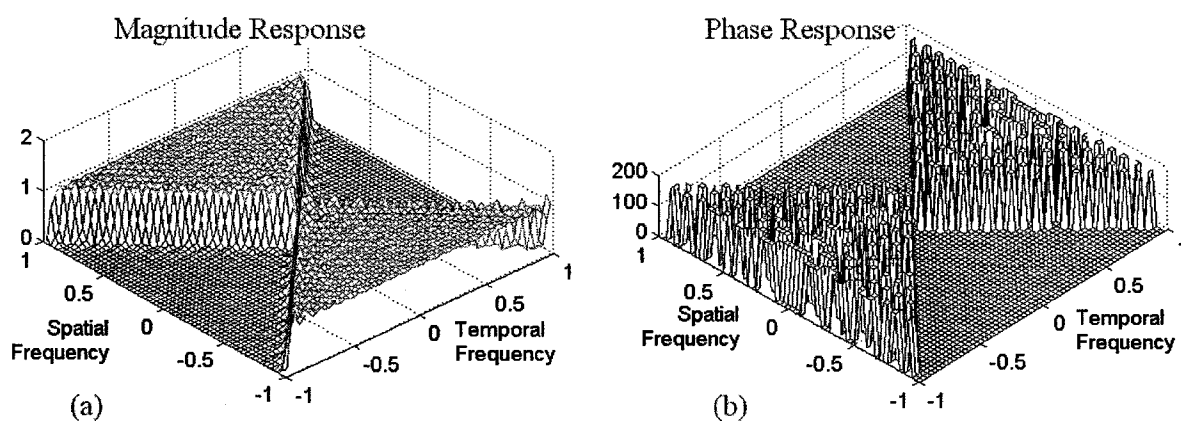


**Figure 4-2: (a) FIR fan filter  $k$ - $\omega$  magnitude response, (b) phase response**

After passing the data through the filter once, the output of the filter contains only the slow propagating component  $s_{2,n}(t)$  as expected, and the fast component  $s_{1,n}(t)$  has been attenuated by the filter. This is evident in the frequency domain as shown in Figure 4.3 where the  $k$ - $\omega$  magnitude spectra are compared for the input and output arrays.

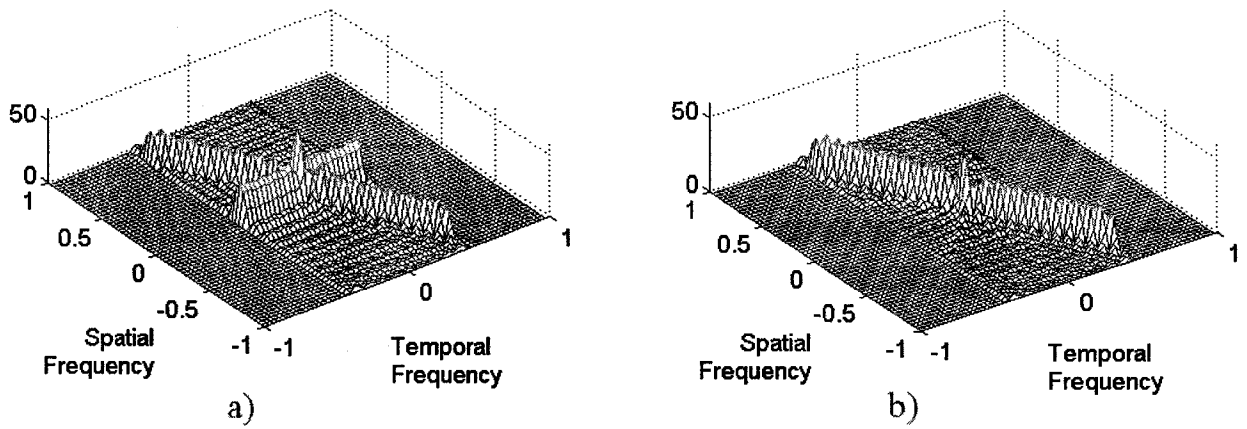
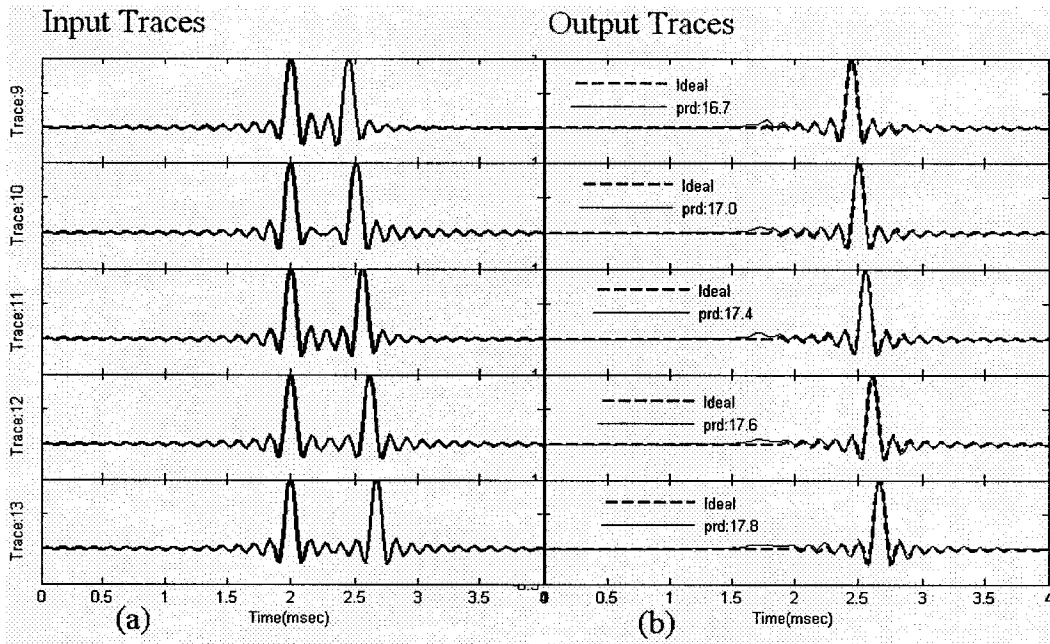


Figure 4-3:  $k$ - $\omega$  magnitude spectrum of (a) input, (b) output

In the time domain, accuracy of the center trace estimate is evaluated quantitatively for the center trace of the output using the percent residual difference (PRD) because the center trace naturally provides the best velocity filtered output as shown in Section 3.2. The PRD is a normalized measure of the variance of the error in the estimate expressed as a percentage in Equation 4.2.

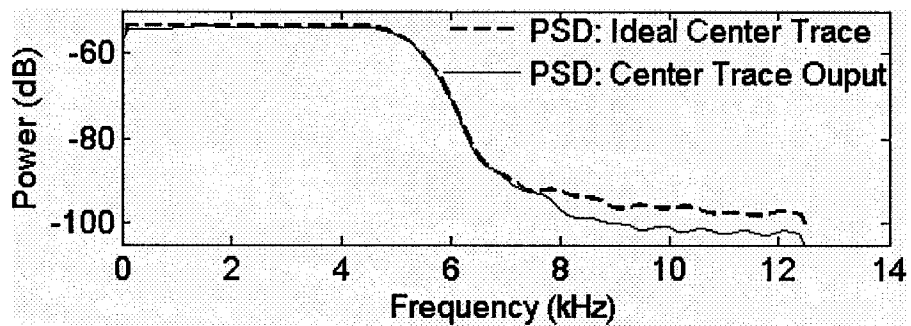
$$PRD = \sqrt{\frac{\sum_{n=1}^N \left( x_i(n) - \hat{x}_i(n) \right)^2}{\sum_{n=1}^N \left( x_i(n) - \bar{x}_i(n) \right)^2}} \times 100\% \quad (4.2)$$

Figure 4.4 shows the center 5 traces of the input and the output arrays. The output of interest is the center trace and corresponds to a velocity filtered version of the center trace of the input. The filtered SEP corresponds to the SEP located at the geometric center of the array. The attenuation of the fast component  $s_I(t)$  is seen in the  $x$ - $t$  domain in Figure 4.4(b). The PRD of the center trace filter estimate with respect to the ideal estimate is 17.4 %.



**Figure 4-4: Center 5 traces of signals from Equation 4.1, (a) input, (b) output**

Although the filter is a 2D system, the best velocity filtered output is the center trace. Other traces are discarded because only one spatially localized, 1D, velocity filtered SEP trace is required, so the system output is effectively the 1D center trace which is a SEP waveform as a function of time. The power spectral density (PSD) of the center trace is shown in Figure 4.5 along with that of the ideal center trace.



**Figure 4-5: Comparison of center trace output PSD with ideal**

As explained in Section 3.4.2, passband distortion occurs primarily in the low-frequency region of the filter. If more attenuation is desired, the data may be filtered multiple times, each time achieving more attenuation of components lying in the stopband, but at the expense of accumulating more possible distortion of components lying in the passband. A tradeoff must be made between the requirements of SA cancellation and of SEP distortion.

#### **4.2 Effect of Sampling Rate**

The simulation results of Section 4.1 with a PRD of 17.4% for the center trace were obtained with a sampling rate of 25 kHz. If the sampling rate is increased, the  $k$ - $\omega$  spectrum will be compressed in the temporal frequency dimension on a normalized frequency scale. This will tilt the spectrum of the slow signal further into the passband and less distortion should be expected because its  $k$ - $\omega$  spectrum is now further away from the passband edge; however, another consequence of increasing the sampling rate is that the attenuation of the fast signal component will be decreased as it moves closer to the passband edge. Further, the overall spectrum will be more localized around the low frequency range relative to the Nyquist frequency, and so an increase in low frequency distortion will be expected. Since the array data are limited by a finite number of channels, the number of filter traces is also limited by how many data channels it can make use of. As in any filter design problem, roll-off rate must be traded off for flatness of the passband and filter order. The direct impact of the sampling rate on filtering performance is difficult to predict because of the influence from the above factors. In this section, the overall sensitivity of the PRD performance for the center trace estimate is evaluated empirically over a range of sampling rates in order to provide

more insight into which distortion effects are more dominant in terms of achieving an estimate of the slow signal that is empirically optimal in the PRD sense.

The sampling rate was swept to examine its effect on the estimate slow signal. The following three cases were tested independently:

1. The slow signal was passed through the filter and the PRD due to distortion was measured shown in Figure 4.6(a) for sampling rates of 20 to 60 kHz.
2. The fast signal was passed through the filter and the residual power was measured in dB shown in Figure 4.6(b) for sampling rates of 20 to 60 kHz.
3. Both the slow and fast signals were passed through the filter and the PRD error due to both distortion and residual fast signal were measured shown in Figure 4.6, (c) for sampling rates of 20 to 60 kHz.

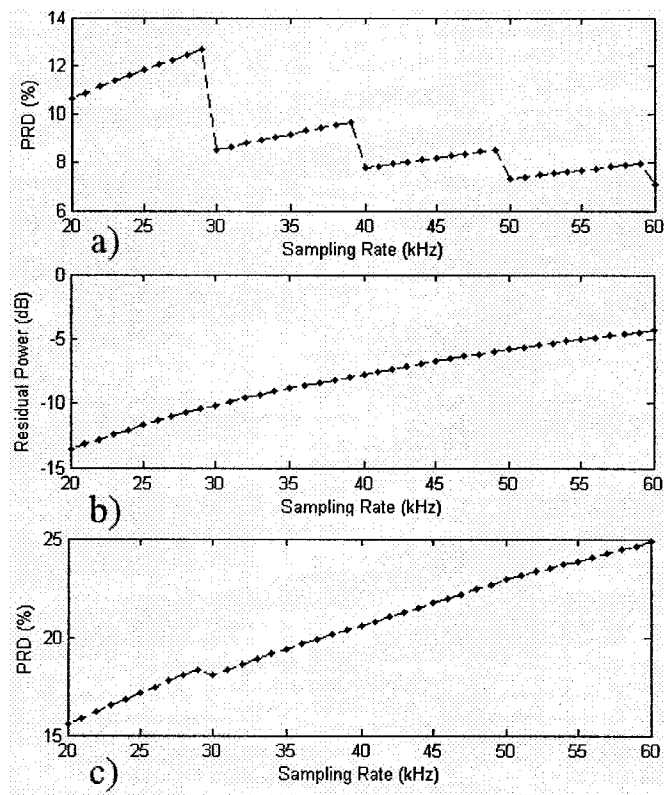


**Figure 4-6: Effect of sampling rate on filtering performance, (a) PRD measure of distortion when filtering slow signal, (b) residual power when filtering fast signal, (c) PRD measure of overall error when filtering fast + slow signals**

In Figure 4.6(a), the overall trend is that the distortion of the slow signal measured by the PRD decreases as the sampling rate is increased. The plot is also divided into local regions where the PRD increases. When the sampling rate increases the  $k-\omega$  spectrum accumulates more distortion as it moves into the low frequency range where more filter distortion occurs; however after the sampling rate increases to a point that the trace-to-trace moveout gains an integer number of samples, the PRD undergoes a large decrease because its distribution of frequency components in  $k-\omega$  space suddenly moves further away from the passband edge. Figure 4.6(b) confirms the fact that as the sampling rate increases, the filter cutoff velocity

increases. The closer that the high-velocity signal is to the filter cutoff velocity, the less it is attenuated by the filter. The residual power of the high velocity signal therefore increases with increasing sampling rate. In Figure 4.6(c), the overall PRD due to both passband distortion of the slow signal and residual fast signal increases with increasing sampling rate. The overall conclusion from these 3 plots is that as the sampling rate is increased, the effect of reduced stopband attenuation is the dominant source of error in the filter output because the overall PRD tends to increase. Therefore, the sampling rate should be chosen as small as possible, yet still large enough to not introduce too much passband distortion. Very high attenuation may be achieved, but this is of little use if the slow signal estimate is distorted. The goal of velocity filtering is to achieve an SEP estimate whose latency and amplitude are known with more certainty and confidence than that prior to filtering. This tradeoff between passband distortion and stopband attenuation is examined here for flat-spectrum signals and achieves a minimum PRD of ~15.5% when sampling at 20 kHz from Figure 4.6(c). Because the dominant source of error is due to the residual fast signal, the lowest possible sampling rate that satisfies the Nyquist theorem gives the best PRD. This is not the case when filtering the SA and SEP. In Section 6.1, a more appropriate sampling rate is chosen for simulated SA and SEP signals using the same method which does not necessarily coincide with this result because of the spectral characteristics of the SA and SEP.

One way of improving performance is to pass the data through the filter multiple times, each time achieving more attenuation of the high-velocity components lying close to the edge of the stopband. The costs associated are an increased computational load, and that components lying near the edge of the passband will accumulate more distortion. It is suggested that some

*a priori* knowledge or optimization be used to initially determine a sampling rate, and number of filter passes to get the best performance for a given application depending on the spectral content and propagation velocities involved with the signals of interest.

### **4.3 Effect of Number of Channels**

The number of channels of data available,  $N_C$ , and channel spacing,  $\Delta x$  are physical limitations imposed by the measurement setup. The SEP array measurements of interest in this study are located at the wrist location of the median nerve where the nerve bundle is close enough to the skin surface that the SEP may be detected with acceptable SNR using surface electrodes. The number of spatial channels in the array data is limited to about 11 to 15 channels when using 5 mm channel spacing. The limited number of channels imposes a degradation in the resolution of spatial frequency. This uncertainty in frequency leads to decreased filtering performance.

The minimum spacing between channels in the array data that can be achieved with reasonable accuracy using bipolar electrodes in our measurement setup is  $\approx 5$  mm. A result of this and the physical electrode sizes places an upper bound on the spatial Nyquist frequency or on the minimum wavelength that can be unambiguously represented in the SEP measurements.

To examine in more detail the effects of varying the number of channels and the channel spacing, these two parameters were swept and the PRD was used as a measure of the performance. The number of data channels was swept from 3 to 51 in steps of 2. This was done using the test signals of Equation 4.1, with a sampling rate of 25 kHz, channel spacing

of 5 mm, and 101 filter channels. Figure 4-7 shows the curve of the PRD versus number of data channels.

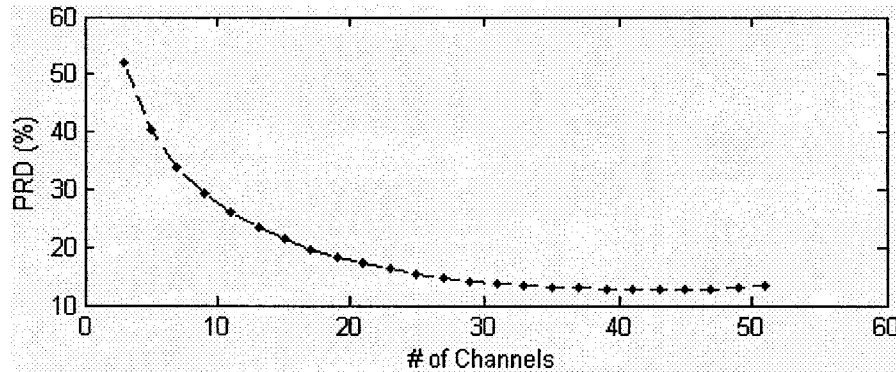


**Figure 4-7: PRD of center trace filter output for different number of data channels**

The PRD error appears to have inversely proportional relationship to the number of data channels. Using 21 channels in Section 4.1 achieves a PRD of ~17.4%. Using more than 40 channels reduces the PRD to nearly 10%. In real measurements, using 5 mm spacing on the median nerve at the wrist, only 11 to 15 channels are typically available because outside of this range the nerve is too deep under the skin surface for a large enough SEP to be measured from the skin surface. Although spatial frequency resolution may improve with more channels, our objective is to determine whether the SA reduction using 11 available SEP channels is significant enough to justify the use of a velocity filter for stimulus artifact reduction. Using the simulated sinc pulses, Figure 4-8 indicates that the PRD performance using 11 channels and 5 mm spacing is roughly 27%. While the velocity filtered estimate of the slow signal is quite accurate, spatial SEP variations have not yet been considered in these simulations which are another source of distortion to the SEP estimate. Figure 4-8 shows the PRD curve versus channel spacing, or spatial sampling rate.

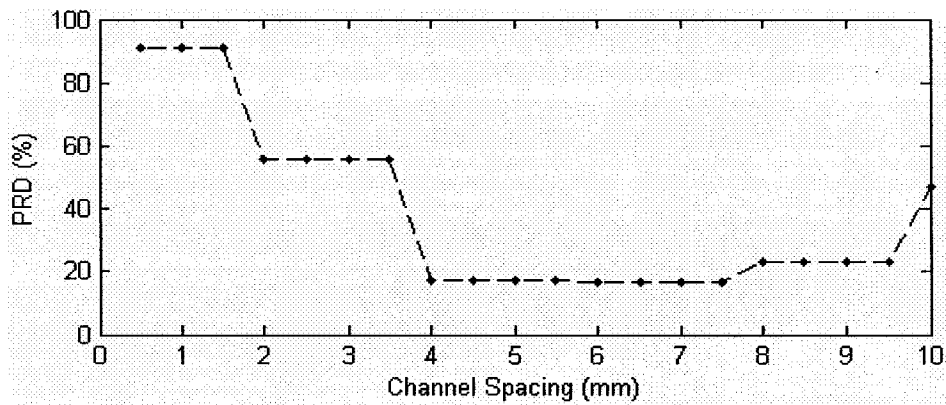


**Figure 4-8: PRD of center trace filter output for different channel spacing**

When the channel spacing is small (1 mm), the spatial Nyquist frequency is larger, compressing the spectrum in the  $k$  dimension, and tilting the slow signal closer to the passband edge where more distortion occurs as in Figure 3-5. As the spacing is increased, the PRD improves until the spacing becomes too large and the PRD begins to increase due to spatial aliasing or folding in the  $k$  dimension. Considering the median nerve's superficial range and the electrode sizes, a spacing of 5 mm is a practical choice in terms of PRD performance of the center trace SEP.

#### **4.4 Effect of SEP Spatial Amplitude Variation**

The assumption that the propagating temporal signal does not change with distance along the array axis has been assumed in the previous simulations. This was expressed in Section 3.1 as:

$$\begin{aligned}
s(x,t) &= s\left(t - \frac{x}{v}\right) \\
S(k,\omega) &= S(\omega)\delta\left(k + \frac{\omega}{v}\right)
\end{aligned}
\tag{4.3}$$

Due to the variable fiber depth under the skin surface along the nerve axis, the SEP experiences attenuation that increases with axial distance, resulting from the tissue filtering effect [25].

Although the velocity filter can produce an accurate estimate of the slow signal's shape, its amplitude and phase may be distorted by the filter because amplitude is a feature that is not constant with distance in the array measurements.

The signal features that will mainly contribute to distortion of the filter estimate when varying with distance are:

1) Spatial variation of amplitude due to attenuation. If the amplitude varies across traces, then amplitude information will not be consistently represented in the center-trace output of the filter as shown in section 3.4.3. This is confirmed by running the same simulation as in Section 4.1, but reducing the peak amplitude of each channel to 90% of that from the previous channel. This test obtained a PRD of 46.9% as opposed to the constant amplitude case where the PRD was 17.4%.

2) Inconsistency in trace-to-trace delay due to imperfect sampling times or electrode locations in the array. This situation will reflect a time-varying propagation velocity, and rather than a straight line in  $k$ - $\omega$  space as in Figure 3.2, the spectrum will be distributed around the straight line, with some variance around it. The result is that different frequency

components in the array may experience different gains from the filter and distort the overall center trace estimate. This is confirmed by running the same simulation as in Section 4.1 with 21 traces, but with a trace-to-trace moveout of 1 sample for 7 channels, 2 samples for the next 7, and 3 samples for the remaining 7. This test obtained a PRD of 55.6% as opposed to the constant velocity case where the PRD was 17.4%.

#### **4.5 Loss of Low Frequency Information**

As described in Section 3.4.2, a general result of realizing fan filters is that low frequency information is distorted or lost. One way to look at this is by examining the ideal fan response in Figure 3.5. An ideal 1D low-pass filter has a discontinuity or an instantaneous jump from 1 to 0 in the magnitude of the frequency response at the cut-off frequency. This type of sharp and sudden change has a very large derivative and an infinitely large filter order is required to perfectly model this shape, thus temporal windowing, finite roll-off, and ringing occur in practical filter realizations. In the 2D fan filter response, two of such discontinuities approach each other with decreasing frequency and converge at the origin. Therefore the ringing and finite roll-off from the passband edge in each frequency dimension combines with that of the other frequency dimension more and more as frequency decreases and the two edges approach each other.

Several techniques have been proposed in the literature to reduce or remove this effect [21], [22]. Fortunately, the SEP is a bandpass signal and contains little information below 1 kHz [3]. Using sinc pulses exciting the full spectrum equally, we can measure the extent to which low frequency information is attenuated. The plot in Figure 4-9 shows a comparison of the

PSD of the center trace estimate and the ideal estimate of the filter for the same simulation in Section 4-1; however in this case the data were passed through the filter 5 times, to exaggerate the effect of low-frequency distortion.

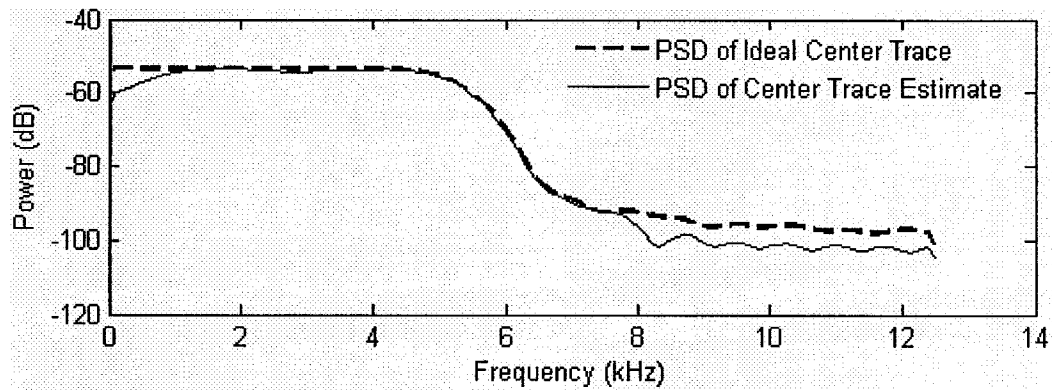


**Figure 4-9: Power spectral density of center trace filter output**

The observation is that most distortion becomes significant at frequencies below 1 kHz when using 5 mm spacing and a 25 kHz sampling rate. This is encouraging because the SEP has a bandwidth of ~ 1-3 kHz.

## Chapter 5

### Simulation Study Using Synthetic SEP Measurements

In this chapter, to evaluate the method of velocity filtering for SA reduction in surface recorded SEP measurements, a simulated array of SEP and SA was used. This way, random noise can be eliminated and parameters can be controlled such as the relative amplitudes of the SEP and SA, number of channels, SEP latency, and spatial SEP variations. To simulate the SEP array, a linear dynamic model was used to approximate single-fiber action potentials (SFAP) based on [25]. To simulate the SA array, a linear circuit model was used to approximate the current-voltage dynamics producing the SA based on [13].

#### 5.1 Simulated SEP Array

A single bipolar surface-recorded SEP measurement was approximated by a single-fiber action potential (SFAP), and the consecutive array traces evolving with axial distance are generated by increasing the distance from the innervation zone to the recording site in intervals of 5 mm. The trace-to-trace SEP latency with axial distance is consistent with the SEP conduction velocity and channel spacing which are assumed to be 50 m/s and 5 mm respectively in this study. To approximate bipolar measurements which are tri-phasic waveforms, a single simulated SEP trace is composed of the difference between the potential located at a position  $x + d$  and position  $x$ , where  $x + d/2$  is the distance from innervation zone to the recording site, and  $d$  is the inter-electrode distance which is 20 mm for the recording electrodes in our measurement setup.

In [25], a static model was used to approximate the spatially localized action-potential (AP) on the nerve in response to a square current stimulus pulse. This potential is a function of the fiber depth, the stimulus intensity, and stimulus duration. A linear dynamic system that models the two-port input-output voltage dynamics (tissue filter) is then used to compute the potential after propagation to a location down the fiber and located above the nerve on the skin surface. This potential is a function of the distance from innervation zone to recording site, inter-electrode distance, fiber depth, and conduction velocity. The overall system is represented by the diagram of Figure 5-1.

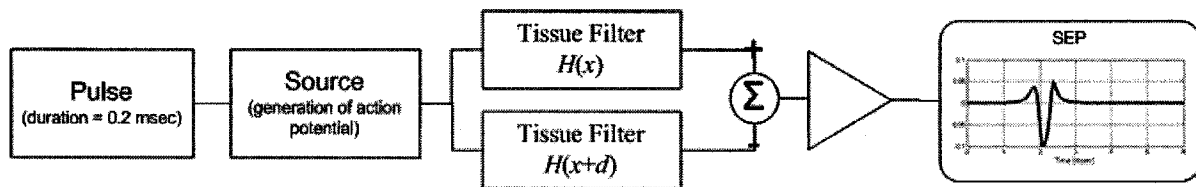


**Figure 5-1:Block diagram illustrating synthetic SEP measurements**

Although a surface recorded SEP is composed of a temporal distribution of contributions from many individual axons with a distribution of conduction velocities, this model uses a single conduction velocity of a single fiber for simplicity. Random noise and spatial SEP variations other than latency are not considered. To create the array data, this was repeated for 11 channels of SEP signals, with the distance from innervation zone to recording site increasing by intervals of 5 mm for each consecutive trace representing the channel spacing. The parameters used in these simulations are given in Table 5-1. The length of the single fiber is also assumed to be infinite. The model was generated and computations performed using a simulation program in Matlab that was supplied by the author of [25].

Parameter	Value
Sampling Rate	25.6 kHz
Distance from Innervation Zone to Midpoint of First Electrodes in Array	150 mm
Source Duration	0.2 ms
Depth of Fiber	5 mm
Conduction Velocity	50 m/s
Fiber Termination	Unterminated <sup>1</sup>

**Table 5-1: Simulation parameters used to generate SEP waveforms**

The only spatial variation in the signals considered here is the constant trace-to-trace SEP latency computed from its propagation velocity. In Figure 5-2, the 11 simulated SEP traces are shown.

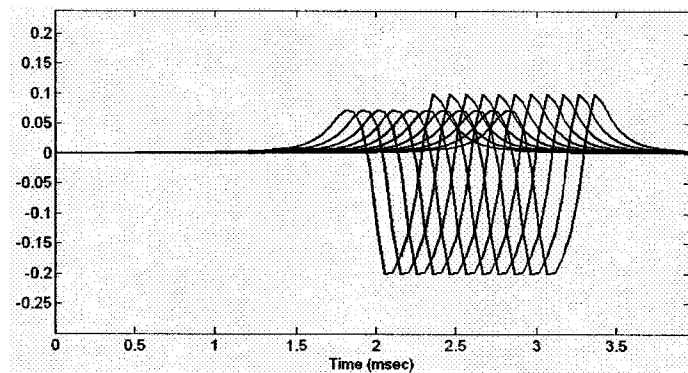


**Figure 5-2: Synthesized 11-channel array of surface-recorded SEP's**

---

<sup>1</sup> Infinite fiber length

## 5.2 Simulated Stimulus Artifact

A two-port linear circuit was used to model the current-voltage dynamics between the stimulus current pulse and the recording electrodes pair. This system maps the rectangular current pulse to an SA waveform that resembles the one that appears in real measurements and is based on the work in modeling of the stimulus artifact in [13]. The simulation was carried out in the time domain using a transient sweep over a 10 ms time period using a time-step of  $1/256000$  which was later re-sampled to 25.6 kHz so it could be temporally added to each simulated SEP trace. This was done using the commercial circuit simulator Agilent ADS version 2003(a) with the schematic shown in Figure 5.3. The components included in the model are explained below. The component values have been roughly chosen within a reasonable range for creating a synthetic stimulus artifact, but are not to be mistaken as being an accurate representation of realistic values.

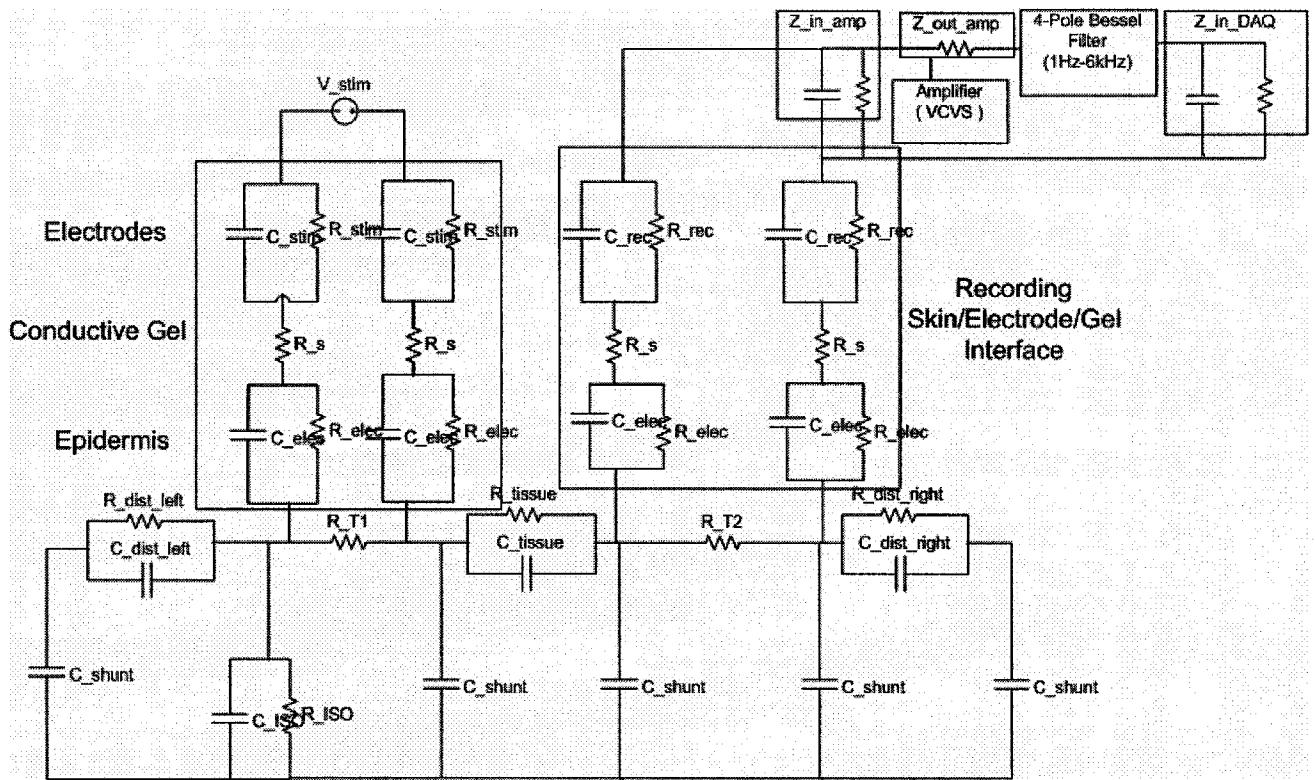


Figure 5-3: Circuit schematic of SA generation mechanism model in Agilent ADS

1) Stimulating and Recording Electrodes: Although the stimulating and recording electrodes used are different, for these purposes, their impedances are assumed to be the same. They are modeled as a parallel RC network so they behave as low-pass filters. The values are chosen based on [14].

$$R_{Stim} = R_{Rec} = 50 \text{ k}\Omega$$

$$C_{Stim} = C_{Rec} = 10 \text{ nF}$$

2) Series resistance between electrodes and skin: This value represents an ohmic drop across the electrolytic gel based on [14].

$$R_s = 50 \text{ }\Omega$$

3) Epidermis layers: These are represented by a parallel RC network. The resistance and capacitance are small and thus are expected to have a small effect compared to the electrode impedances. The values are based on [8].

$$R_{ELEC} = 100 \Omega$$

$$C_{ELEC} = 0.1 \text{ nF}$$

4) Tissue impedances between bipolar electrode pairs: These depend on the separation between the 2 electrodes used in bipolar measurements, which are 20 mm for recording electrodes and 30 mm for stimulating electrodes in our measurement setup. The values are based on [14].

$$R_{T1} = 72 \Omega$$

$$R_{T2} = 72 \Omega$$

5) Isolation impedances: These are located between the stimulator and ground, and between recording amplifier and ground and are modeled as a parallel RC network with a very large resistor and a very small capacitor. A body reference is taken as the zero potential reference for ground. This removes DC components from the measurement system and provides safety to the patient from possible electrical power surges in the instrumentation systems connected to the wall supply [13]. The values chosen are based on [13].

$$R_{ISO} = 1.976 \text{ G}\Omega$$

$$C_{ISO} = 16.3 \text{ pF}$$

6) Distributed impedance of the body tissues outside the range of interest: This is modeled by parallel RC networks that are placed to the left of the stimulation site, and to the right of the

recording site and are much greater than those than tissue impedances inside the region between the stimulation and recording site. They roughly model the fact that some SA energy escapes to the ground through other paths in the body. These are not to be mistaken as accurate values and they vary widely across subjects, however the role that they play here is that they are finite, but much larger than the tissue parameters between stimulus and recording sites because there is much more tissue outside of this region.

$$R_{Distr\_left} = 5 \text{ k}\Omega$$

$$C_{Distr\_left} = 100 \text{ }\mu\text{F}$$

$$R_{Distr\_right} = 5 \text{ k}\Omega$$

$$C_{Distr\_right} = 100 \text{ }\mu\text{F}$$

7) Distributed impedance of the body tissues outside the range of interest: This is modeled by a parallel RC network, representing the impedance of the tissues between the stimulus and recording sites. The values are based on [14].

$$R_{Tissue} = 500 \text{ }\Omega$$

$$C_{Tissue} = 1.5 \text{ }\mu\text{F}$$

9) Stimulation current: This is modeled as an ideal current source. The pulse duration was set to 0.2 ms as in the measurement setup used. The rise and fall-times were set to 0.05 msec. The rise and fall times are actually on the order of microseconds, but 0.05 ms was used to relax the computational demands of numerical integration by using lower frequency content (slower rise/fall times). Faster rise and fall times make the solution of the system time-consuming and have little importance for our purpose of synthesizing a rough model of the SA. The amplitude was set to 5 mA, changing it only scales the input and output because the

model is linear. In reality, the system is nonlinear and the SA shape is a nonlinear function of stimulation strength [5], [6], [16].

10) Recording amplifier: The amplifier used in our measurement setup is a Grass 15A54 bio-amplifier. From the data sheets, the input impedance was  $20\text{ M}\Omega$  in parallel with  $35\text{ pF}$ , the output impedance was  $300\ \Omega$ . The amplifier includes an integrated 4-pole analog Bessel bandpass filter with a bandwidth from  $1\text{ Hz}$  to  $6\text{ kHz}$  which is also included in this model. These parameters are constant in the frequency range of interest. The amplifier and bandpass filter were included in the model by using an ideal voltage-controlled voltage-source (VCVS) with the specified input and output impedances, and a 4-pole, unity gain, Bessel bandpass filter with a bandwidth from  $1\text{ Hz}$  to  $6\text{ kHz}$  from the Agilent ADS component library.

11) Data Acquisition Board: Sample and hold and quantization were performed in our measurement setup using a National Instruments PCI-6071E data acquisition board (DAQ). From the data sheets, its input impedance was  $100\text{ G}\Omega$  in parallel with  $100\text{ pF}$ . This was also included in the model.

After running the simulation, the plot of the SA in Figure 5-4 was obtained. The backwards Euler method was used with the MNA matrix formulation and a fixed time-step of  $1/256000$  seconds.

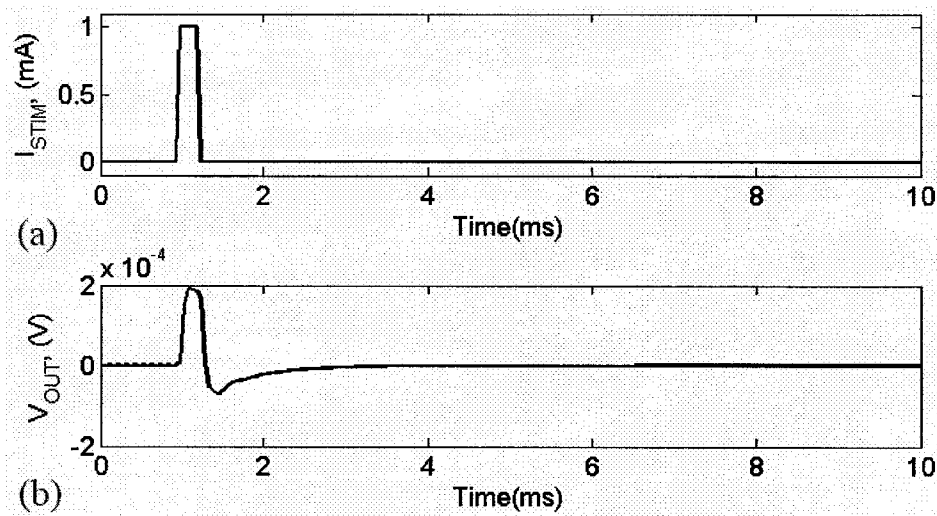


**Figure 5-4: Simulation of SA generation mechanism, (a) input current, (b) output voltage**

After sweeping various input parameters over large ranges, it was found that the only variables that had a significant impact on the output waveform were the stimulation electrode impedance, and the tissue impedance between recording electrodes,  $R_{Sim}$ ,  $C_{Sim}$ , and  $R_{T2}$ . Imbalance of recording electrode impedances was also found to significantly change the SA waveform. The simulation model produces very similar SA waveforms to the ones appearing in real measurements. For stimulus artifact array data synthesis, this SA waveform was copied and added to each of the simulated SEP traces, with no delay in order to simulate its very large apparent velocity. Figure 5-5 shows the superimposed 11 channels of the array of simulated SA + SEP measurements. In this image the relative amplitudes of the SEP and SA are not to scale, the simulated SEP is made larger for visual representation. In the data used for velocity filtering, the peak amplitude of the SEP is 20 times smaller than that of the SA.

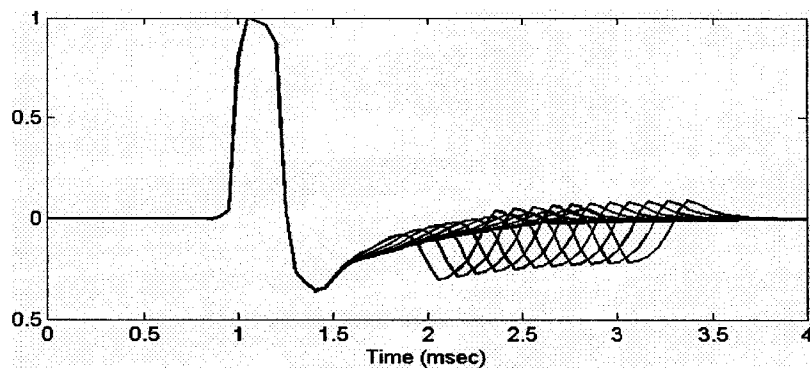


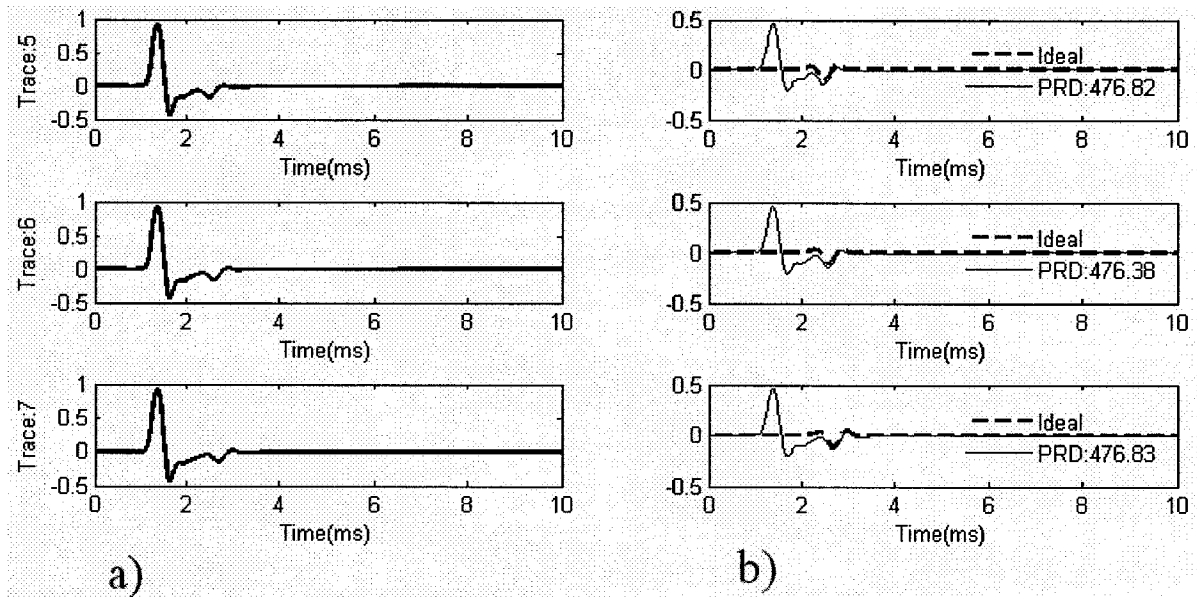
**Figure 5-5: Simulated SEP measurements with SA corruption (SEP amplitudes are scaled up)**

### 5.3 Simulation Results

The SEP and SA array data that were synthesized by simulation in Section 5.1 and 5.2 were used to test the performance of the fan filter for reduction of the stimulus artifact in SEP measurements. The filter used was the one described in Section 3.3 with a filter size of  $21 \times 101$ . The simulated data contains 11 channels with 5 mm spacing, 50 m/s conduction velocity, has a 20 times ratio of SA to SEP peak amplitudes, and contains no spatial SEP variations. The sampling rate was swept as in Section 4.2 to determine a sampling rate that gives the minimum PRD and was selected as 66 kHz.

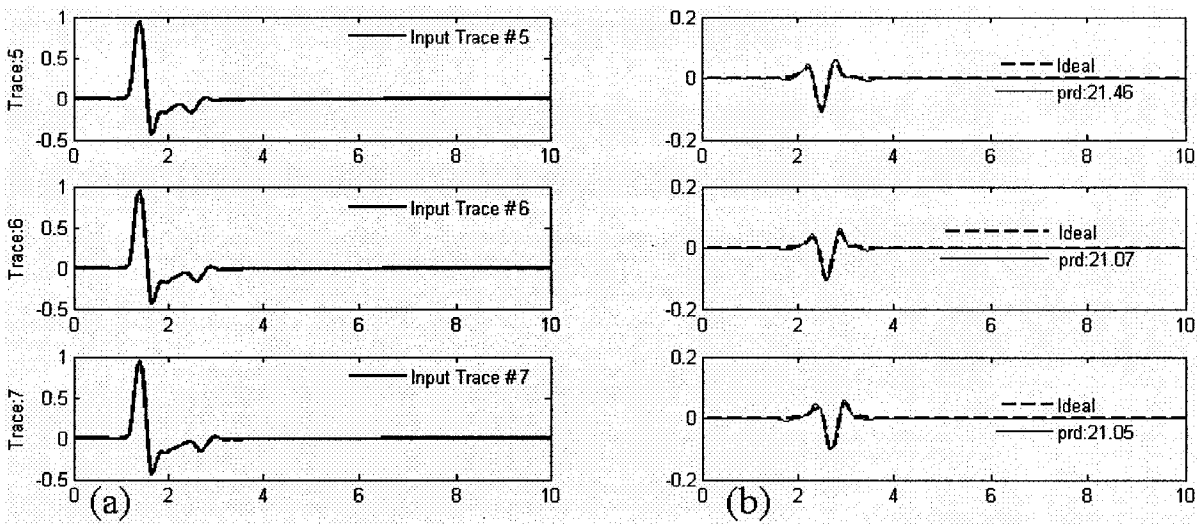
After filtering the array data once, the SA is attenuated and there is a gain in SNR, but the SEP is still significantly distorted by the SA. In order to achieve much larger levels of SA attenuation, the data must be filtered multiple times, each time achieving greater attenuation, at the expense of accumulating passband distortion. Too many filter passes may introduce too much distortion to the SEP estimate; however too few passes will not sufficiently attenuate the SA.

Figure 5-6 shows the center 3 center traces of the input and output arrays after filtering the array data once. In this case, the SA has been attenuated, but it still considerably distorts the SEP.



**Figure 5-6: Center input and output traces for one filter pass, (a) input, (b) output**

The PRD of the center trace estimate after filtering one time has been reduced from  $PRD_{ALL} = 887.40\%$  to  $476.40\%$  over the entire waveform and from  $PRD_{SEP} = 235.22\%$  to  $120.21\%$  during the time period containing the SEP. After filtering 200 times, the  $PRD_{ALL}$  reduces to  $21.07\%$  and  $PRD_{SEP}$  reduces to  $17.94\%$ . The 3 center traces of the input and output are shown in Figure 5-7 after filtering 200 times. Note that the peak amplitude of the SA was reduced by a factor of 2.04 after filtering once and by a factor of 1020.8 after filtering 200 times.



**Figure 5-7: Center input and output traces after 200 filter pass, (a) input, (b) output**

The SA has now been almost entirely attenuated. This is also evident in the  $k-\omega$  domain shown in Figure 5-8.

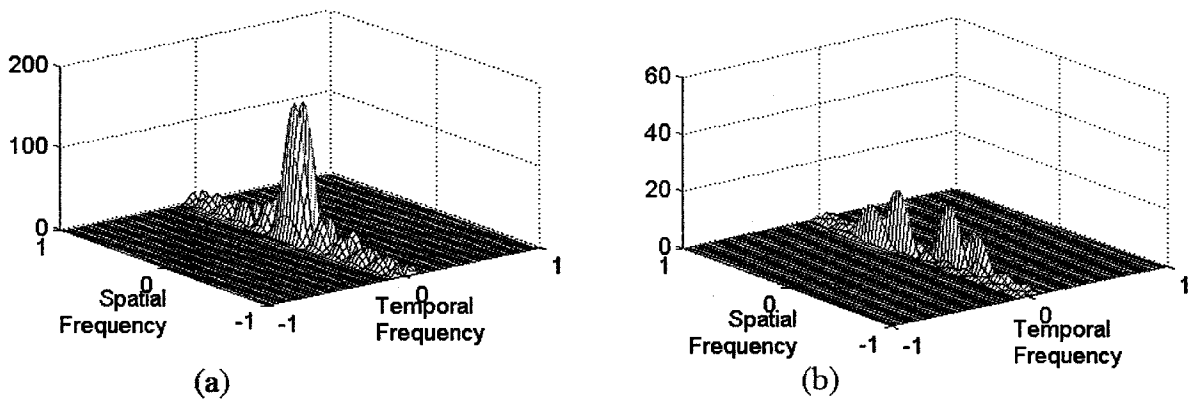


**Figure 5-8: Input and output  $k-\omega$  magnitude spectra after 200 filter pass, (a) input, (b) output**

From the one-dimensional PSD of the center trace estimate, the frequency content of the filter output matches with that of the ideal estimate, except for the small loss of low frequency content. Fortunately, the SEP contains little energy below 1 kHz and this effect is not as significant as in the case of the sinc pulses of chapter 4.

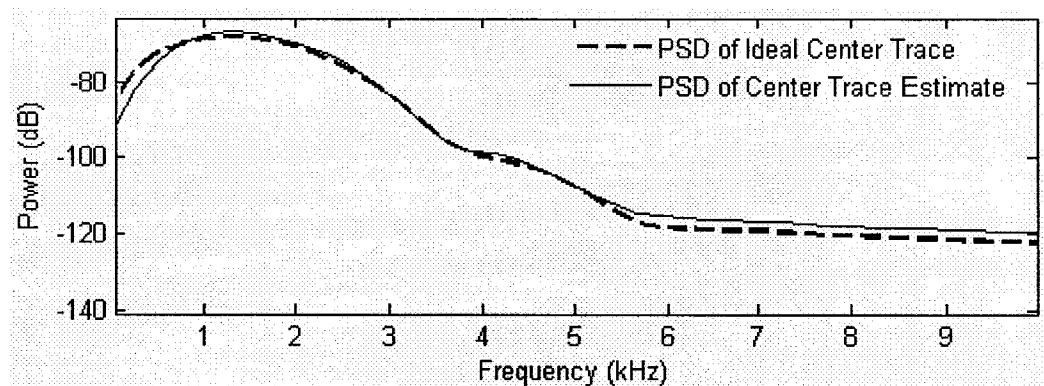


**Figure 5-9: PSD of center trace output compared to ideal after 200 filter passes**

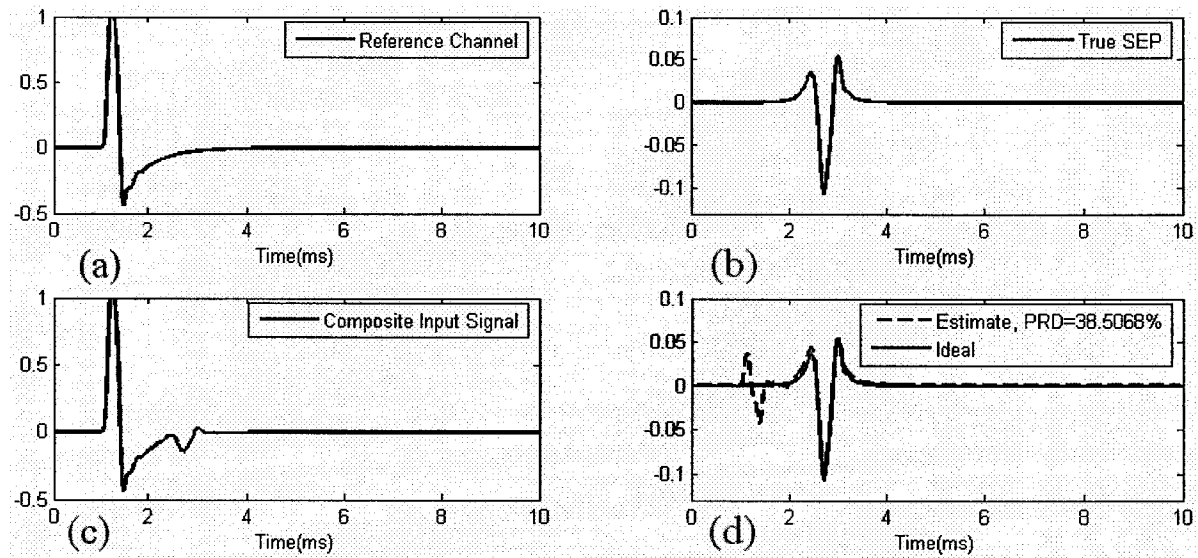
The simulated SA and SEP signals have been used to validate the fan filter as a means of velocity filtering for reduction of the stimulus artifact under ideal conditions and using 11 channels with 5 mm spacing. The performance was evaluated in terms of the PRD since the ideal filter output was known in advance. In Chapter 6, this method is applied to real 11-channel arrays of SEP measurements from 10 subjects.

#### **5.4 Comparison with Nonlinear ANC - Segmented Training**

A nonlinear ANC scheme was described in Chapter 2 for stimulus artifact reduction. This method used an ANN to learn the relationship between a SEP measurement and an off-nerve reference channel not containing a SEP, but containing an SA that is correlated with the one in the primary channel. These data were segmented into 2 partitions, the first being the time period before the occurrence of the SEP and was used to train the ANN. The second segment would extrapolate, or generalize this relationship over the remaining time period to estimate the shape of the SA waveform and subtract it from the measurement. Refer to Section 2.3.1 for a detailed description of the method. These two methods are compared against each other

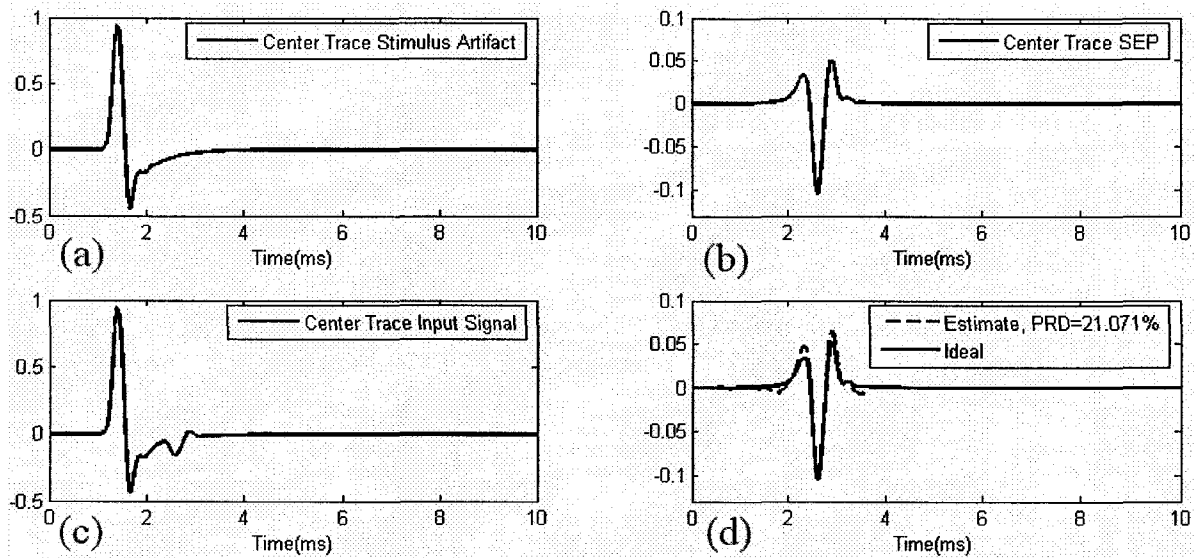
using the synthetic data from Sections 5.1 and 5.2. In both cases, the conduction velocity of the SEP was 50 m/sec and the SA propagation velocity was infinite.

Figure 5-10 shows the results of nonlinear ANC with segmented training using one off-nerve reference channel and a primary SA+SEP channel. This reference channel was synthesized by passing the SA through a 6<sup>th</sup> order Butterworth low-pass filter with a bandwidth of 425 kHz so that it is correlated with the SA in the reference channel. The ANN in this case used a 3 layer MLP structure with 2 input delays and 10 hidden neurons. Different ANN structures were attempted and this one yielded acceptable empirical results although a full exhaustive search was not the focus of the thesis. This method is very sensitive to the user's choice of  $t_0$ , the time point just before the occurrence of the SEP where the training and predicting data are segmented from the one original data set. This must be chosen manually by trial and error for each new measurement because both conduction velocity and the SA vary between subjects. The best result shown here was obtained when  $t_0$  was selected to be 21% of the total 10 ms time interval. This method is also sensitive to the sampling rate. Since the adaptive element is nonlinear, even when the training data presented to the ANN is sampled above the Nyquist rate, when used for prediction the ANN may introduce harmonics into the output that may contain higher frequencies. Consequently, trial and error must be used before discovering that good performance is achieved after up-sampling the data from 66 kHz to 100 kHz. Training was stopped when the gradient of the least squared norm of the training error (L2 error) with respect to the weights stopped changing.



**Figure 5-10: Results of SEP estimate using segmented nonlinear ANC, (a) reference channel, (b) ideal SEP estimate, (c) primary channel, (d) comparison of SEP estimate and ideal**

Figure 5-11 shows the same SEP estimate after filtering 200 times using the same  $21 \times 101$  fan filter from Section 5.3 with 11 channels of data sampled at 66 kHz with 5 mm spacing. Note that the same data were used in both cases for the ANC primary input and the velocity filter center trace, however due to linear interpolation when this signal is up-sampled in Matlab, the center trace SA and SEP appear slightly different between Figure 5-10 and Figure 5-11.



**Figure 5-11: Results of SEP estimate using 11-channel velocity filter, (a) center trace SA, (b) center trace SEP, (c) center trace input, (d) comparison of center trace estimate and ideal**

For the velocity filtered estimate,  $PRD_{ALL} = 21.07\%$  and  $PRD_{SEP} = 17.94\%$  after filtering 200 times. For the ANC method,  $PRD_{ALL} = 38.51\%$  and  $PRD_{SEP} = 16.90\%$ . Using this simulated data, the PRD performance is better overall when using the velocity filter due to better SA cancellation; however the PRD within the region containing the SEP is lower for the nonlinear ANC method because it introduces less SEP distortion. Note that the SEP distortion due to velocity filtering would normally be even greater when spatial SEP variation is included. It should also be noted that different ANN structures, different values of  $t_0$ , and different sampling rates were attempted by trial and error to obtain this result. In the general case, the performance of the nonlinear ANC estimator is not guaranteed to be accurate unless these parameters are exhaustively selected by trial and error.

To obtain the results for the ANC method, different ways of segmenting the data, different sampling rates, and different ANN structures were exhausted by trial and error before

obtaining the estimate above with the lowest PRD. Table 5-2 quantitatively compares these 2 methods using the following 5 metrics:

$q_1$ : PRD over the entire waveform (smaller  $q_1$  indicates a closer estimate)

$q_2$ : PRD over the portion of the waveform containing the SEP (smaller  $q_2$  less SEP distortion)

$\rho_1$ : the ratio of the peak value in the primary channel to that in the output. The primary channel has been defined in the case of ANC schemes, but for velocity filtering, the primary channel is taken to be the center trace of the 11-channel SEP array measurements. This computation is done during the time period before the occurrence of the SEP. A large value indicates higher attenuation of the SA peak before the occurrence of the SEP.

$$\rho_1 = \frac{x_{pk}}{sep_{pk}} \quad (6.1)$$

$\rho_2$ : the ratio of the standard deviation in the primary channel to that in the output. The primary channel is also taken to be the center trace of the 11-channel SEP array measurements. This computation is also done during the time period before the occurrence of the SEP. A higher value indicates better reduction of overall SA energy before the occurrence of the SEP.

$$\rho_2 = \frac{\sigma_x}{\sigma_{sep}} \quad (6.2)$$

$\rho_3$ : the ratio of the mean-squared value (MSV) in the output to the primary channel. The primary channel is also taken to be the center trace of the 11-channel SEP array measurements, but this computation is done during the time period after the occurrence of the

SEP. This helps to assess how much SA tail has been attenuated using the assumption that most of the MSV is due to the SA and not to the SEP. It should be noted however, that it can not distinguish how much of the MSV is due to the SA and not to the SEP. Because the SEP is much smaller than the SEP, a smaller value generally indicates better reduction of the SA tail.

$$\rho_3 = \frac{MSV_{sep}}{MSV_x} \quad (6.3)$$

It important to note that the first two metrics ( $q_1$  and  $q_2$ ) enable a deterministic comparison of the SEP estimate with the ideal estimate, but the last 3 metrics ( $\rho_1$  through  $\rho_3$ ), which are from [reference], make no assumption about the ideal estimate. This is because in chapter 6 when the velocity filter and the nonlinear ANC method are objectively compared using real data where the ideal SEP estimate is unknown, only the  $\rho$  metrics can convey some degree of determinism in accuracy of the estimate. This is because they are computed from signal features that are well defined for the SA and SEP, namely the peak amplitude, standard deviation, and mean-squared value. Although the ideal SEP is known in the simulated data, these last 3 metrics are still computed here to enable comparison to the results from the real data in chapter 6.

	$q_1$	$q_2$	$\rho_1$	$\rho_2$	$\rho_3$
<b>11-Channel Velocity Filter</b>	21.07%	17.94%	1020.80	517.4033	1.4641e-006
<b>ANC (Segmented Training)</b>	38.51%	16.90%	19.9250	28.0008	0.0191

**Table 5-2: Summary of performance indices for velocity filter and nonlinear ANC (grey box used to indicate which method was better according to the given metric)**

Using simulated data, and these 5 performance metrics, the 11-channel velocity filter is found to outperform the nonlinear ANC method in all cases except for  $q_2$  when considering a 10 ms time interval containing the SEP and SA. The  $q_1$  measure indicates that the overall velocity filtered SEP estimate is closer to the ideal estimate than the ANC estimate because it better attenuates the SA. However the  $q_2$  measure shows that less distortion is suffered in the ANC case. The lower  $q_2$  shows that the ANC method outperforms the velocity filter inside the region containing the SEP by 1%. This is because it introduces slightly less SEP distortion in this case than the velocity filter. The primary cause of the filter's distortion is spatial variation in SEP amplitude as explained in Chapter 4.

The  $\rho_1$  performance indicates that the velocity filter attenuates the SA peak 51.2 times more than the ANC method in this case. Ideally, the SEP estimate should be zero everywhere outside the time containing the SEP. The  $\rho_2$  performance indicates during this time, the velocity filter reduces the standard deviation 18.5 times more than the ANC method does in this case. The  $\rho_1$  performance shows that that the velocity filter achieves better “flattening” of the SA tail. This is the most important  $\rho$  measure because it is the SA tail that overlaps the SEP in time and not the initial large spike portion of the SA.

When interpreting these results, it should also be noted that the ANC system parameters were carefully selected by trial and error to yield the lowest  $q_1$ , the ANC reference channel was a low-pass filtered version of the SA in the primary, no spatial variation of the propagating SEP was assumed, and the data used for ANC were interpolated from 66 to 100 kHz. It is

also important to note that for the velocity filter, the results may be improved by using different filter design methods and using more data channels, and the ANC results could be made better if the SA in the reference channel was more correlated with that in the primary channel.

The main observation is that the velocity filter better attenuates the SA, but also introduces more distortion to the SEP because the data were filtered 200 times. Because this distortion is deterministic, it can be accounted for by measuring the exact distortion of the filter which is a deterministic, LTI system with a static architecture. This is a topic of future research. Using velocity filters with real measurements, even more SEP distortion is likely to be observed because of the spatial SEP amplitude variation apparent along the array axis. This will be observed in the real array data used in Chapter 6.

## **Chapter 6**

### **Filtering Real SEP Array Data**

In the previous chapters, the method of velocity filtering was studied using simulated signals under ideal conditions. In this chapter, the filter is applied for SA reduction using real array measurements with the aim of assessing its feasibility as a practical means of SA reduction in SEP measurements. The experimental setup for acquiring measurements is described in Section 6.1. The results of filtering these data are given in Section 6.2. Section 6.3 quantitatively analyzes the performance of SA cancellation. Section 6.4 then compares the relative performance of nonlinear segmented ANC against velocity filtering.

#### **6.1 Measurement Setup**

Data were collected from the right arm of 10 healthy, male subjects (S1 to S10) between the ages of 20 and 30 to assess the feasibility of velocity filtering for real-time SA cancellation for clinical SEP monitoring. Figure 1 illustrates the overall measurement setup which is further explained in this section.

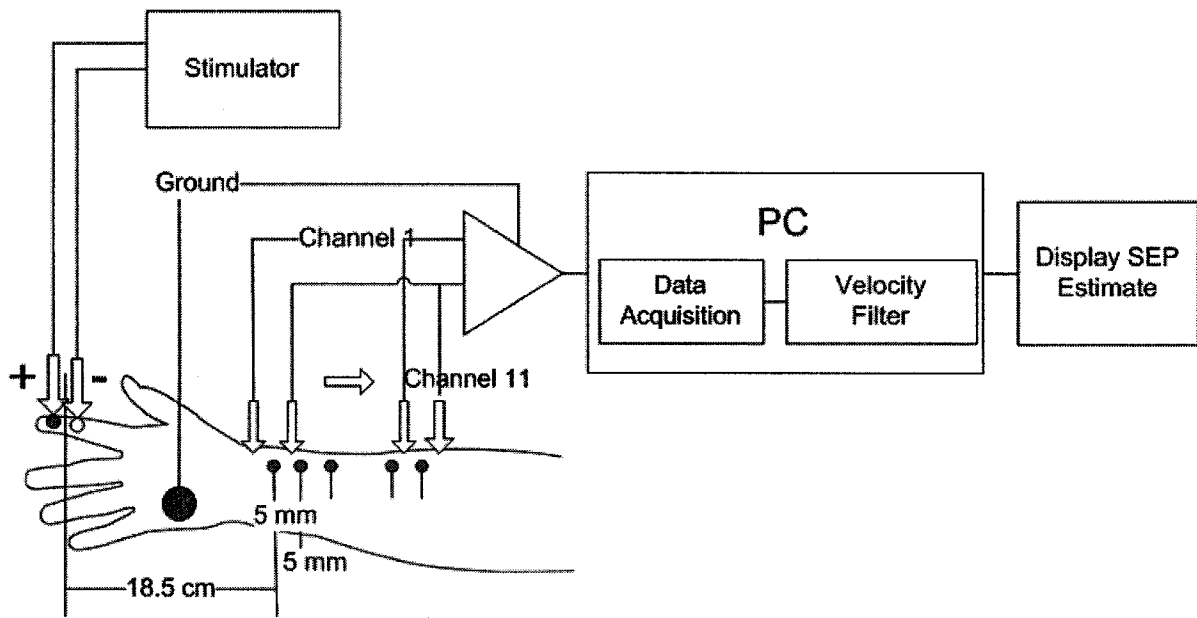


**Figure 6-1: System diagram of SEP recording setup**

The data were also analyzed before filtering to identify characteristics that will affect the performance of this method. This research was reviewed and approved by the Carleton University Research Ethics Committee (CUREC). A consent form which has been signed by all 10 subjects that has been issued by the CUREC is in Appendix B.

### 6.1.1 Stimulation

The median nerve of the right arm was stimulated at the index finger using an S48 stimulator from Grass-Telefactor (division of Astro-Med, Longueuil, QC). This was used with a Grass-Telefactor SIU5 constant-voltage isolation unit to provide electrical isolation. A constant current device may produce measurements that are more repeatable by automatically tracking the required voltage to account for time-varying electrode impedances; however, such a constant current isolation unit was not available for this study. Biphasic current pulses of duration of 0.2 ms were delivered at a rate of 3 per second with an amplitude of

approximately 6 V. This amplitude was varied between 5 and 10 V depending on the threshold of the particular subject.

Grass-Telefactor F-E10S2B bipolar electrodes were used for stimulation. These electrodes have twisted pair leads, 30 mm spacing, and were used with Myo-Jel electrolyte paste from MyoTronics (Tukwila, WA) in order to better match the electrode impedance to the skin impedance. They were placed on the right index finger (palm side) along the nerve axis with the positive electrode at the distal end of the finger as in Figure 6-1.

### **6.1.2 SEP Recording**

The SEP associated with the median nerve was recorded at the right wrist, using a Grass-Telefactor 15A54 Amplifier. The gain of the amplifier was 5000, with a bandwidth of 1 Hz to 6 kHz. A 12-bit PCI-6071E data acquisition board (DAQ) from National Instruments (Austin, TX) was used to sample the measurements. Data were first collected with a sampling rate of 100 kHz in a voltage range of  $\pm 5$  V, and then decimated offline to a 50 kHz sampling rate to ease the computational requirements.

A separate trigger pulse synchronous with each stimulus pulse was directly sent from the stimulator to the DAQ to indicate the starting time of each SEP record and trigger the recording. A 1 ms pre-trigger duration was used in the acquisition. For each SEP trace, 300 triggered records of 10 ms each were collected and ensemble averaged to reduce uncorrelated noise (e.g., electronic, cardiac, power-line, myoelectric).

Myo-Tronics Duo-Trode disposable Ag/AgCl electrodes were used to record the SEP. These contain a pair of bipolar electrodes with a fixed spacing of 20 mm. The reference electrode

was a Red Dot Ag/AgCl electrode from 3M (Montreal, QC). This reference electrode was located midway between the stimulus site and the site of the first recording channel on the palm as in Figure 6-1.

The 11-channel array of SEP recordings along the median nerve axis was implemented manually by collecting each trace individually at different times placed at different locations using the same electrode pair. Ideally all 11 channels would be collected simultaneously using a rigid electrode array but this was done because such an electrode array was not available. For subject S1, the midpoint of the recording electrode pair for the first trace was located on the lower wrist 18.5 cm from the midpoint of the stimulating electrode pair. For other subjects, depending on their size, this distance was slightly adjusted to yield large enough SEP amplitudes over the 5.5 cm measurement window. The channel spacing was set to 5 mm by moving the recording electrode pair proximally along the nerve axis such that the midpoint of the recording electrodes was translated in 5 mm intervals as in Figure 6-1. Data were then acquired and processed offline using Matlab Version 7.0.4. Filter Realization

The velocity filter was realized using an FIR approximation of the ideal impulse response as explained in Section 3.3 and the filter size was truncated to  $21 \times 101$  as in the simulations of Chapter 5. The filter was represented in Matlab as a 2D matrix of filter coefficients and applied to array data using 2D linear convolution as in Section 3.2. Because the output is the center trace and is considered 1D, then the output can also be computed by a sum of  $PM$  1D convolutions, where  $M$  is the spatial length of the filter and  $P$  is the number of times the array data are passed through the filter.

### 6.1.3 Physical Array Implementation

Variations in electrode impedances across different recording channels were minimized by collecting one trace at a time using the same electrodes to record all traces; however, the spatially sampled data are sensitive to the unavoidable human error in position and orientation of the electrodes at each trace. Although care was taken to minimize this error, this source of error will also play a role in the filtering performance. In a more practical scenario, a rigid and accurate array structure would be used to collect all channels simultaneously, and pass directly through an analog-to-digital converter (ADC) connected to a digital velocity filter.

The waveforms containing the SA and SEP at each trace do not necessarily satisfy the assumption of Chapter 2 that the trace-to-trace signal features are spatially invariant along the array axis. Due to the tissue filtering effect and the variable depth of the nerve under the skin surface, the amplitude of the SEP as seen from the skin surface varies with axial distance along the array, which will cause distortion to the velocity filter estimate in the form of a possible scaling and phase-shifting of the SEP estimate as shown in Chapter 3. A phase shift could distort the timing information of the SEP and a scaling factor can distort amplitude information of the SEP; these features are both clinically important. This variable SEP amplitude can be seen in the 11-channel traces of Figure 6.2(b) which was measured from subject S1 and the trace-to-trace SA variation can be seen in Figure 6.2(a). Note that the most critical feature required by the velocity filter to deliver performance is the trace-to-trace latency of the SEP which appears reasonably accurate and constant in Figure 6.2(b).

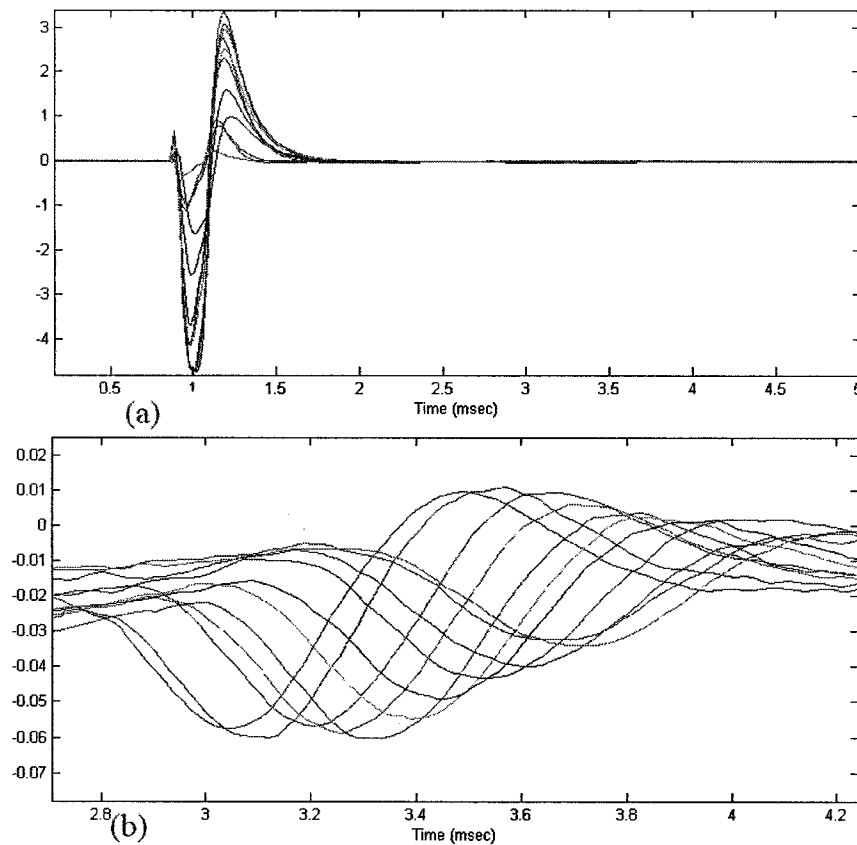


**Figure 6-2:11-channel SEP array measurements from subject S1, (a) raw measurement showing the SA, (b) zoomed in on SEP**

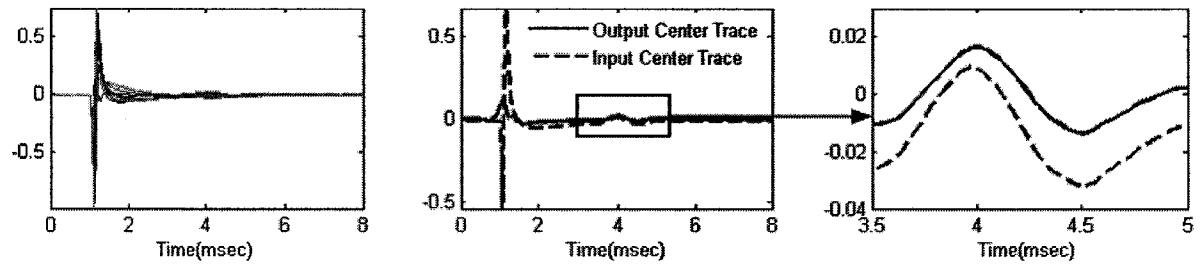
Although the velocity filter may produce an accurate estimate of the SEP shape when using simulated data, Figure 6-2(b) shows that its amplitude at the center trace is not constant across all traces. This was shown in Section 3.4 to yield a scaled and phase shifted estimate for a simple case where the SEP amplitude varies linearly with distance. In this case, the exact distortion introduced to the SEP is difficult to predict and is unlikely to be linear.

## 6.2 Results and Discussion

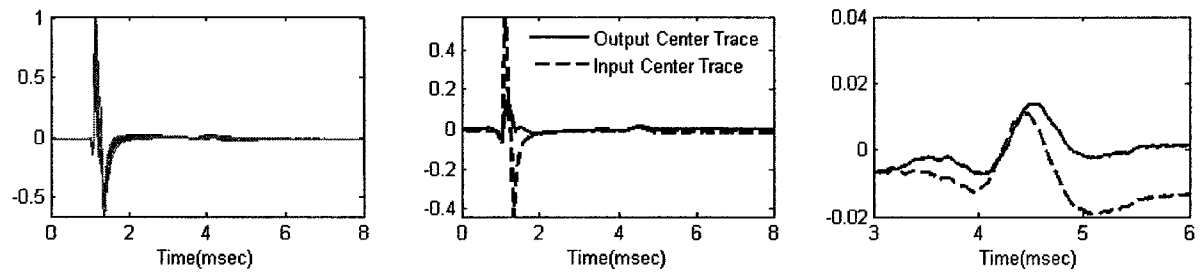
In this section, the results are presented and analyzed for 10 subjects (S1 to S10). Figures 6.3(S1) to (S10) display the 11-channel array data from each subject. These traces contain

raw array data of the SEP distorted by the SA, a comparison of the input versus the output center trace, and the same comparison zoomed into the region containing the SEP after filtering 200 times.

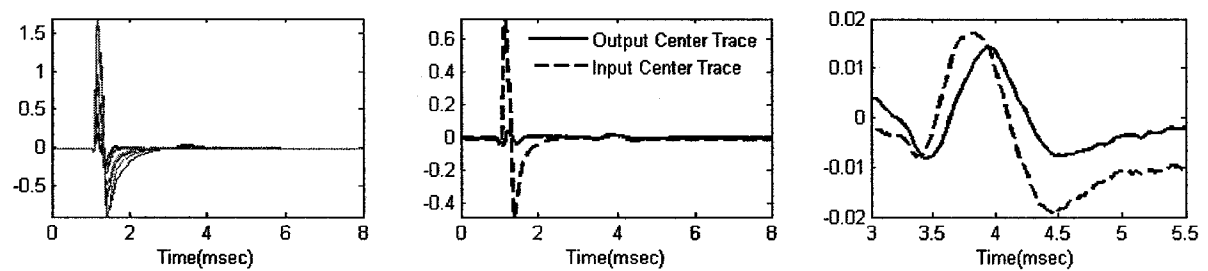
(S1)



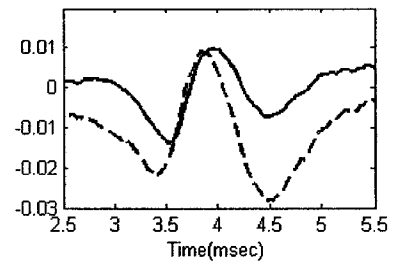
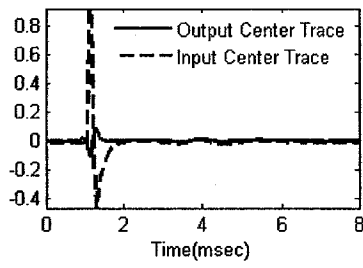
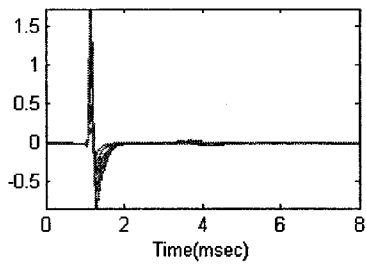
(S2)



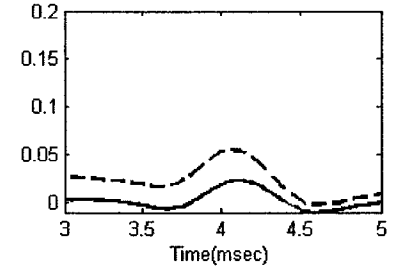
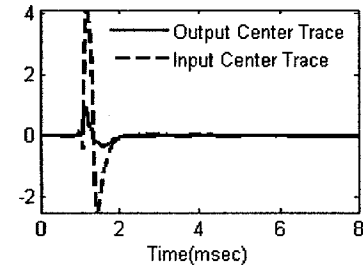
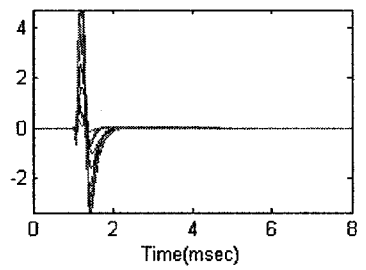
(S3)



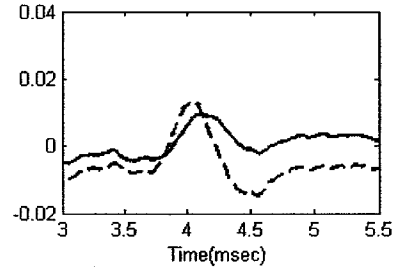
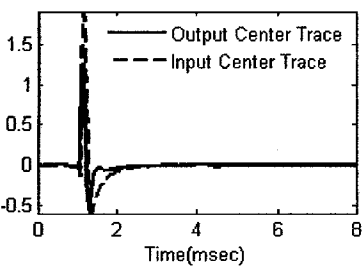
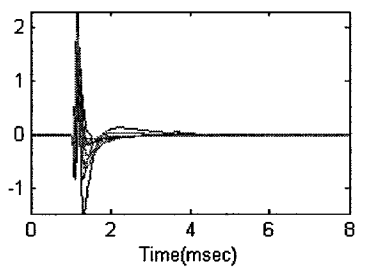
(S4)



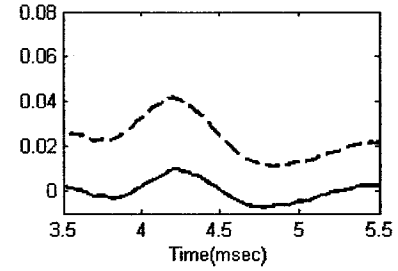
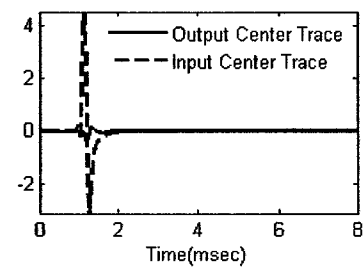
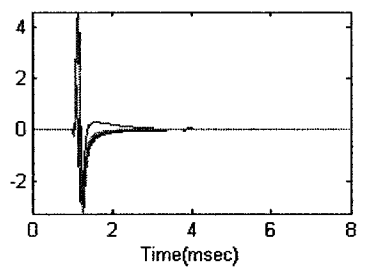
(S5)



(S6)



(S7)



(S8)

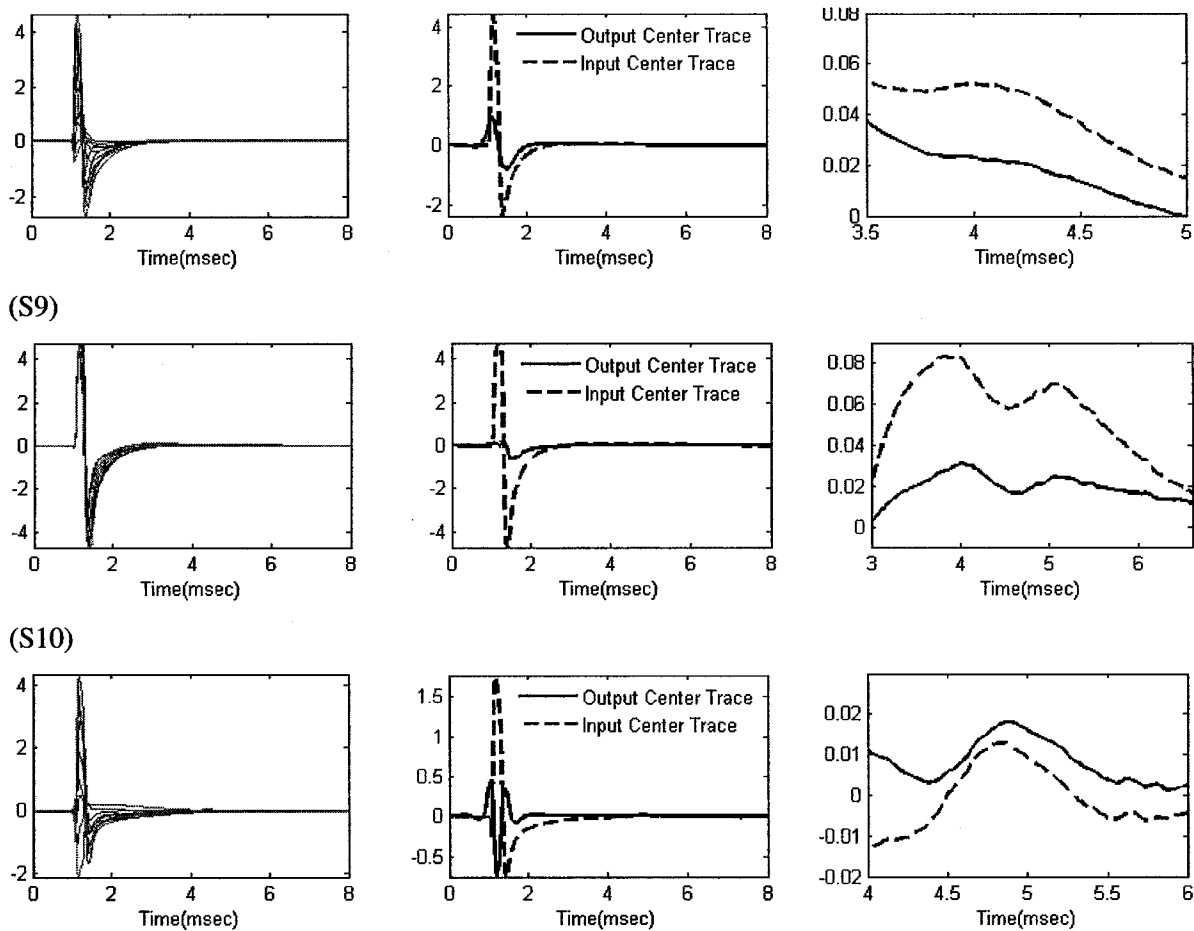


**Figure 6-3: Velocity filtered output, (S1)-(S10): Array data from subject (left), comparison of input and output center trace (middle), comparison of SEP at center trace input and output (right)**

In most cases, a large gain in SNR is observed qualitatively. The traces containing substantial DC components (S1, S2, S5, S7, and S10) are re-centered around zero. More importantly, the traces that are distorted by a curved, sloped, line arising from the stimulus artifact tail are flattened in most cases. The large, fast spike portion of the SA is significantly attenuated in all cases. These observations visually confirm that SA reduction is occurring. The SEP estimate of S6 is tilted upwards and severely scaled with respect to the input. To help explain this, the  $k$ - $\omega$  magnitude spectrum of the array data are shown in Figure 6-4.

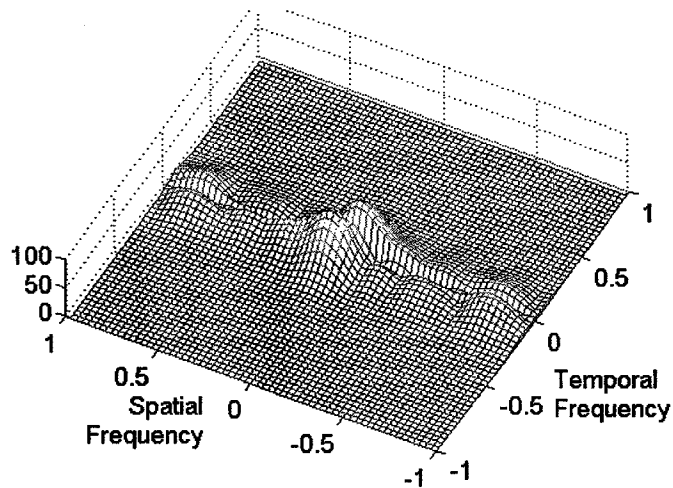


**Figure 6-4: Array data from Subject S6 zoomed into SEP region**

The SA is expected to propagate near the speed of light and its magnitude spectrum should lie along the  $\omega$  axis. From Figure 6-4, it appears that the spectrum of the SA is tilted off center in the  $k$ - $\omega$  plane because of an extra bump appearing in the SA in first few traces and not in the others. The upwards slope of the SEP estimate of S6 must be due to SA spectral content falling into the passband.

An exact measure of performance is not possible because the SEP is considered unknown; therefore, the two  $q$  measures defined in section 5.4 cannot be used to quantify the performance. The three  $\rho$  measures defined in section 5.4, however, are computed and used to indicate some degree of SA cancellation performance.

Table 6-1 summarizes these 3 performance indices for the 10 subjects.

	(S1)	(S2)	(S3)	(S4)	(S5)	(S6)	(S7)	(S8)	(S9)	(S10)
$\rho_1$	6.014	3.837	18.711	10.925	4.530	1.515	23.637	4.660	23.296	3.877
$\rho_2$	4.352	3.767	11.355	7.705	5.197	1.561	11.751	3.195	9.019	2.367
$\rho_3$	0.004	0.002	0.009	0.001	0.002	0.027	0.004	0.019	0.401	0.996

**Table 6-1: Summary of performance indices of velocity filtered SEP estimates for all subjects**

In all cases,  $\rho_1 > 1$  indicates that the SA peak has been attenuated by the filter. In the worst case the SA peak is reduced by a factor of 1.6 and in the best case by 23.6. On average it is attenuated by a factor of 10.1, an order of magnitude. In all cases,  $\rho_2 > 1$  shows that before the onset of the SEP, the standard deviation of the SA and equivalently the energy of the SA has been reduced. In the worst case  $\sigma$  is reduced by a factor of 1.6, in the best case by 11.8, and on average by 6.0. The mean value of the filter output should be close to zero after the onset of the SEP if the SA tail is removed assuming that most of the mean value is attributed to the SA tail and not to the SEP. Since the SEP is orders of magnitude smaller than the SA, a value of  $\rho_3$  that is less than 1 indicates to a large extent a better reduction of the SA tail. This has been achieved in all 10 subjects. The mean squared value after the SEP onset has been increased by a factor of 0.001 in the best case, 0.996 in the worst case, and by 0.15 on average. This suggests good “flattening” of the SA tail after the onset of the SEP.

The dominant sources of error in the performance using real measurements arise from residual SA after filtering and from SEP distortion introduced by the filter. Residual SA is mainly due to limited number of channels in the array data. Distortion is mainly due to

spatial SEP amplitude variation and also to measurement error in the electrodes' position and orientation in the array leading to variations in trace-to-trace SEP latency. The latter may be improved by using a rigid array with high-precision channel spacing that is accurately oriented along the nerve axis. The effect of spatial SEP amplitude variation on the estimate can be predicted and accounted for if the spatial SEP variation is a simple or linear relationship; however, in real measurements the spatial amplitude variation experienced by the SEP cannot be known exactly unless it is measured *a posteriori*. Furthermore, these variations change across subjects, as well as with other parameters such as electrode impedance, stimulus intensity, and moisture of the skin. This is a topic for future research. In this thesis, we go as far as to state that there is spatial variation in the SEP amplitude that will distort the filter estimate unless otherwise accounted for. The amount and the nature of this distortion are difficult to know or predict.

Although the SEP estimate contains distortion and residual SA energy, the result is still a significant improvement upon the unfiltered center trace with the little cost of implementing  $N$  2D convolutions or  $N \times M$  1D convolutions where  $N$  is the number of times the data are passed through the filter and  $M$  is the number of filter traces. It is important to note however that without accurate knowledge of the true nature of the distortion introduced to the SEP by the filter due to spatial SEP variations, amplitude and timing information of the SEP estimate still contain some degree of uncertainty. Thus, to appreciate the full benefit of the velocity filter, this distortion must be accounted for or be measured deterministically. It is suggested that this issue be resolved by pre-processing the array SEP data from a given subject to

estimate the SEP spatial variation, fit this to a model, and apply weighting factors to the filter traces to account for it.

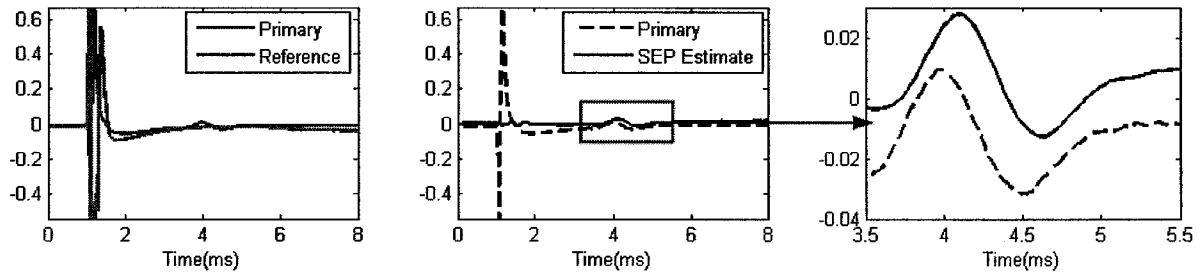
### **6.3 Comparison with Nonlinear ANC – Segmented Training**

In this section, the velocity filtering method was compared against the nonlinear ANC method using segmented training, which is described Chapter 2, using real SEP array measurements. The results are presented, analyzed and compared using the quantitative measures ( $\rho_1$ ,  $\rho_2$ , and  $\rho_3$ ) defined in Section 6.2.

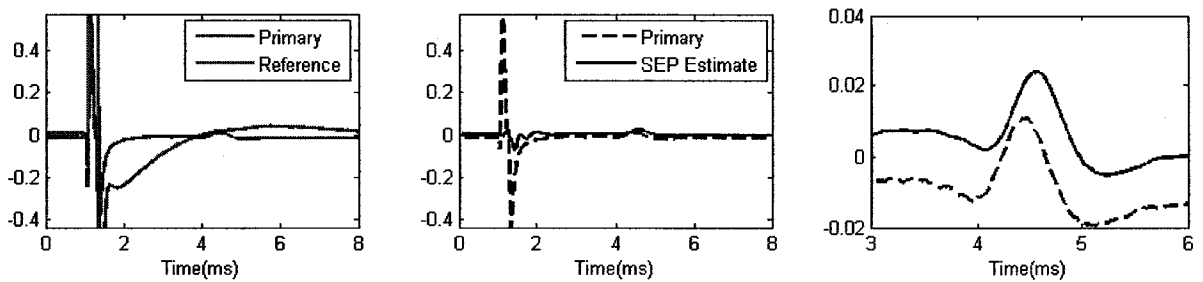
The nonlinear ANC method used one off-nerve channel as the reference input and one composite SA+SEP channel as the primary input. This was done for the same 10 subjects where the primary channel is the center trace of the array data used for velocity filtering. The ANN in this case used a 3 layer MLP structure with 2 input delays, 3 input neurons, and 10 hidden neurons. This structure was empirically found to yield acceptable results although a full exhaustive search was not carried out. This method was very sensitive to the user's choice of where to partition the data set into segments. This partitioning time,  $t_0$  was determined for each case visually and selected as the approximate time just before the onset of the SEP. The sampling rate was 50 kHz for all subjects. Training was stopped when the gradient of the training error with respect to the weights stopped changing between consecutive training epochs. The ANC output was also low-pass filtered using an FIR filter with a cut-off frequency of 10 kHz to remove any high frequency content that the ANN may introduce.

Figure 6-5(S1)-(S10) displays the primary and reference channels measured from each subject, a comparison of the primary channel versus the ANC output, and the same comparison zoomed into the region containing the SEP.

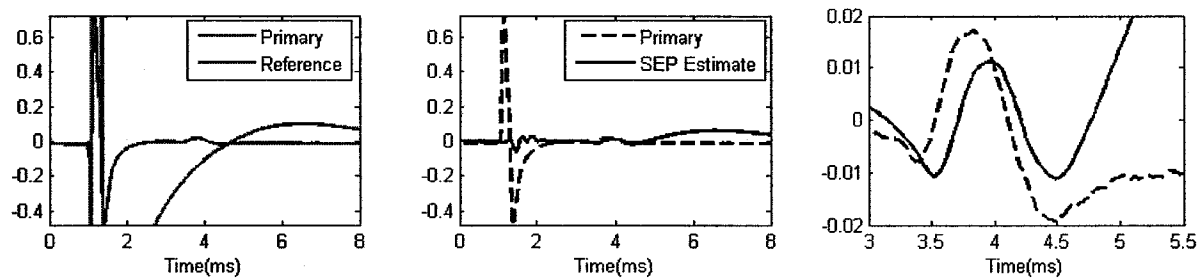
(S1)



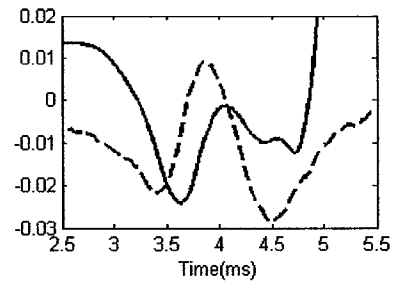
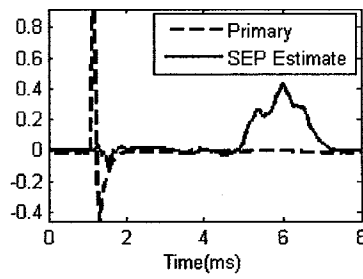
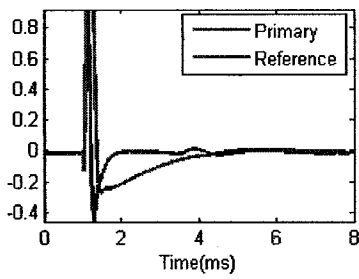
(S2)



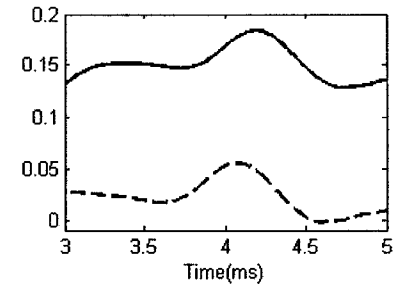
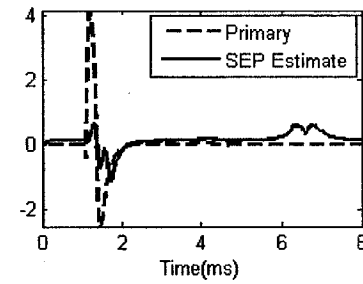
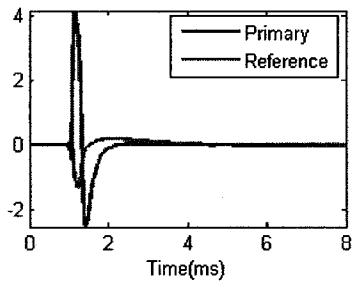
(S3)



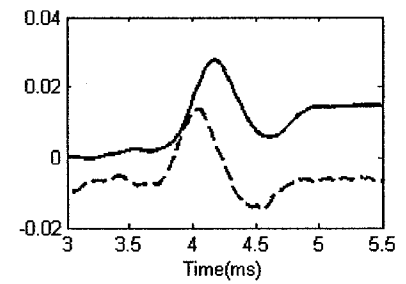
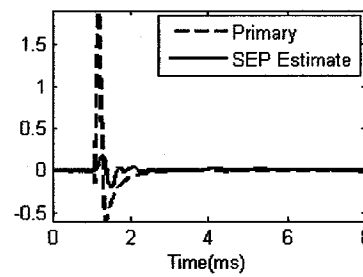
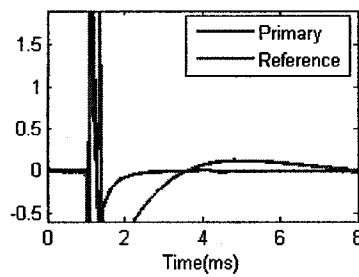
(S4)



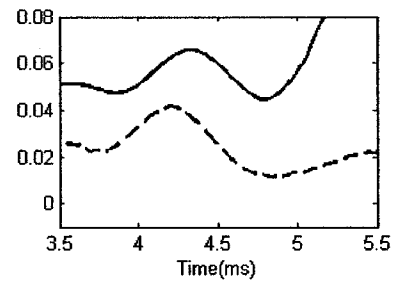
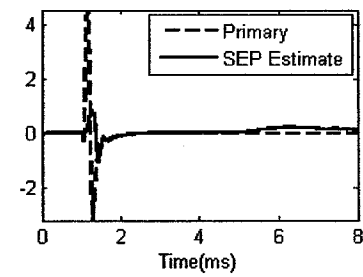
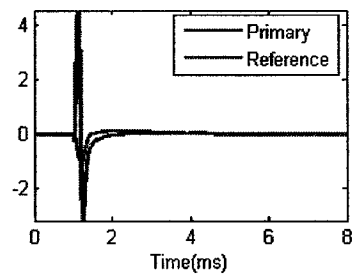
(S5)



(S6)



(S7)



(S8)

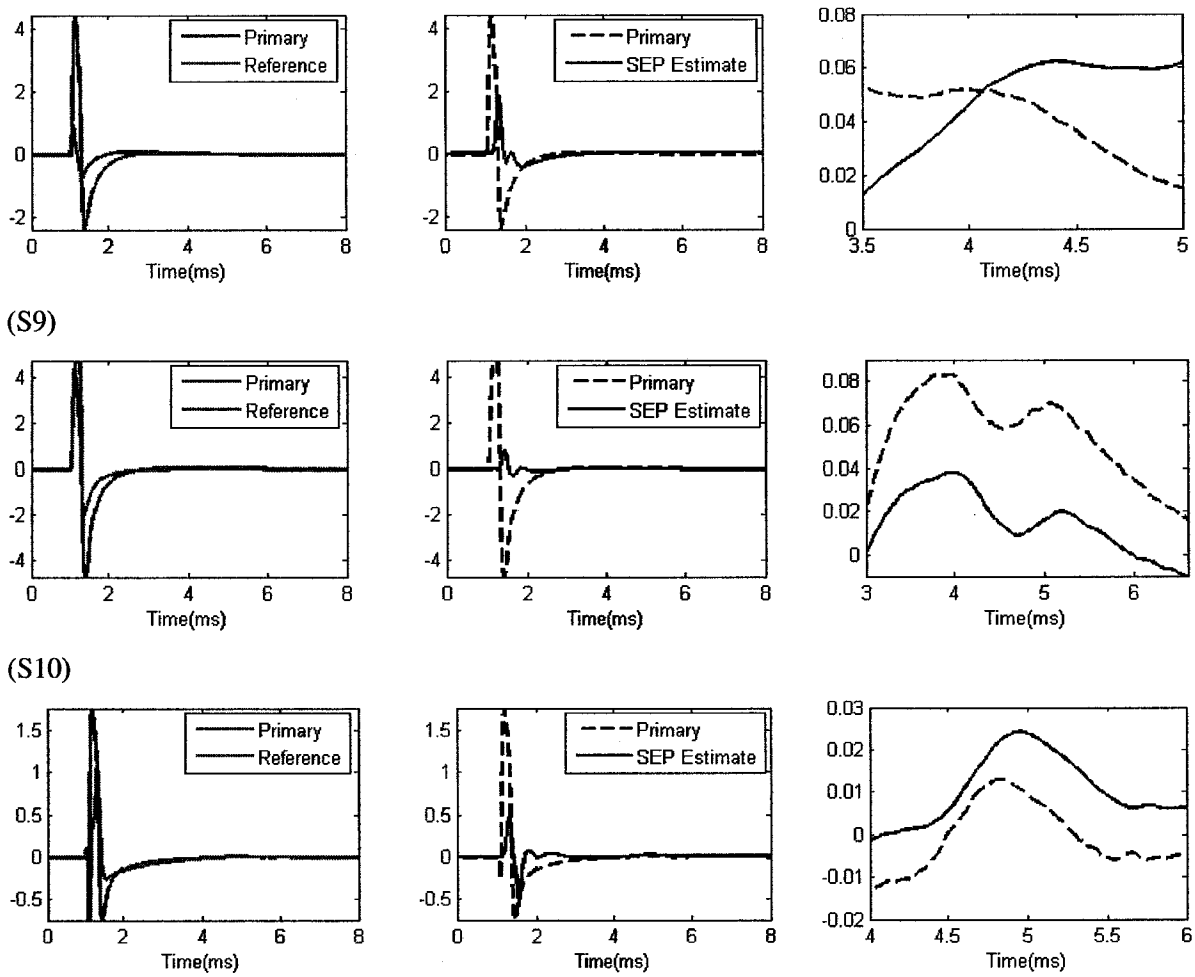


**Figure 6-5: (S1)-(S10)Nonlinear ANC output (segmented training), array data from subject (left), comparison of input and output traces (middle), comparison of SEP at center trace input and output (right)**

	(S1)	(S2)	(S3)	(S4)	(S5)	(S6)	(S7)	(S8)	(S9)	(S10)
$\rho_1$	63.029	44.251	20.985	34.681	6.420	10.583	5.307	2.361	5.902	3.770
$\rho_2$	32.569	8.418	12.793	8.052	3.283	5.934	3.635	2.939	10.891	3.199
$\rho_3$	0.964	0.007	6.257	36.04	159.233	0.420	39.175	264.008	0.143	2.512

**Table 6-2: Summary of performance indices of Nonlinear ANC SEP estimates for all subjects**

Table 6.2 summarizes the 3  $\rho$  performance indices over subjects (S1) through (S10). The mean value of each of these metrics was computed over the 10 subjects for the SEP estimate using the 11-channel velocity filter:

$$\bar{\rho}_1 = 10.100 \quad \bar{\rho}_2 = 6.027 \quad \bar{\rho}_3 = 0.147$$

and using the nonlinear ANC method with segmented training:

$$\bar{\rho}_1 = 19.729 \quad \bar{\rho}_2 = 9.171 \quad \bar{\rho}_3 = 50.876$$

With a larger  $\rho_1$  and  $\rho_2$ , the ANC method outperforms the velocity filter on average in terms of reduction of the SA peak, and in terms of reduction of SA energy before the onset of the SEP. The ANC method achieves better reduction of the SA peak in 6 out of 10 cases, and better reduction of SA energy in 7 out of 10 cases. This is because the ANN learns the relationship between the SA in the primary and reference channels very well in all cases during the time before the onset of the SEP. The attenuation capability of velocity filter on the other hand is primarily determined by the number of data channels used, and on the design of the filter and is fixed for this particular design.

On average, the velocity filter has a smaller  $\rho_3$ , indicating better “flattening” of the SA tail. This is seen in 9 out of 10 cases. In the ANC case, the correlation between the SA in the primary and reference channels is high before the onset of the SEP; however this is not the case for the SA tail after the SEP onset, especially for subjects S2, S3, and S6 from Figure 6-5. The velocity filter has the advantage of not depending on how a reference is related to the coherent interference. Accordingly, it achieves better reduction in the SA tail because it is only concerned with the propagation velocity.

The distributions of these metrics over the 10 subjects are also plotted in Figure 6-6. S1 and S2 for the ANC case appear to have very large SA peak reduction. This is because for those particular subjects, the reference SA was highly correlated with the SA in the primary channel as compared to the other subjects due to their tissue properties. This is also seen for S1 in the second plot for reduction in standard deviation of the SA. The ANN therefore learns the relationship very accurately because it is a simple relationship.

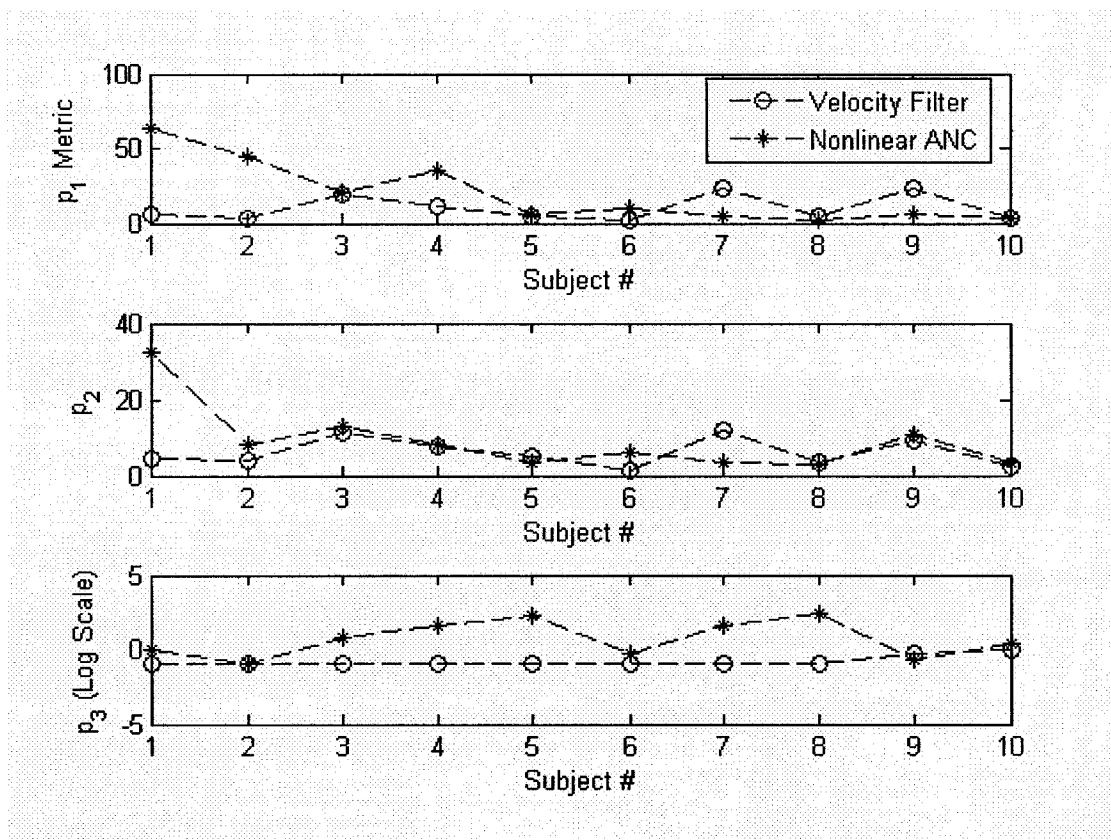


**Figure 6-6: Comparison of performance metrics for velocity filter and nonlinear ANC, (a)  $p_1$  measure, (b)  $p_2$  measure, (c)  $p_3$  measure**

In comparing the 2 methods, it is important to note that the performance reported using the ANC method was only attained after trial and error was used to select the best value of  $t_0$ ,

and training was repeated in some cases many times from scratch before convergence was reached. Performance of the SEP estimate using nonlinear ANC is also a strong function of the ANN structure, and the amount of training data. This was not exhaustively examined because it was not the aim of this thesis. The same ANN structure was used for all 10 subjects for this comparison and although the “optimal” ANN structure may differ for each subject, in a practical implementation a fixed ANN structure may be required. The most important metric is  $\rho_3$  because this is computed during the region containing the SEP. Under this criterion, the velocity filter outperforms the ANC method achieving better reduction of the SA tail. It should be noted that this metric is not a complete description of performance as it does not convey how much distortion is suffered by the SEP. From the results of the simulation study in chapter 5, it would suggest that some distortion is likely to have occurred. This distortion is also likely to be higher than the simulation results as there are other factors that would contribute to the distortions, including the variation in the SEP and SA between channels and measurement errors (e.g. accuracy of channel spacing).

It was noted in Chapter 2 that another ANN-based ANC paradigm called sub-threshold training [6] was proposed to learn a simpler relationship between stimulus intensity and SA waveform at subthreshold stimulus levels and generalize this to supra-threshold levels. This method avoids temporal generalization and simplifies the ANN learning criteria, but the data collection is time-consuming and still requires supervised ANN training and human supervision.

## 6.4 Conclusions

Qualitatively, an improvement can be observed in the SNR of the SEP for all subjects. In most cases, a DC level has been removed and a sloped, curved SA tail is reduced or removed. The SA cancellation metrics defined in Section 6.2 indicate that the peak amplitude of the SA is significantly reduced, the overall SA energy is also significantly reduced during the time before the onset of the SEP. After the onset of the SEP, the mean value has been set closer to zero in all cases indicating reduction of the SA tail.

In comparing velocity filtering against the ANN-based ANC method it was shown that for the first 2 criteria, the ANC method has outperformed the velocity filter on average. This indicates that the peak reduction and the energy reduction of the SA were greater in the case of ANC than for the velocity filter. The third criterion shows that the velocity filter achieves greater reduction of the SA tail on average and in 9 out of 10 cases. This result is important because the time interval containing the SEP is where SA reduction is most important for recovering an estimate of the SEP as this is where they temporally overlap.

Although better SA reduction is achieved using the velocity filter in the time interval containing the SEP, it should be carefully noted that the  $\rho_3$  metric is only a partial indicator of performance in terms of estimating the SEP as it does not give any information about how much the SEP is distorted by the filter. It is likely for SEP distortion to be greater for the case of velocity filtering than for the case of nonlinear ANC if the ANN is made to achieve accurate performance. This is not only because the data are passed through the filter many times, but also because the SEP amplitude varies spatially as seen from the skin surface as it propagates down the array. This variation may not be modeled in a general or accurate way

because it is specific to the physiology of a given subject. Distortion due to factors such as the limited number of channels and filter characteristics can be predicted and reduced by careful design, but unfortunately the distortion due to spatially varying SEP amplitude is a source of error with outcomes that are currently uncertain. This distortion consisted of a scaled and phase shifted term passing through the filter and combining with the center trace SEP for the simple case where the SEP amplitude changes linearly with distance as shown in Chapter 3, but this is by no means an accurate or general description of the actual SEP spatial variation.

The purpose of SA cancellation was to remove uncertainty in the clinically important SEP features such as amplitude and latency that were obscured by SA distortion. Although a good deal of SA cancellation has been achieved, the true nature of the distortion in the SEP estimates due to velocity filtering of the spatially varying SEP is also uncertain in phase and amplitude. Accordingly, methods of measuring SEP distortion or ensuring low distortion are required to ensure the quality of velocity filtered SEP estimates if they are to be used in a clinical setting for real-time SA cancellation.

In a similar sense, the SEP estimates achieved by nonlinear ANC are also uncertain to some degree. In this method uncertainty arises due the nature of the data, because of the uncertainty in the relationship between the SA in the primary and reference channels. Uncertainty is also inherent in the learning ability of the ANN.

It is suggested that distortion in the SEP estimate due to spatial SEP variation could be reduced or removed using other techniques. Pre-processing of the array data prior to filtering

may be used to model or estimate the spatial variation of the SEP amplitude in the array data. This knowledge could then be used to correct the filter estimate, by adding weighting factors to the filter traces to account for the variations. This is a topic for further research.

The main advantage of using a nonlinear ANC scheme as opposed to the velocity filter is that it can always be made to perform to any required degree of accuracy if the network structure and training data set are made large enough and training is not limited by time. This is only guaranteed with trial and error and human supervision. The nonlinear ANC method also makes more efficient use of data, requiring only 2 channels, one primary and reference to extract enough information to estimate the SEP. The computational cost is comparable to that of the velocity filter because the ANN must be trained. The velocity filter on the other has a more systematic implementation that can be automated, produces results that are more general and repeatable because it operates solely on apparent velocity, and may yield an SEP estimate in a very short time.

## Chapter 7

### Conclusions

#### 7.1 Summary and Conclusions

The main objectives of this thesis were to show that velocity filters may be used to attenuate coherent stimulus artifact interference in SEP measurements and to determine whether this method is a practical choice for real-time clinical SA cancellation in SEP measurement.

The velocity filtering method was demonstrated theoretically in Chapter 3, noting that the performance is limited by factors such as the number of available channels which limits spatial frequency resolution, of spatial and temporal sampling rates, which influence a velocity resolution, and of spatial variations in SEP amplitude seen at different locations along the array.

In Chapter 4, it was shown by simulation that a velocity filter can effectively separate signals propagating at different velocities along the axis of an array of electrodes. It was shown that the sampling rate should be chosen as a tradeoff between attenuation of the fast signal and distortion of the slow signal. It was also shown that the numbers of channels and the channel spacing have strong influences on the filtering performance and that having only  $N$  spatial data channels available means that no more than  $2N-1$  filter channels will be useful when filtering multiple times. This causes a virtually truncated number of filter channels that will contribute to the velocity filtered output. Spatial SEP amplitude variation in the array data was also shown to significantly degrade the filtering performance.

In Chapter 5, using 11 channels of simulated data, 5 mm spacing, and 50 m/s propagation, the PRD performance was measured to be 21.1% after filtering 200 times. The simulated data consisted of an identical SA waveform at every trace to simulate its high velocity; and an SEP waveform that was only time-delayed between traces to simulate its low velocity. When compared against a nonlinear ANC technique using an ANN and segmented training approach, the velocity filter was found to perform better in terms of the PRD of the estimate, attenuation of the SA peak, and reduction of SA energy outside the region containing the SEP. The PRD of the SEP inside the time interval where the SEP is non-zero was lower for the ANC method than that for the velocity filter indicating distortion of the SEP by the filter.

In Chapter 6, SEP array data from 10 subjects was velocity filtered and the output center trace estimate of the SEP was compared with the center trace of the input. The performance cannot be deterministically measured, but improvement in SNR can be seen. This was compared against the nonlinear ANC method using segmented training. Using SEP array data from 10 subjects, the nonlinear ANC method out-performed the velocity filter in terms of reduction in the SA peak, reduction of the overall SA energy before the onset of the SEP. The velocity filter outperformed the ANC method in terms of reduction of the mean-squared value of the SA tail after the onset of the SEP. It was concluded that better reduction of the SA tail is achieved using an 11-channel velocity filter with 5 mm spacing than using the ANC method. Velocity filtering as a practical method for real-time SA cancellation is only clinically acceptable if it can preserve the original SEP information without introducing new uncertainty into the SEP amplitude and latency. Accordingly, it is necessary to develop a method that would pre-process the array data to estimate the spatial SEP variation, and use

this knowledge to estimate the resulting distortion and account for it. This is a topic for further research.

## **7.2 Contributions**

### **7.2.1 Minor Contributions**

1) The 2D Fourier Transforms have been formulated for general spatio-temporal signals with lossless propagation at constant velocities. The 2D spatio-temporal impulse response of the velocity filter has been formulated from the ideal frequency response. This allows for a full analytical description of velocity filtering.

2) The theory of velocity filtering was confirmed by simulation under ideal conditions using sinc pulses with a flat spectrum that is bandlimited.

3) It was shown theoretically and by simulation that the number of channels limits spatial frequency resolution in the array data and that PRD performance of the filtered estimate is inversely proportional to the number of channels.

4) Spatial variation of the SEP amplitude was shown to introduce distortion in the form of a filtered, scaled and phase-shifted term to the velocity filtered SEP estimate in the case of the SEP amplitude varying linearly with distance. A distorted SEP estimate was also obtained through simulation by synthesizing an array of SEP measurements where the SEP amplitude was an exponentially decaying function of distance. It was further explained that the actual spatial variation of the SEP amplitude is more complicated than a linear function and phase and amplitude distortion are likely to be more severe and unpredictable in real SEP measurements.

5) It was shown that the velocity filter can achieve greater SA reduction than nonlinear ANC, but is also more likely to distort the SEP estimate than the ANC method.

6) It was concluded that to justify the use of velocity filters in clinical SEP monitoring, new methods are required to account for SEP distortion that results from spatial SEP amplitude variation.

### **7.2.2 Major Contributions**

1) A new velocity filtering method has been proposed to meet the requirements of real-time SA cancellation in clinical SEP monitoring that addresses the limitations of the current methods.

2) A detailed study of the difficulties and practical limitations of applying velocity filters to SEP array data recorded on the median nerve has been carried out. The advantages and disadvantages have been discussed and weighed using quantitative measures, and compared against an existing nonlinear ANC-based method.

3) Analysis of the SA cancellation performance of velocity filters using simulated data and real data have revealed the conclusions that the velocity filter achieves a large gain in SNR; however distortion arising from spatial SEP variation introduces uncertainty in the amplitude and latency of the SEP estimate.

4) A database of array data of SEP measurements from 10 subjects has been established and examined. This may be used for future research.

5) Performance metrics have been used to measure the SA cancellation performance of velocity filtering and compared against that of a nonlinear ANC method using simulated data and real data.

### **7.3 Future Work**

The most immediate requirement for future work is to address the problem of distortion that the filter introduces to the SEP estimate due to spatial SEP variation. If the spatial SEP amplitude variation can be accurately modeled, or can be approximated by pre-processing the array data, then this information may be used to remove or account for the variation by attempting to normalize the SEP in all traces, or adding weighting factors the filter traces. Also, if information about the spatial variation is known, and the number of channels is limited as in this study with 11 channels, then it may be possible to spatially extrapolate more data to increase the effective number of channels used by the filter. Increasing the number of channels always improves the quality of the velocity filter estimate, which is normally limited by spatial resolution. The number of channels can be increased until there are enough channels to resolve one full wavelength of the smallest spatial frequency contained in the array data.

In this thesis, focus was placed on the SEP recorded on the median nerve at the wrist when stimulated at the index finger. When stimulating and recording SEPs on the spinal cord during spinal surgery from the skin surface, the depth of the nerve is more constant and more data channels would be available. In this case, the ability to reject the SA without distorting the SEP with a velocity filter should be much greater. This would significantly facilitate

spinal SEP monitoring applications, as the surgeon would have little trouble measuring important features of the presence of the SEP when it is not embedded in a large stimulus artifact.

The fan filter impulse response may be realized using an IIR approximation yielding better roll-off characteristics. Different filter design methods should be explored. A simple method was used in this work as this was not the focus of this thesis. Different window functions need to be explored as well that can improve fan filter accuracy based on known characteristics of the SA and SEP and where they are localized in time. A simple window method was used in this work as this was not the focus of this thesis.

The FIR approximation may also be realized in hardware using standard digital blocks such as adders, multipliers, and delays. A fan filter implemented in an FPGA or ASIC would allow for real-time SA cancellation in a clinical setting. The system could be directly connected to the electrode array and to the measurement instrumentation so that SA cancellation occurs automatically. In a real clinical setting, this would reduce cost, waiting time, and computing resources. With less uncertainty in these SEP measurements due to real-time SA cancellation, diagnosis of neuromuscular disorders and nerve damage, and spinal SEP monitoring during surgery could be done faster and more reliably.

## References

- [1] R.N.Scott, L.McLean, P.A.Parker "Stimulus Artefact in Somatosensory Evoked Potential Measurement," *Medical & Biological Engineering & Computing*, vol.35, 1997, pp.211-215
- [2] B. H. Boudreau, "Modeling Stimulus Artifact Generation in Noninvasive Somatosensory Evoked Potential Measurements," M.Sc.E. Thesis, University of New Brunswick, Fredericton, N.B., Canada, 2000
- [3] M. R. Isley, G. L. Krauss, K. H. Levin, "Electromyography/Electroencephalography – Biophysical Measurement Series," © Spacelabs Medical Inc., 1993
- [4] S. B. Harrison, D. F. Lovely, "Identification of Noise Sources in Surface Recording of Spinal Somatosensory Evoked Potentials," *Medical & Biological Engineering & Computing*, vol.33, 1995, pp.299-305
- [5] R. Grieve, P. A. Parker, B. Hudgens, K. Englehart, "Nonlinear Adaptive Filtering of Stimulus Artifact," *IEEE Transactions on Biomedical Engineering*, vol. 47, no. 3, March, 2000
- [6] B. H. Boudreau, K. B. Englehart, A. D. C. Chan, P. A. Parker, "Reduction of Stimulus Artifact in Somatosensory Evoked Potentials: Segmented Versus Subthreshold Training," *IEEE Transactions on Biomedical Engineering*, vol. 51, no. 7, July, 2004
- [7] B. Farhang-Boroujeny, "Adaptive Filters, Theory and Application," © John Wiley & Sons, 1998
- [8] J. W. Clark Jr., "Medical Instrumentation, Application and Design," John G. Webster, Editor, © John Wiley & Sons, 1998
- [9] J. M. Guerit, "Neuromonitoring in the Operating Room, why, when and how to monitor?" *Electroencephalography and Clinical Neurophysiology*, vol. 106, 1998, pp. 1-21

- [10] S. Haldeman, "The Electrodiagnostic Evaluation of Nerve Root Function," *Spine*, vol. 9, 1984, pp. 42-48
- [11] M. Smorto, J. Basmajian, "Clinical Electroneurography," © Williams and Wilkins Company, Baltimore, 1979
- [12] S. J. Oh, Lippincott, "Clinical Electromyography: Nerve Conduction Studies: Third Edition," © Williams and Wilkins Company, Baltimore, 2003
- [13] Y. Hua, "Factors Affecting the Stimulus Artifact Tail in Surface Recorded Somatosensory Evoked Potentials," MscE Thesis, University of New Brunswick, Fredericton, N.B., Canada, 2005
- [14] Y. Hua, D. F. Lovely, R. Doraiswamy, "Factors Affecting the Stimulus Artifact Tail in Surface Recorded Somatosensory Evoked Potentials," *Medical & Biological Engineering & Computing*, vol. 44, no. 3, March, 2006, pp. 226-241
- [15] Grass Telefactor, "Instruction Manual: Model S48K Square Pulse Stimulator," © Grass Instrument Division, Astro-Med, Inc., 1996
- [16] V. Parsa, P. A. Parker, R. N. Scott, "Adaptive Stimulus Artifact Reduction in Noncortical Somatosensory Evoked Potential Studies," *IEEE Transactions on Biomedical Engineering*, vol. 45, no. 2, February, 1998
- [17] W. G. Stevens, "The Current-Voltage Relationship in Human Skin," *Medical & Biological Engineering & Computing*, vol.1, 1963, pp.389-399
- [18] Q.J. Zhang, K.C. Gupta, V.K. Devabhaktuni, "Artificial Neural Networks for RF and Microwave Design-From Theory to Practise," *IEEE Transactions on Microwave Theory and Techniques*, vol. 51, no. 4, April, 2003
- [19] J. P. Fail, G. Grau, "Les filters en envetail," *Geophysical Prospecting*, vol. 11, June, 1963, pp. 9-163

- [20] K. L. Peacock, "On the Practical Design of Discrete Velocity Filters for Seismic Data Processing," *IEEE Transactions on Acoustics, Speech, and Signal Processing*, vol. ASSP-30, no. 1, February, 1982
- [21] D. W. McCowan, P. L. Stoffa, J. B. Diebold, "Fan Filters for Data with Variable Spatial Sampling," *IEEE Transactions on Acoustics, Speech, and Signal Processing*, vol. ASSP-32, no. 6, December, 1984
- [22] K. Nishikawa, H. Ohno, X. Tang, T. Kanamori, H. Naono, "A Design Method of 2D Fan Filters for Wideband Beam Forming by Means of 2D Fourier Series Approximation," *Electronics and Communications in Japan*, part. 3, vol. 85, no. 7, 2002
- [23] A. E. Gerheim, "A Synthesis Procedure for 90° Fan Filters," *IEEE Transactions on Circuits and Systems*, vol. CAS-30, no. 12, December, 1983
- [24] E. Z. Psarakis, V. G. Mertzios, G. P. Alexiou, "Design of Two-Dimensional Zero Phase FIR Fan Filters Via the McLellan Transform," *IEEE Transactions on Circuits and Systems*, vol. 37, no. 1, January, 1990
- [25] N. Jiang, "Modelling of Motor Unit Innervation Process Correlation and Motor Unit Common Drive in Human Skeletal Muscles," MscE thesis, University of New Brunswick, 2004
- [26] J. Vlach, K. Singhal, "Computer Methods for Circuit Analysis and Design," New York: Van Nostrand, 1983
- [27] V. Parsa, P. A. Parker, "Multireference Adaptive Noise Cancellation Applied to Somatosensory Evoked Potentials," *IEEE Transactions on Biomedical Engineering*, vol. 41, no. 8, August, 1994
- [28] K. C. McGill, K. L. Cummins, L. J. Dorfman, B. B. Berlizot, K. Luetkemeyer, D. G. Nishimura, B. Widrow, "On the Nature and Elimination of Stimulus Artifact in Nerve Signals

Evoked and Recorded Using Surface Electrodes”, IEEE Transactions on Biomedical Engineering, Vol.BME-29, No.2, February 1982

[29] U. S. Inan, A. S. Inan, “Electromagnetic Waves,” © Prentice Hall, 2000

[30] Sankar Basu, Alfredo C. Tan, “Adaptive 1-D and 2-D Filtering with Internally Passive Structures,” International Journal of Electronics and Communications, (AEU), 55, no.6, pg. 397-407, 2001

[31] Thomas J. Herbert, “The Ionic Basis for the Action Potential,” University of Miami [http://www.bio.miami.edu/tom/bil255/bil255goods/action\\_potential.html](http://www.bio.miami.edu/tom/bil255/bil255goods/action_potential.html), last visited May, 2006

[32] A. Hodgkins, A. Huxley, “A Quantitative Description of Membrane Current and Its Application to Conduction and Excitation in Nerve”, J. Physiol., vol.117, pg.500-544, 1952

[33] S. Trietel, J. L. Shanks, C. W. Frasier, “Some Aspects of Fan Filtering,” Geophysics, , vol. XXVII, no. 5, pg. 801-818, October, 1967

[34] M. T. Hanna, “Design and Implementation of Velocity Filters Using Multichannel Array Processing Techniques,” IEEE Transactions on Acoustics, Speech, and Signal Processing, vol. ASSP-35, no. 6, June, 1987

[35] L.R.Rabiner, B.Gold , “Theory and Application of Digital Signal Processing,” © Prentice Hall, 1975

[36] GENESIS (General Neural Simulation System), © California Institute of Technology,  
<http://www.genesis-sim.org/GENESIS/>, 1988-2001, last visited September 19, 2006

[37] R. Pallas-Areny, J.G. Webster, "Composite Instrumentation Amplifier for Biopotentials,"  
*Annals of Biomedical Engineering*, vol.18, pg.251-262, 1990

## Appendix A

### Derivation of Fan Filter Impulse Response

$$\begin{aligned}
 f(x,t) &= \frac{1}{2\pi} \frac{1}{2\pi} \int_{-\infty}^{\infty} \int_{\frac{|k|}{v_c}}^{\frac{|k|}{v_c}} e^{j\omega x} e^{jkx} \partial\omega \partial k \\
 &= \frac{1}{4\pi^2} \int_{-\infty}^{\infty} e^{jkx} \operatorname{sgn}(k) \int_{\frac{k}{v_c}}^{\frac{k}{v_c}} e^{j\omega x} \partial\omega \partial k \\
 &= \frac{1}{4\pi^2} \int_{-\infty}^{\infty} e^{jkx} \operatorname{sgn}(k) \left( \frac{1}{jt} \left[ e^{j\omega x} \right]_{\frac{k}{v_c}}^{\frac{k}{v_c}} \right) \partial k \\
 &= \frac{1}{4\pi^2} \frac{2}{t} \int_{-\infty}^{\infty} \operatorname{sgn}(k) \left( \frac{e^{j\frac{kt}{v_c}} - e^{-j\frac{kt}{v_c}}}{2j} \right) e^{jkx} \partial k \\
 &= \frac{1}{4\pi^2} \frac{2}{t} \int_{-\infty}^{\infty} \operatorname{sgn}(k) \sin\left(\frac{kt}{v_c}\right) e^{jkx} \partial k \\
 &= -\frac{1}{4\pi^2} \frac{2}{t} \int_{-\infty}^{\infty} (j \operatorname{sgn}(k)) \left( j \sin\left(\frac{kt}{v_c}\right) \right) e^{jkx} \partial k \\
 &= g(t) \mathfrak{S}^{-1} \{Z(k)Y(k)\} \\
 &= g(t) [z(x) * y(x)]
 \end{aligned}$$

where  $g(t) = -\frac{1}{4\pi^2} \frac{2}{t}$ ,  $Z(k) = j \operatorname{sgn}(k)$ ,  $Y(k) = j \sin\left(\frac{kt}{v_c}\right)$

$$z(x) = \frac{1}{\pi x} \text{ (Hilbert Transform Operator)}$$

$$\begin{aligned}
 y(x) &= \int_{-\infty}^{\infty} j \sin\left(\frac{kt}{v_c}\right) e^{jkx} \partial k \\
 &= \int_{-\infty}^{\infty} \frac{e^{j\frac{kt}{v_c}} - e^{-j\frac{kt}{v_c}}}{2} e^{jkx} \partial k
 \end{aligned}$$

$$\begin{aligned}
&= \frac{1}{2} \left[ \int_{-\infty}^{\infty} e^{j\frac{kt}{v_c}} e^{jkx} \partial k - \int_{-\infty}^{\infty} e^{-j\frac{kt}{v_c}} e^{jkx} \partial k \right] \\
&= \frac{1}{2} \left[ \int_{-\infty}^{\infty} e^{jk\left(x+\frac{t}{v_c}\right)} \partial k - \int_{-\infty}^{\infty} e^{jk\left(x-\frac{t}{v_c}\right)} \partial k \right] \\
&= \frac{1}{2} \delta\left(x+\frac{t}{v_c}\right) - \frac{1}{2} \delta\left(x-\frac{t}{v_c}\right)
\end{aligned}$$

$$\therefore f(x,t) = g(t) [z(x) * y(x)]$$

$$\begin{aligned}
&= -\frac{1}{4\pi^2} \frac{2}{t} \left[ \frac{1}{\pi x} * \left( \frac{1}{2} \delta\left(x+\frac{t}{v_c}\right) - \frac{1}{2} \delta\left(x-\frac{t}{v_c}\right) \right) \right] \\
&= \frac{1}{4\pi^2} \frac{2}{t} \left[ \frac{1}{\pi x} \right] * \left[ \frac{\delta\left(x-\frac{t}{v_c}\right)}{2} - \frac{\delta\left(x+\frac{t}{v_c}\right)}{2} \right] \\
&= \frac{1}{4\pi^2} \frac{1}{t} \left[ \hat{\delta}\left(x-\frac{t}{v_c}\right) - \hat{\delta}\left(x+\frac{t}{v_c}\right) \right]
\end{aligned}$$

## **Appendix B**

### **Carleton University Research Ethics Committee Consent Form**

CARLETON UNIVERSITY  
DEPARTMENT OF SYSTEMS AND COMPUTER  
ENGINEERING

---

## **INFORMED CONSENT**

### **Electroneurogram Research**

#### **Investigator**

**Dr. Adrian D.C. Chan** (Principal Investigator)  
Carleton University  
Department of Systems and Computer Engineering  
1125 Colonel By Drive  
Ottawa ON  
K1S 5B6  
613-520-2600 ext. 1535

#### **Feedback**

I may contact one of the investigators for consultation of any concerns I have about the research. In addition, I may also request any publications and information about the final results or conclusions from the study.

#### **Purpose**

This research will study electroneurogram (ENG) – nerve signals.

Electroneurograms (nerve signals) can provide information about the integrity of the nervous system. These signals are useful in clinical diagnoses, treatment, and monitoring of diseases such as carpal tunnel syndrome.

Nerve signals can be elicited using an electrical stimulus, and monitored non-invasively using electrodes on the surface of the skin. Surface signals, however, are more susceptible to noise and interference, as well as providing information that is less localized. In this research project, the researcher seeks to find effective ways of processing nerve signals to enhance their quality (ie. signal-to-noise ratio) and/or to provide some automatic classification (ie. pattern recognition).

**Should the experimenter note any unusual readings during the course of the experiment the study will be stopped immediately. The experimenter is not a physician and cannot make a medical diagnosis. I will be asked to contact my family physician. The researcher will contact my physician in writing explaining why the experiment was stopped. I may not return to the study or undertake any further experiments without the written consent of my physician.**

### **Procedure**

I understand that surface electrodes with conductive gel will be placed on me to deliver an electrical stimulus and to acquire the necessary ENG signals. Depending on the study, the number and exact placement of the electrodes may vary. In general, one electrode will deliver electrical stimuli (eg. to my fingertip or ankle), and multiple electrodes will monitor my nerve signals. A maximum of 8 simultaneous channels will be used to monitor my nerve signals.

**I have been fully informed of the study that I am participating in.**

Given the range of experiments I understand that I am being asked to participate in:

electroneurogram signal study that requires the application of surface electrodes and electrical stimuli.

The risk involved is similar to that of obtaining an ECG (cardiac) record (i.e. slight irritation of the skin under the electrode site). The electrical stimuli will be applied at the minimum level and slowly increased, in order to minimize the risk of electrocution.

I may be asked some questions to ascertain some additional data, which may include: age, sex, height, weight, birth place, and whether I have any known neuromuscular disorders

I have been informed in advance that the study session for the data collections will be:

approximately fifteen minutes

up to one hour

I may be asked to return for additional sessions, and will be informed of this at the end of the study session. I am in no way obligated to participate in these additional sessions.

### **Potential Benefits**

There are no direct benefits or remuneration for my participation in this study.

### **Risks**

The application of surface electrodes may cause slight irritation of my skin under the electrode sites.

As electrical stimuli are applied to my skin, I understand there is a chance of electrocution. This risk has been minimized by using an electrical isolation unit, and by slowly increasing the electrical stimuli from the minimum level.

### **Confidentiality**

My identity will be kept strictly confidential unless otherwise discussed with the researcher. Any scientific report, presentation, or publication of the data will refer to me using a subject number. Information on my gender, age, and the presence of known neuromuscular disorders may be used.

I understand that the data from this research will be used in scientific reports, presentations, and publications and my identity will remain confidential. Data will be kept electronically and my consent forms and information will be kept as a hardcopy. Access to the data will be restricted to the researcher investigators. Data may be shared with research associates at other academic institutions. Data may be kept for an indefinite period of time.

### **Ethical review**

This study has been reviewed and received ethics clearance through the Carleton University Research Ethics Committee in accordance to the Tri-Council Policy Statement for Ethical Conduct for Research Involving Humans. Should I have any concerns or questions about my involvement in this study I may contact the committee chair (Professor Antonio Gualtieri, 613-520-2517, ethics@carleton.ca).

### **Withdrawal**

Participation in this study is strictly voluntary. I am free to withdraw from the experiment at any time and without any consequences. I will also declare if the researcher can/cannot use the data I have provided should I decide to withdraw from the study.

### **Consent for Participation in the Study**

**I hereby agree to participate in this study and consent to the use of this research data in scientific reports, presentations, and publications with the understanding that my identity will remain confidential. I have read and understand the above explanation of the research procedure and all my questions have been answered to my satisfaction. I**

**understand that I am free to withdraw from this research at any time and without any consequence.**

Participant: \_\_\_\_\_ Signature: \_\_\_\_\_ Date: \_\_\_\_\_

Experimenter: \_\_\_\_\_ Signature: \_\_\_\_\_ Date: \_\_\_\_\_

**Research undertaken as part of a graduate or undergraduate course requirement YES / NO**

If YES specify course name and course number

\_\_\_\_\_

Research undertaken as part of a graduate or undergraduate thesis research YES / NO

### **Consent for Photographs**

I understand that photographs (conventional/digital) may be required to document portions of the study. I have the option to consent or decline the usage of photographs during the study. Usage of these photographs will be restricted to scientific reports, presentations, or publications. I understand that my confidentiality will be maintained as best as possible; however, the usage of photographs may compromise my confidentiality.

**Photographs will be required in this study YES / NO**

If YES photographs will be CONVENTIONAL / DIGITAL

**I hereby consent to photograph to be taken in this study and consent to their use in scientific reports, presentations, and publications with the understanding that my identity may not remain confidential, as a consequence. I have read and understand the above explanation and all my questions have been answered to my satisfaction.**

Participant: \_\_\_\_\_ Signature: \_\_\_\_\_ Date: \_\_\_\_\_

Experimenter: \_\_\_\_\_ Signature: \_\_\_\_\_ Date: \_\_\_\_\_